INFORMATION TO USERS

This manuscript has been reproduced from the microfilm master. UMI films the text directly from the original or copy submitted. Thus, some thesis and dissertation copies are in typewriter face, while others may be from any type of computer printer.

The quality of this reproduction is dependent upon the quality of the copy submitted. Broken or indistinct print, colored or poor quality illustrations and photographs, print bleedthrough, substandard margins, and improper alignment can adversely affect reproduction.

In the unlikely event that the author did not send UMI a complete manuscript and there are missing pages, these will be noted. Also, if unauthorized copyright material had to be removed, a note will indicate the deletion.

Oversize materials (e.g., maps, drawings, charts) are reproduced by sectioning the original, beginning at the upper left-hand corner and continuing from left to right in equal sections with small overlaps.

Photographs included in the original manuscript have been reproduced xerographically in this copy. Higher quality 6" x 9" black and white photographic prints are available for any photographs or illustrations appearing in this copy for an additional charge. Contact UMI directly to order.

Bell & Howell Information and Learning
300 North Zeeb Road, Ann Arbor, MI 48106-1346 USA

UMI®
800-521-0600

HIGH-RESOLUTION ANALYTICAL ELECTRON MICROSCOPY AND CREEP DEFORMATION OF SILICON NITRIDE CERAMICS

By

QIANG JIN, B. Eng., M. Eng.

A Thesis

Submitted to the School of Graduate Studies

in Partial Fulfilment of the Requirements

for the Degree

Doctor of Philosophy

McMaster University

@ Copyright by Qiang Jin, May, 1998

CREEP OF SILICON NITRIDE

DOCTOR OF PHILOSOPHY (1998)
(Materials Science and Engineering)

McMaster University
Hamilton, Ontario

TITILE: High-Resolution Analytical Electron Microscopy and Creep Deformation of Silicon Nitride Ceramics

AUTHOR: Qiang Jin, B.Eng. & M. Eng.

SUPERVISOR: Professors D.S. Wilkinson and G.C. Weatherly

NUMBER OF PAGES: xv, 196

ABSTRACT

The typical microstructure of silicon nitride consists of rigid Si_3N_4 grains and intergranular amorphous films associated with the liquid phase sintering process involved during densification. The presence of the amorphous films may affect the creep behaviour of silicon nitride ceramics at elevated temperatures. The advent of high resolution transmission electron microscopy (HRTEM) coupled with fine-probe chemistry analysis enables us to investigate the structure and chemical composition of the nano-scale grain boundary amorphous films and the role they play in creep deformation of silicon nitride.

The materials investigated consist of β-Si_3N_4 grains with and without secondary crystalline phases. All grains were covered with a thin intergranular amorphous film at both homophase and heterophase boundaries. It was found that these amorphous films have a characteristic value of thickness, independent of grain misorientation, but dependent on the chemical composition of the film and the grains on either side of the film. The creep behaviour of the materials were evaluated by compressive and tensile testing. The grain-boundary film thickness distribution was measured before and after creep using both high-resolution lattice imaging technique and Fresnel fringe imaging technique. The results show a narrow range of film widths in the uncrept material but a bimodal distribution after creep. This provides, for the first time, direct evidence for the occurrence of viscous flow of intergranular amorphous films during creep deformation of silicon nitride. Finally, a model is developed to describe the viscous flow process in multi-phase

Si_3N_4 materials in contrast to prior models which are only applicable to “pure” Si_3N_4 materials. The creep response predicted by the model is consistent with the experiment.

ACKNOWLEDGEMENTS

I would like to express my gratitude to my supervisors Professor D.S. Wilkinson and Professor G.C. Weatherly for their constant guidance and help throughout this research. Thanks are also expressed to Professor A.P. Hitchcock for valuable guidance as part of my Ph.D. committee.

Thanks also go to Fred Pearson, Andy Duft, Chris Butcher, Ed McCaffery for their help with the experimental work. Mention should also be made to Dr. A. Perovic and Dr. X.G. Ning for their suggestions and expertise in TEM operation.

Dr. H.-J. Kleebe from Technische Universität Bayreuth, Germany, provided some of the experimental materials. Dr. W.E. Luecke of National Institute of Standards and Technology, USA, conducted the tensile creep tests.

I also wish to thank all the students of the mechanical properties group (Rm A206) for their friendship and help.

The financial support of the Natural Sciences and Engineering Research Council of Canada, and McMaster University is gratefully acknowledged.

Special thanks to my wife for her constant support and encouragement.

TABLE OF CONTENTS

ABSTRACT iii
ACKNOWLEDGEMENTS v
TABLE OF CONTENTS vi
LIST OF FIGURES AND TABLES ix

1. INTRODUCTION 1

2. LITERATURE REVIEW 5
   2.1 Introduction 5
   2.2 Fabrication and General Microstructure Silicon Nitride 5
   2.3 Stability and Chemistry of Amorphous Grain-Boundary Phase 8
   2.4 Creep of Silicon Nitride 15
      2.4.1 General Creep Behaviour 15
      2.4.2 Creep Models 21
      2.4.3 Explanation of Creep Behaviour 38
      2.4.4 Effect of Oxidation and Crystallization on Creep Behaviour 41

3. EXPERIMENTAL TECHNIQUES 45
   3.1 Introduction 45
   3.2 Materials 45
   3.3 High Temperature Creep Tests 50
      3.3.1 Tension Tests 50
      3.3.2 Compression Tests 52
   3.4 Transmission Electron Microscopy 54
   3.5 Grain-Boundary Film Thickness Measurements 54
      3.5.1 LFI Technique 55

3.5.2 FFI Technique 56

3.5.3 Statistical Analysis 56

3.6 Chemistry Analysis 57

4. DETERMINATION OF GRAIN-BOUNDARY FILM THICKNESS BY THE FRESNEL FRINGE IMAGING TECHNIQUE 60

4.1 Introduction 60

4.2 Results and Discussion 61

4.2.1 Determination of Grain-Boundary Film Thickness 61

4.2.2 Accuracy and Validity of Measurement 66

4.2.3 Advantage of FFI and Limitations of LFI 70

4.3 Summary 73

5. MICROSTRUCTURE OF SILICON NITRIDE 74

5.1 Introduction 74

5.2 Results 77

5.2.1 General Microstructure 77

5.2.2 Structure of Grain-Boundary Films 86

5.2.3 Chemical Composition of Grain-Boundary Films 94

5.3 Discussion 102

5.3.1 Chemistry Dependence of Intergranular Film Thickness 102

5.3.2 Crystallization of Intergranular Phase in Y_2O_3 Doped Material 106

5.4 Summary 112

6. VISCOUS FLOW CREEP OF SILICON NITRIDE PART I, EXPERIMENTAL OBSERVATIONS 114

6.1 Introduction 114

6.2 Results 117

6.2.1 Creep Response 117

6.2.2 Film Thickness Distribution After Creep 121
6.2.3 Other Microstructural Features Caused by Creep 134
6.3 Discussion 137
6.4 Summary 143

7. VISCOUS FLOW CREEP OF SILICON NITRIDE PART II, MODELING AND DISCUSSION 144
7.1 Introduction 144
7.2 Viscous Flow Model for Multiphase Ceramics 146
7.2.1 General Considerations 146
7.2.2 Strain Rate and Local Stress Calculation 149
7.2.3 Ceramics Containing an Arbitrary Volume Fraction of SP Grains 153
7.2.4 Effect of Microstructure 155
7.3 Discussion 162
7.4 Summary 169

8. SUMMARY AND CONCLUSIONS 171

APPENDICES 175
Appendix A. A Model for Cavity Growth by Viscous Flow and Its Effect on Grain-Boundary Film Thickness 175
Appendix B. Separation Rate of Parallel Plates Separated by a Newtonian Fluid Layer with Unequal Pressures at Ends 184
BIBLIOGRAPHY 186

LIST OF FIGURES AND TABLES

Figure 2.1 Typical microstructure of Si_3N_4 ceramic showing equiaxed and elongated grains (Gasdaska 1994)........ 7

Figure 2.2 Plot of measured film thickness as a function of the Ca content in the silicon nitride materials (Tanaka et al 1994b)........ 11

Figure 2.3 The thickness of the intergranular films in polycrystalline Si_3N_4 and Si_3N_4 particles in the glass as a function of the ionic radius of the lanthanide ion (Wang et al 1996)........ 11

Figure 2.4 Excess free energy as a function of grain boundary thickness due to van der Waals, structural (or steric) and applied forces (Chadwick 1990)........ 14

Figure 2.5 Typical creep curve for a monolithic material (Kingery et al 1976)........ 16

Figure 2.6 The creep response of SN220 at 1200°C and 63.5 MPa under four-point bending. Before creep the material was annealed at 1200°C from 0 to 400h (Chadwick 1990)........ 18

Figure 2.7 The creep response of GN 10, tested in tension at 1275°C and 137.5 MPa, showing a gradually decreasing strain rate (Luecke and Wiederhorn 1993)........ 18

Figure 2.8 The creep response of a HIPed Y_2O_3-doped Si_3N_4, NT154, tested in tension at 1400°C and 125 MPa, two plateaus of strain rate occurring in the creep process (Luecke and Wiederhorn 1993)........ 19

Figure 2.9 The creep response of SN220 tested in four point bending at 1325°C. Two plateaus occur during creep, which is different from Figure 2.6 (Chadwick 1990)........ 19

Figure 2.10 Creep of NT154 at 1430°C, showing creep asymmetry. Under the same applied stress, the creep rate in tension is from 10 to 100 times that in compression (Wiederhorn et al 1994)........ 20

Figure 2.11 Model for viscous flow creep based on the assumption of cubic grains (Pharr and Ashby 1983)........ 23

Figure 2.12 Two-dimensional model for incompressible fluid between rigid hexagons (Drucker 1964)........ 23

Figure 2.13 Strain dependence term of the creep rate $S(\varepsilon_N)$ as a function of normalized strain $\varepsilon_N=\varepsilon/f$ predicted theoretically from equation 2.8 (Jin 1995).......... 26

Figure 2.14 Plot of critical nucleation stresses for spherical and oblate cavities for hot-pressed silicon nitride (Thouless et al 1984).. 35

Figure 2.15 Schematic diagram illustrating the microcrack formation process. (a) uncavitated interface, (b) nucleation of oblate cavities along two-grain boundary,(c) coalescence to a full-facet microcrack, (d) an uncavitated triple pocket, (e) nucleation of a spherical cavity in the glass, (f) depletion of the pocket by viscous flow,(g) expansion to full-facet microcrack by viscous flow,(h) growth to full-facet size by solution-reprecipitation at low stress (Marion et al 1983)....................... 36

Figure 3.1 SEM microstructure of the experimental materials, (a) undoped, (b) 800 ppm Ba doped, and (c) 4 wt.% Y_2O_3 doped, showing the equiaxed and elongated Si_3N_4 grains. The bright grains in (c) represent secondary crystalline phases which contain yttrium... 49

Figure 3.2 The tensile creep specimen used in this study (Luecke et al 1995)......... 51

Figure 3.3 Schematic diagram for the laser extensometer used for measuring tensile creep deformation (Carroll et al 1989).. 51

Figure 3.4 Schematic diagram of the loading system used for measuring the compressive creep deformation.. 53

Figure 3.5 Principle of the LFI technique for measuring the grain-boundary amorphous film thickness.. 55

Figure 4.1 Schematic diagram representing the boundary potential model (a), and the corresponding schematic profile of intensity for underfocus (b). I_b is the background intensity; I_c is the intensity at the center of the boundary film; I_f is the intensity of the first set of fringes.. 63

Figure 4.2 Through focal series of images of a grain boundary in silicon nitride; (a) underfocus of 1400 nm, (b) underfocus of 700 nm, (c) overfocus of 700 nm, and (d) overfocus of 1400 nm. The fringe spacing decreases with decreasing defocus......... 64

Figure 4.3 Measured fringe spacing data as a function of defocus for the boundary shown in Figure 4.2, (a) the fitting function $W = W_0 + c\Delta f^{1/2}$ is used to obtain the boundary film thickness; (b) linear fitting is used, confirming that the fringe spacing (W) is a function of $\Delta f^{1/2}$ 65

Figure 4.4 High-resolution lattice fringe image of the grain boundary shown in Figure 4.2 67

Figure 4.5 Histogram of the distribution of parameter c in the fitting function $W = W_0 + c\Delta f^{1/2}$ obtained from different grain boundaries 68

Figure 5.1 TEM micrographs of the undoped (a) and Ba doped material (b), showing equiaxed and elongated β-Si_3N_4 grains 78

Figure 5.2 TEM micrograph of an amorphous intergranular phase in a triple junction and at two-grain boundaries 79

Figure 5.3 (a) TEM micrograph of the Y_2O_3 doped material after heat treatment at 1430°C for 690h, showing secondary crystalline phases formed at multigrain junctions (indicated by arrows); (b) a EDX spectrum corresponding to $Y_5(SiO_4)_3N$ (indicated by a 1 in a); (c) a EDX spectrum corresponding to $Y_2Si_2O_7$ (indicated by a 2 in a) 81

Figure 5.4 Micrographs of a multigrain junction in the Y_2O_3 doped heat-treated sample showing complete crystallinity in (a) bright-field and (b) dark-field 82

Figure 5.5 Results of XRD analysis of the Y_2O_3 doped material, showing the presence of β-Si_3N_4, α- and δ-$Y_2Si_2O_7$, and N-apatite phase in the microstructure... 83

Figure 5.6 SEM microstructure of the Y_2O_3 doped sample (polished without etching) showing the distribution of the secondary crystalline phases (bright particles) 85

Figure 5.7 Annular dark-field image showing secondary crystalline phases enveloping the Si_3N_4 grains. The bright contrast of the secondary crystalline phases is due to the presence of Y. The bright film between two Si_3N_4 grains (indicated by an arrow) suggests that the film contains Y 85

Figure 5.8 Histogram of the grain-boundary film thickness distribution in the as-sintered undoped material. The mean thickness value and the standard deviation are shown 87

Figure 5.9 Histogram of the grain-boundary film thickness distribution in the as-sintered Ba doped material. The mean thickness value and the standard deviation are shown 88

Figure 5.10 High-resolution lattice image of a Si_3N_4 grain boundary in the as-sintered undoped material, showing an amorphous intergranular film thickness of 1.0 nm. The lattice fringes in the lower grain are parallel to the $\{10\bar{1}0\}$ plane whose planar spacing is 0.66 nm........ 89

Figure 5.11 High-resolution lattice image of a Si_3N_4 grain boundary in the as-sintered Ba doped material, showing an amorphous intergranular film thicknes of 1.2 nm. The lattice fringes in the lower grain are parallel to the $\{10\bar{1}0\}$ plane whose planar spacing is 0.66 nm........ 90

Figure 5.12 Histogram of the two-Si_3N_4-grain-boundary film thickness distribution in the Y_2O_3 doped material after complete crystallization. The mean thickness value and standard deviation are shown........ 92

Figure 5.13 High-resolution lattice image of a homophase boundary in the grip end of the Y_2O_3 doped material after complete crystallization (1430°C, 690h), showing the film thickness of 0.74 nm........ 93

Figure 5.14 High-resolution lattice images of amorphous films at heterophase boundaries, (a) between Si_3N_4 and $Y_5(SiO_4)_3N$ showing a film thickness of 3.5 nm.; (b) between Si_3N_4 and $Y_2Si_2O_7$ showing a film thickness of 4.5 nm........ 95

Figure 5.15 EDS spectra from the grain boundary film (dash line) and 20 nm into the Si_3N_4 grain (solid line), indicating the presence of O in the grain boundary film... 96

Figure 5.16 X-ray energy filtered images showing the excess of O, less Si and N at a grain boundary: (a) bright-field image: (b) Si-Kα X-ray mapping; (c) O-Kα X-ray mapping; (d) N-Kα X-ray mapping. 97

Figure 5.17 EDS spectra from the Si_3N_4 grain boundary (dash line) and 20 nm into the Si_3N_4 grain (solid line), indicating the presence of Y and O in the thin intergranular film........ 99

Figure 5.18 X-ray energy filtered images showing an Y-rich glassy phase at a Si_3N_4 grain boundary: (a) bright-field image; (b) Y-Kα X-ray mapping; (c) brightness across the grain boundary; (d) line scanning of Y-Kα across the grain boundary...... 100

Figure 5.19 Yttrium concentration profile across and along a grain boundary film. This profile was obtained from measurements in a step of 1 nm........ 101

Figure 5.20 Phase relations in the system Si_3N_4-SiO_2-Y_2O_3-YN (Gaukler et al 1980)........ 108

Figure 5.21 High-resolution lattice image of a triple junction formed by two Si_3N_4 grains and one secondary phase grain, showing the small size of triple junctions left after multigrain junction crystallization........ 111

Figure 6.1 Creep response for the undoped material at 1400°C under different compressive stresses (Jin 1995): (a) strain-time curves, (b) strain rate vs strain curves........ 118

Figure 6.2 Creep response for the Ba doped material at 1400°C, 100MPa for different time periods (7h, 40h, 200h): (a) strain-time curves, (b) strain rate vs strain curves. The solid curve is for creep of 40h while the dash curve is for creep of 200h........ 119

Figure 6.3 Creep response of the Y_2O_3 doped material crept at 1430°C under stresses of 40 MPa and 150MPa, showing initial constant strain rate followed by a measurable decrease in strain rate at a strain of 3×10^{-3} (Luecke 1997)........ 120

Figure 6.4 Histogram of the grain-boundary film thickness distribution in the undoped material after creep at 1400°C for 20h under a stress of 200MPa (total strain 1.1%). Two peaks at 0.6 nm and 1.53 nm indicate a bimodal distribution of the grain-boundary film widths after creep........ 122

Figure 6.5 High-resolution latice images of grain-boundary amorphous films in the experimental material crept at 1400°C under 200MPa for 20h, showing a large difference in film thickness: (a) a thinner grain boundary with a film thickness of 0.6 nm; (b) a thicker grain boundary with a film thickness of 1.56 nm. In both micrographs, the $\{10\bar{1}0\}$ planar spacing of 0.66 nm were used for accurate determination of the grain-boundary film thickness........ 124

Figure 6.6 Film thickness distribution in the Ba doped material after creep for different time; (a) 7h (ε=0.0049) , (b) 40h (ε=0.0104), (3) 200h (ε=0.0307)........ 128

Figure 6.7 High-resolution lattice fringe images of grain boundary films in the Ba doped material crept under 100MPa for 40h, showing (a) a film thickness of 0.8 nm at one grain boundary, and (b) a film thickness of 1.7 nm at another grain boundary........ 130

Figure 6.8 Histogram of film thickness distribution of homophase boundaries of the Y_2O_3 doped material crept at 1430°C under 40MPa for 690h, showing a bimodal distribution with the first peak at 0.52 nm and a second peak at 1.33 nm........ 131

Figure 6.9 High-resolution lattice images of homophase boundary films in the gauge section of the Y_2O_3 doped Si_3N_4 sample crept under 40MPa for 690h, showing (a) a film thickness of 0.5 nm at one grain boundary, and (b) a film thickness of 1.2 nm at another grain boundary 133

Figure 6.10 Cavitation at multigrain junctions in the Ba doped material after creep at 1400°C, 100MPa for 200h; (a) single spherical cavity, (b) multiple lens-shaped cavities separated by ligaments 136

Figure 6.11 Strain whorls observed at two-grain boundaries in the Ba doped material after creep at 1400°C, 100MPa for 200h 137

Figure 6.12 Schematic diagram of the grain-boundary film thickness distribution in a glass-containing ceramic; (1) uniform film thickness in the as-sintered state, (b) bimodal distribution of the film widths under a compressive load 139

Figure 6.13 (a) High-resolution lattice image of a thick grain boundary film in the Ba doped material crept at 1400°C, 100MPa for 200h, (b) lower magnification of the grain boundary, showing it is connected to a triple junction cavity 142

Figure 7.1 (a) Simplified microstructure of Si_3N_4 containing 1/3 of SP grains, (b) The pressures in the multigrain junctions and the average normal stresses acting on the different boundaries 148

Figure 7.2 Non-dimensional strain rate term $S'(\zeta)$ as a function of the normalized strain ζ for different values of m with a constant value of $\Phi=0.15$: (a) tensile creep; (b) compressive creep 156

Figure 7.3 Nondimensional strain rate term $S'(\zeta)$ as a function of the normalized strain ζ for different values of Φ with a constant value of m=5, (a) tensile creep; (b) compressive creep 157

Figure 7.4 Stresses in the local regions vary with the volume fraction of SP grains for a compatible deformation (m=5) 159

Figure 7.5 Average normal stresses on perpendicular boundaries and pressures at their ends as a function of the normalized strain for different values of m with $\Phi=1/3$, (a) homophase boundaries; (b) heterophase boundaries 160

Figure 7.6 Average normal stresses on angle homophase and heterophase boundaries as a function of the normalized strain for different values of m with $\Phi=1/3$. 161

Figure 7.7 Creep resistance as a function of strain found experimentally (solid curve); and predicted theoretically (dashed curve) for compression testing at 1400°C and 200MPa. Two values of the initial film thickness (1 nm and 1.5 nm) and a stress exponent n=1.7 are used in modeling.......... 167

Figure A1 Microstructure of glass-containing ceramic which is simplified as hexagons of rigid grains (facet length 2L) surrounded by amorphous grain-boundary films (thickness $2\delta_0$) and cylinders of glass pockets (radius R<<L) at three-grain channels.......... 176

Figure A2 Schematic diagram for stress analysis during viscous flow process.......... 176

Figure A3 Effect of viscosity (or temperature) on the cavity growth rate indicating that the higher viscosity the lower growth rate (σ^{∞}=100MPa).......... 181

Figure A4 Effect of stresses on the cavity growth rate with an assumed viscosity $\eta=10^7$ Pa.s.......... 182

Figure A5 Effect of cavity growth on the film thickness change, showing the boundary in tension takes almost all the glass which flows out from the pockets while boundaries in compression essentially do not change their thickness (σ=100MPa, $\eta=10^5$ Pa.s).......... 183

Figure B1 Schematic diagram of the stress distribution for viscous flow of a fluid layer in a two-grain boundary channel.......... 185

Table A1. Values of Assumed Parameters.......... 180

Chapter 1

INTRODUCTION

Silicon nitride ceramics have received considerable attention in recent years for high temperature structural applications due to their many useful intrinsic properties. For example, they have low density, high strength at high temperatures, good thermal stress resistance and relatively good resistance to creep and oxidation which make them superior to other structural ceramics and commercial high temperature metallic alloys. Obviously, to ensure the long term reliability of structural components in use at elevated temperature, the creep behaviour of the materials from which they are made must be understood.

Due to insufficient volume diffusion and volatilization, silicon nitride does not sinter easily in the "pure state". So most silicon nitride ceramics are sintered or hot-pressed with the addition of 5 to 20 wt% of oxides (Loehman 1994) that become molten at the processing temperature. Densification is enhanced through solution of α-Si_3N_4 in the liquid and its precipitation as grains of β-Si_3N_4. When the ceramic is cooled, the liquid usually forms an amorphous grain boundary phase. The resulting microstructure consists of Si_3N_4 grains, a grain boundary amorphous phase and sometimes secondary crystalline phases. The creep behaviour of the material is thus limited or decreased when the intergranular amorphous phase softens at high temperatures.

In general, three creep mechanisms associated with this amorphous grain-boundary phase have been proposed to explain the creep behaviour of Si_3N_4 ceramics. These are viscous

flow, dissolution-reprecipitation and cavitation mechanisms. The creep mechanisms have been found to be not only dependent on the material, or the composition of the intergranular amorphous phase (Lange et al 1980a), but also dependent on the testing temperature and the stress state (Wilkinson 1998). Models have been developed to describe the creep process in terms of the stress and temperature dependence of the creep response based on simple idealized microstructures. However, since much of the analysis in the literature is based on indirect evidence and/or simplified models, more direct evidence from the microstructural evolution is required in order to better understand the creep process of silicon nitride. For example, viscous flow controlled creep is generally assumed to be a transient process since the initial intergranular amorphous phase is very thin, with a thickness in the scale of nanometers. Although several models which capture this essential feature have been developed to describe viscous flow, direct evidence of microstructural evolution due to this process has never been reported. Moreover, the existing viscous flow models are based on the assumption of constant initial thickness value of grain boundary amorphous films. It is questionable to apply these models to silicon nitride materials containing secondary crystalline phases which may result in non-uniform initial grain boundary film thickness (Kleebe et al 1992). Experimental evidence for a cavitation mechanism is the presence of cavities in the multigrain junctions and at two-grain boundaries. Although this has been repeatedly reported in the literature, our current understanding of the processes which control the nucleation and growth of cavities is poor (Wilkinson 1994). Additionally, more work is required to understand the structure and chemistry of grain boundary amorphous films although some work has been done in this aspect. The objectives of this work were to study the structure and chemistry of grain

boundary films and to investigate viscous flow of the amorphous grain-boundary phase during creep deformation of silicon nitride from both an experimental and theoretical viewpoint. In the present study, the materials used are a high purity silicon nitride, a 800 wt. ppm Ba doped silicon nitride and a 4 wt.% Y_2O_3-doped commercial silicon nitride. The creep behaviour was evaluated using both compression and tension tests. Microstructural observations were conducted by means of transmission electron microscopy.

The thesis is organized as follows:

Chapter 2, Literature Review, contains a background of the present work, which includes the microstructure of silicon nitride and our current understanding of creep mechanisms in silicon nitride ceramics.

Chapter 3, Experimental Methods, describes the experimental techniques and related background theories used in microstructural and mechanical characterization of the samples.

Chapter 4, Determination of Grain-Boundary Film Thickness by the Fresnel Fringe Imaging Technique, discusses the validity and accuracy of the Fresnel fringe imaging technique in quantitative determination of grain-boundary amorphous film thickness.

Chapter 5, Microstructure of Silicon Nitride, investigates the microstructure of silicon nitride with and without the sintering additives, with emphasis on the thickness and chemistry of the grain boundary films.

Chapter 6, Viscous Flow Creep of Silicon Nitride (Part I), presents the experimental observations of creep response and film thickness distributions after creep.

Chapter 7, Viscous Flow Creep of Silicon Nitride (Part II), describes a model for creep by viscous flow in multiphase silicon nitride ceramics, and compares it with the experimental observations.

Chapter 8, Summary and Conclusions, contains the overall conclusions derived from this study.

Chapter 2

LITERATURE REVIEW

2.1 Introduction

In this chapter, some background to the relevant work in the field of creep of silicon nitride is presented. This begins with a brief introduction of the fabrication and the resulting microstructure of silicon nitride ceramics (section 2.2). An important microstructural feature in silicon nitride materials is the presence of an amorphous phase at grain boundaries, which is believed to have a dramatic effect on the high temperature properties. Thus, the stability and chemistry of this amorphous phase is discussed (section 2.3). In section 2.4, our current understanding of creep in silicon nitride ceramics is reviewed and assessed. This includes the general creep behaviour of silicon nitride, the models which have been developed for creep in ceramics containing an intergranular amorphous phase, followed by current explanations of creep behaviour of silicon nitride. At the end of this section, the effect of oxidation and crystallization of the intergranular amorphous phase on creep behaviour of silicon nitride is also reviewed.

2.2 Fabrication and General Microstructure of Si_3N_4

Silicon nitride can be considered to be a composite material consisting of elongated β-Si_3N_4 grains embedded in a matrix of glass and finer equiaxed β-Si_3N_4 grains (Wiederhorn et al 1994). This microstructure is developed by a liquid phase sintering process. Silicon nitride has two hexagonal modifications, α and β. The basic structure consists of silicon atoms located in the centre of nitrogen tetrahedra, each nitrogen atom belonging to three

tetrahedra. The strong covalent bonds between silicon and nitrogen atoms make the volume diffusivity of Si_3N_4 very low. Densification for "pure" silicon nitride powder is therefore very difficult to achieve using classical solid state sintering techniques. Since α-Si_3N_4 is a higher free energy, metastable form, transformation from α to β-Si_3N_4 can occur at high temperatures through a solution-precipitation process aided by a liquid phase. Dense silicon nitride ceramics, therefore, are invariably sintered using additives which form silicate-related eutectic liquids based on SiO_2, which is always present in the starting powder as a surface layer on each silicon nitride particle. It is now recognized that some metal oxides (e.g. MgO, Y_2O_3) and nitrides (e.g. AlN) are effective sintering aids. There is often a compromise between sinterability, which favours low valence ions, and the increased 'softening' temperature of glass residues within high temperature ceramics, which favours high-valence cations such as Y (Lewis et al 1988). Good time-dependent properties at high temperatures require high viscosity of the grain-boundary residues of the liquid sintering medium. For instance, changing the sintering aid from MgO to Y_2O_3 can increase the creep resistance, and hence the lifetime, by five orders of magnitude (Wiederhorn et al 1994).

It is now recognized that these sintering liquids usually have M-Si-O-N compositions in silicon nitride. The metallic ion M (or ions) mainly comes from oxides added as the sintering aids. At high temperatures, this eutectic silica-rich liquid enhances rearrangement of the Si_3N_4 grains. The α-Si_3N_4 particles, which are a major component of the starting sintering powders, dissolve in the liquid. Upon supersaturation, β-Si_3N_4 is precipitated and either forms small particles in the triple junctions or is epitaxially

Figure 2.1 Typical microstructure of Si_3N_4 ceramic showing equiaxed and elongated grains (Gasdaska 1994).

deposited on pre-existing β-Si_3N_4 particles (Kleebe et al 1994). The resulting microstructure consists of both elongated and finer equiaxed β-Si_3N_4 grains (Figure 2.1) which influence fracture toughness as well as time-dependent deformation and fracture mechanisms. Fracture toughness is required at all application temperatures and increments in toughness can be obtained from primary crack deflection (Faber et al 1983), interface microcracking (Faber et al 1984) and crack bridging/pull-out. These toughening mechanisms require a relatively weak interface and crystal anisotropy which are the microstructural features of Si_3N_4 ceramics. The morphological anisotropy stems from liquid phase sintering due to anisotropy in solid-liquid interface energy and growth kinetics. The elongated grains, with a typical aspect ratio of 5-10 (Lewis et al 1988) in silicon nitride, can improve the fracture toughness significantly (Lange 1973). It is

reported (Becher et al 1994) that this can lead to fracture toughness up to 10-12 MPa$\sqrt{m}$ as compared to ≤4 MPa$\sqrt{m}$ in a fine, more equiaxed grain structure.

2.3 Stability and Chemistry of Amorphous Grain-Boundary Phase

An important microstructural feature in silicon nitride is the presence of a continuous intergranular amorphous phase, which is formed from the sintering liquid upon cooling. This amorphous phase to a large extent controls the high temperature properties of the ceramic. At temperatures exceeding the softening point of the amorphous phase (about 1000°C), diffusion-related behaviour of the material such as creep and oxidation resistance degrades rapidly (Marion et al 1987, Ziegler et al 1987, Cinibulk et al 1992). Therefore optimization of structural ceramics requires the minimization of the grain boundary phase and a high viscosity of the sintering liquids. The amount and properties of the glass phase depend on the additives. In general, the amorphous phase is located at multigrain junctions and along two-grain boundaries. The amorphous phase at multigrain junctions can be crystallized by heat treatment (Bonnell 1987). However, complete crystallization appears to be impossible as residual glass always remains along two-grain boundaries (Kessler et al 1992). The structural and compositional characteristics of the grain boundary films are thought to be closely related to the reported degradation of the high temperature properties (Pierce et al 1986). For example, Tanaka et al (1994) studied the high-temperature strength of fluorine-doped silicon nitride and found that subcritical crack-growth resistance and creep resistance at 1400°C were degraded significantly by the presence of F as compared with a high-purity Si_3N_4.

High-resolution transmission electron microscopy (HRTEM) in combination with analytical electron microscopy (AEM) has provided important information on the grain boundary film characteristics. Kleebe and coworkers (1993a, 1993b, 1994a, 1994b) have investigated a number of silicon nitride materials, fluxed with various additives, and found that the film thickness at two-grain boundaries is constant within ±0.1 nm for a specific material, independent of grain misorientations. Only small angle grain boundaries and special low energy grain boundaries are not wetted with a glass film (Kleebe et al 1994b). Detailed experimental investigations revealed that silicate-based intergranular films have a thickness between 0.5 and 2 nm, depending on the composition of the film. These values of thickness correspond to the stacking of a few SiO_4^{4-} tetrahedra which form the basis of amorphous SiO_2.

Although great advances have been made by direct observation of grain boundary films, little is known of the atomic structure of these films. Clarke (1985) proposed a model of the interfacial structure, in which a partially ordered intermediate layer of SiO_4^{4-} tetrahedra exists between the Si_3N_4 grains and the amorphous film or triple pockets. Thereafter, Thorel et al (1986, 1989) observed "a specific atomic feature" at the interface between Si_3N_4 surface and bulk SiO_2 glass. It was thus suggested that epitaxial ordering exists in the glass adjacent to the interface. On this basis, it is expected that a similar ordering should be observable at the grain boundary film. Kleebe (1994c) observed a similar specific feature on the HRTEM images taken at the interface formed by the Si_3N_4 grain and the glass pocket, but expressed reservations regarding the interpretations of such features. Considering the effect of the specimen thickness and defocus value of the

objective lens on contrast and periodicity of the HRTEM images, Pan (1996) concluded that the interfacial structure is probably direct Si_3N_4/glass bonding, rather than an ordered transition phase between the Si_3N_4 and the glass phase. The specific features observed near the interface are due to an imaging artefact.

The film chemistry to a large extent determines the equilibrium film thickness. It is suggested (Kleebe et al 1994b) that the overall volume fraction of the amorphous phase has no major effect on film thickness. Excess glass resides in the triple junctions between grains. The effect of impurity cations on the grain boundary film thickness has been investigated in several systems. Kleebe et al (1994a) studied Yb_2O_3/Al_2O_3-fluxed Si_3N_4 materials with and without the addition of small amounts of CaO and found that the film thickness increases from 1.0 nm to 1.3 nm with CaO addition. Tanaka et al (1994a) investigated a series of high purity silicon nitride ceramics doped with 0-450 ppm CaO and found that with increasing Ca content the thickness initially decreased but then increased with further additions of Ca, as shown in Figure 2.2. Ca was selected owing to the extremely limited solubility between CaO and Si_3N_4. The Ca was expected to segregate to the grain boundary phase, therefore affecting both interface chemistry and the equilibrium film thickness. The addition of 800 ppm Ba in a high-purity Si_3N_4 has been found to increase the film thickness from 1 nm to 1.4 nm (Jin 1995). Additionally, the thickness of the intergranular films in Si_3N_4 densified with lanthanide oxides has been systematically investigated by Wang et al (1996) using HRTEM. They found that the film widths increase with increasing ionic radius of the lanthanide, varying in the range from 1.0 nm to 1.7 nm, as shown in Figure 2.3.

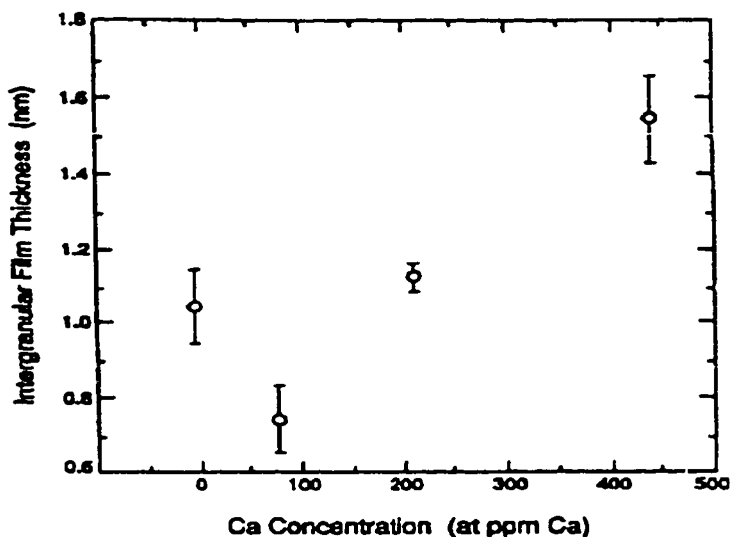

Figure 2.2 Plot of measured film thickness as a function of the Ca content in the silicon nitride materials (Tanaka et al 1994b).

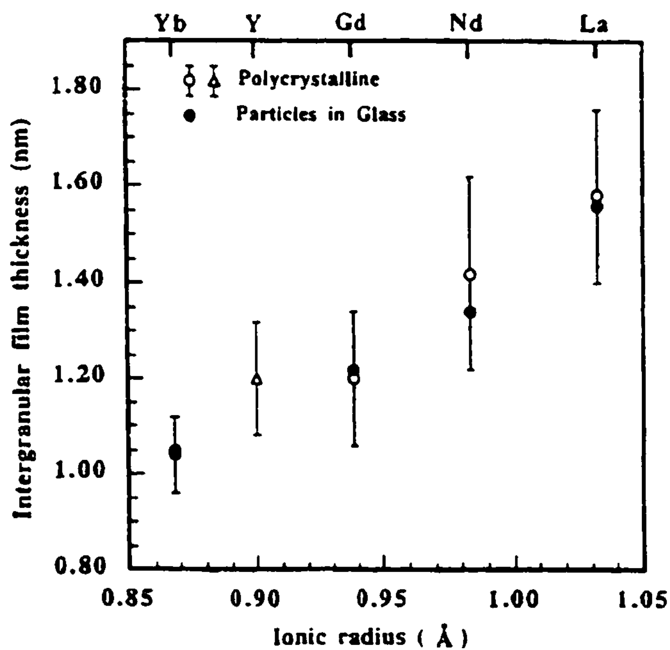

Figure 2.3 The thickness of the intergranular films in polycrystalline Si_3N_4 and Si_3N_4 particles in the glass as a function of the ionic radius of the lanthanide ion (Wang et al 1996).

The constant thickness of grain boundary films and its dependence on the film chemistry have been explained theoretically. Clarke and coworkers (1987, 1993) proposed a theory for the equilibrium thickness of grain boundary films, based on the balance of attractive and repulsive forces acting normal to an intergranular glass film. The attractive term mainly includes a van der Waals dispersion force, Π_{disp}, which acts to draw the grains together. The repulsive term may come from the contribution of the electrical double layer, Π_{edl}, and the structural force due to distortions of SiO_4^{4-} tetrahedra in the amorphous layer, Π_{st}. In the absence of any applied and capillary stresses, these forces balance at equilibrium and thus satisfy an equation of the form

$$\Pi_{disp} + \Pi_{st} + \Pi_{edl} = 0 \tag{2.1}$$

where

$$\Pi_{disp} = \frac{H_{\alpha\beta\alpha}}{6\pi h^3} \tag{2.2}$$

$$\Pi_{st} = -\frac{a\eta_0^2}{\sinh^2(h/2\xi)} \tag{2.3}$$

$$\Pi_{edl} = \frac{64(k_B T)^2 \varepsilon\varepsilon_0}{(zeh)^2} \tanh^2\left[\frac{ze\Psi_s}{4k_B T}\right] k^2 h^2 e^{-kh} \tag{2.4}$$

Here $H_{\alpha\beta\alpha}$ is the Hamaker constant; the subscripts α and β represent the Si_3N_4 and the intergranular amorphous phase respectively; h is the film thickness; $a\eta_0^2$ is a factor derived from the free energy difference between intergranular liquid with and without ordering; ξ is the structural correlation length which can be equated with the size of the molecular

unit of a SiO_4^{4-} tetrahedron; ψ_s is the surface potential of the grains; 1/k is the Debye screening length; k_BT is the Boltzmann constant times the absolute temperature; e is the electron charge; z is the ion charge; ε is the dielectric constant and ε_0 is the permittivity of a vacuum. Generally, in the absence of any sintering aids (except SiO_2), it is assumed that there is no electrical double layer at the grain boundaries (i.e., Π_{edl}=0) and the amorphous phase is a pure silica network. The addition of sintering aids (e.g., Ca^{2+}) may provide charged species in the amorphous film, which results in the formation of an electrical double layer (equation 2.4). On the other hand, different compositions of the amorphous phase reflect different physical and chemical properties, which in turn, may change the magnitude of the two competing forces, therefore, changing the equilibrium film thickness. The equilibrium film thickness has also been treated by Clarke (1994) using Cahn and Hilliard's (1958) diffuse interface approach.

The theories proposed by Clarke and his coworkers (1987, 1993, 1994) can be used to explain the thermodynamic stability of grain boundary films. It has been suggested (Wilkinson 1998) that the pressure applied during sintering plays a very important role in achieving an equilibrium grain boundary thickness. Chadwick (1990) calculated the driving force for equilibration from Clarke's model (1987). She found the difference in excess free energy (i.e., the driving force) between a grain boundary with a thick amorphous layer and one at equilibrium is very small (about 0.1 mJ/m^2, see Figure 2.4). The pressure applied during sintering provides an additional driving force, which has little effect on the equilibrium thickness but substantially increases the driving force.

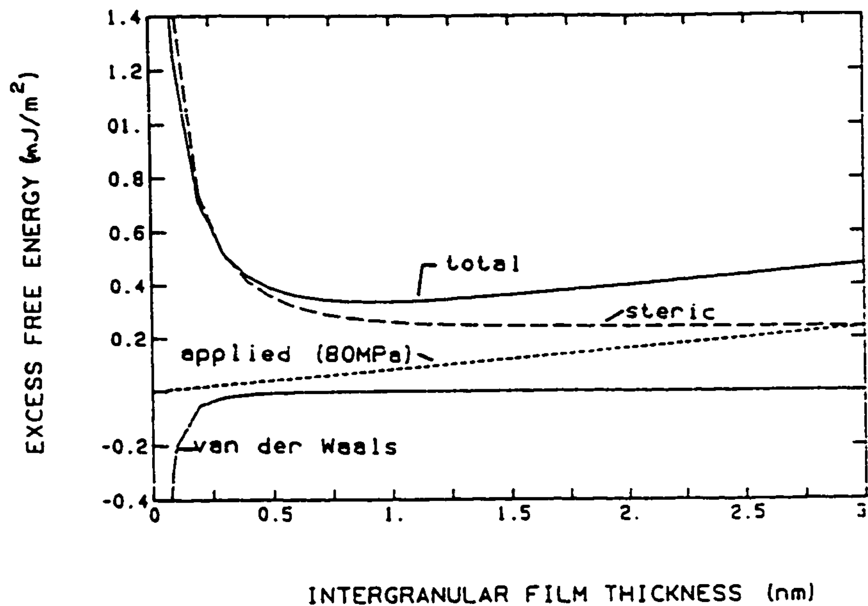

Figure 2.4 Excess free energy as a function of grain boundary thickness due to van der Waals, structural (or steric) and applied forces (Chadwick 1990).

Information regarding the composition of the amorphous phase could be obtained by analytical electron microscopy. As mentioned above, the amorphous phase in silicon nitride materials is assumed to be composed of silicon, oxygen, nitrogen and cations of additives. Since the intergranular films are so narrow (0.5-2 nm), the silica content and exact chemistry of such films could not be determined because of interference from the Si_3N_4 grains on either side of the film, even experimental confirmation of the existence of the cations of additives in the thin amorphous films has been difficult. Vetrano and coworkers (1993) investigated two silicon nitride materials fluxed respectively with 5 vol% and 10 vol% Yb_2O_3 and found excess oxygen and ytterbium in the amorphous films along grain boundaries. It was also reported that cerium and calcium could be

detected qualitatively in the intergranular films of a ceria-fluxed and CaO-fluxed sintered Si_3N_4 material, respectively (Kleebe et al 1993, 1994a). Based on these experimental results, it is suspected that additive cations are also present in the thin amorphous films in other silicon nitride materials.

The elemental distribution within the amorphous phase has been the topic of extensive composition analysis. Tanaka et al (1994b) concluded that the amorphous grain boundary film in a Si_3N_4 material is an oxynitride, compositionally graded from nitrogen-rich at the glass-crystal interface to oxygen-rich in the center of the film. The distribution of impurity cations has also been investigated. Kleebe et al (1994a) studied a Ca-doped Si_3N_4 and found that the concentration of Ca is almost constant in the triple junctions and at grain boundaries. However, the composition distribution of impurity cations, such as Ca, across the film thickness has yet to be determined (Tanaka et al 1994b).

2.4 Creep of Silicon Nitride

2.4.1 General Creep Behaviour

In general, three distinct stages are exhibited during creep deformation of monolithic materials. After an intantaneous elastic deformation on the application of a load, the creep rate decreases with time during the primary stage, and then remains constant in the stage of steady-state creep. A final (tertiary) stage of creep leads to failure (Figure 2.5). The steady-state regime is usually used to analyze and compare the creep behaviour of materials with the Norton power law relation:

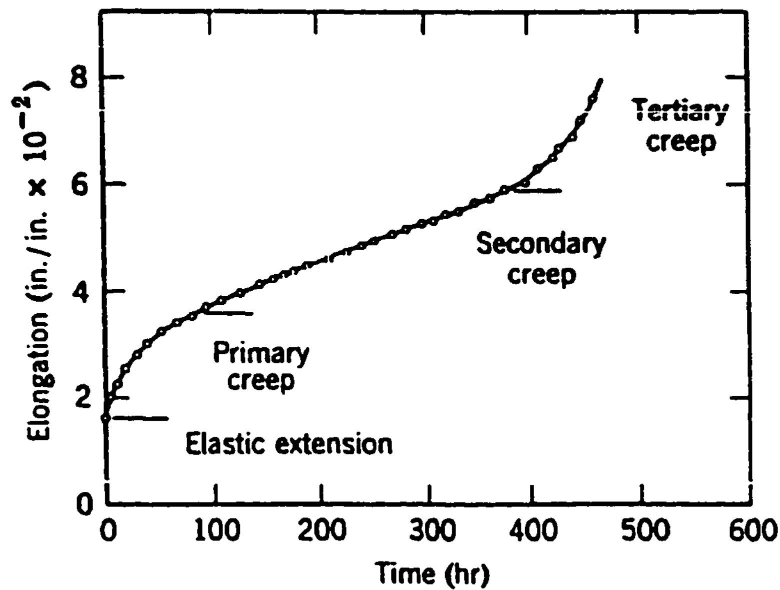

Figure 2.5 Typical creep curve for a monolithic material (Kingery et al 1976)

$$\dot{\varepsilon} = A\sigma^{n}e^{-Q/RT} \tag{2.5}$$

where $\dot{\varepsilon}$ is the steady-state strain rate, σ is the applied stress, A is a material constant, n is the stress exponent, Q is the activation energy for creep which explains the dependence of the creep rate on temperature, and RT is the gas constant times the absolute temperature. In general, the creep deformation is characterized by the stress exponent and the activation energy.

The creep behaviour of silicon nitride depends on many complicated factors, such as the grade of material, the stress and temperature range, and the state of stress (Wilkinson 1994). However, experimental data in the literature suggest that only the first two stages

of creep occur in silicon nitride, i.e., primary creep and steady-state creep. In some grades of silicon nitride, creep consists only of a primary creep stage (Arons et al 1980, Wiederhorn et al 1993), and failure intervenes before steady-state creep occurs. The absence of tertiary creep is attributed to the lack of long range ductility in structural ceramics (Wiederhorn et al 1994). The classical description of creep may not be applicable for silicon nitride cearmics. In analyzing the creep behaviour of silicon nitride ceramics, Chadwick et al (1992, 1993) presented creep test data in terms of creep rate as a function of strain on a log-log plot. Based on this analysis, the concepts of exhaustion creep, steady-state creep and mixed creep were introduced by Wilkinson (1994) to classify the creep response of silicon nitride.

The term "exhaustion creep" describes the creep behaviour whereby an initial period of creep with a relatively constant strain rate is followed by a sharp drop in strain rate when the creep strain reaches a critical value at which creep essentially stops. This phenomenon has been found in four-point bending creep of SN220, a commercial sintered silicon nitride doped with 4 wt% Al_2O_3 and 4 wt% Y_2O_3 (Chadwick 1990), as shown in Figure 2.6.

In other grades of silicon nitride, such as GN10, a commercial material sintered with Y_2O_3 and other additives, under certain testing conditions the creep rate is nearly constant, decreasing very slowing during the entire creep test (Luecke and Wiederhorn 1993). This behaviour is termed steady-state creep (Figure 2.7). Mixed behaviour is shown in Figure 2.8 for NT154, a HIPed Y_2O_3-doped silicon nitride (Luecke and Wiederhorn 1993). Following a short period of constant creep, the creep rate decreases towards a new

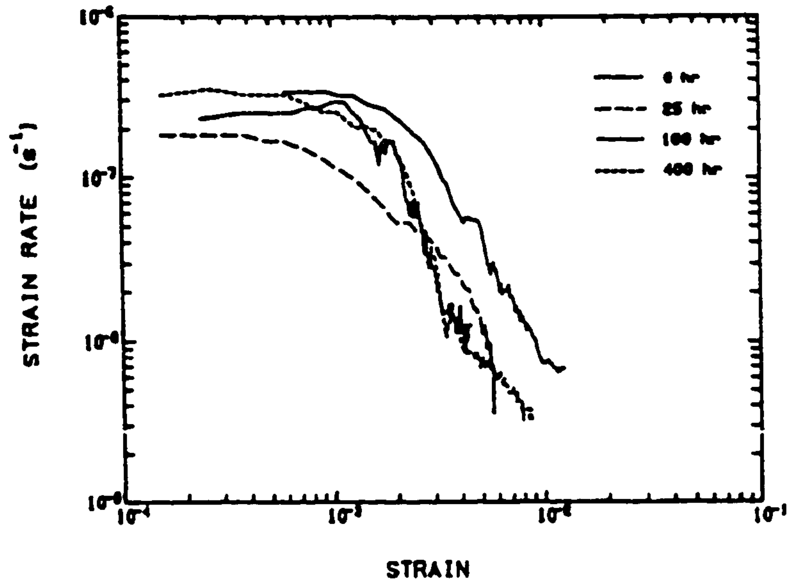

Figure 2.6 The creep response of SN220 at 1200°C and 63.5 MPa under four-point bending. Before creep the material was annealed at 1200°C from 0 to 400h (Chadwick 1990).

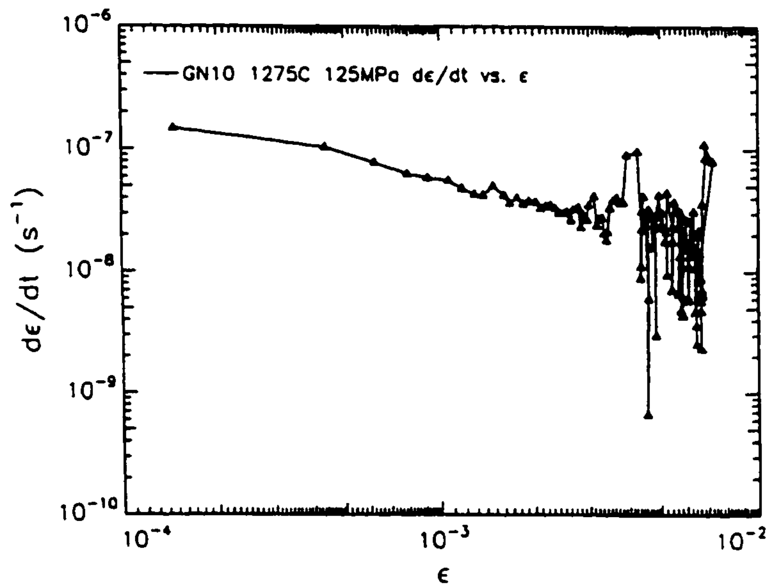

Figure 2.7 The creep response of GN 10, tested in tension at 1275°C and 137.5 MPa, showing a gradually decreasing strain rate (Luecke and Wiederhorn 1993).

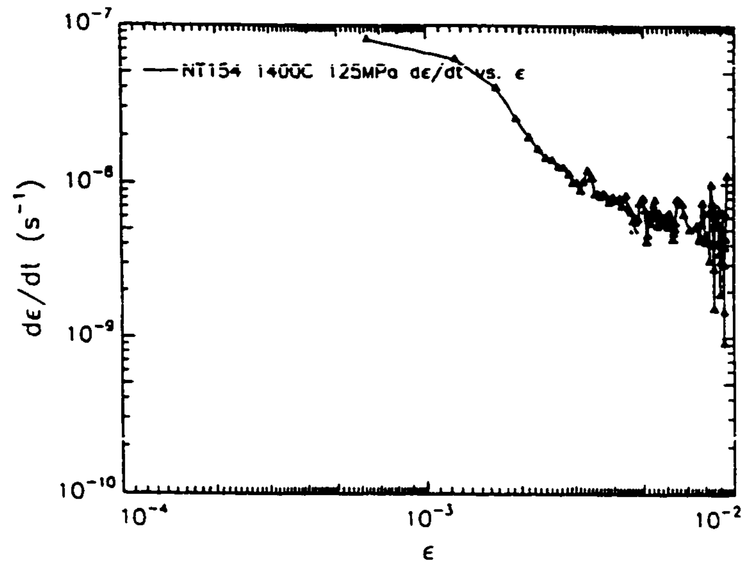

Figure 2.8 The creep response of a HIPed Y_2O_3-doped Si_3N_4, NT154, tested in tension at 1400°C and 125 MPa, two plateaus of strain rate occuring in the creep process (Luecke and Wiederhorn 1993).

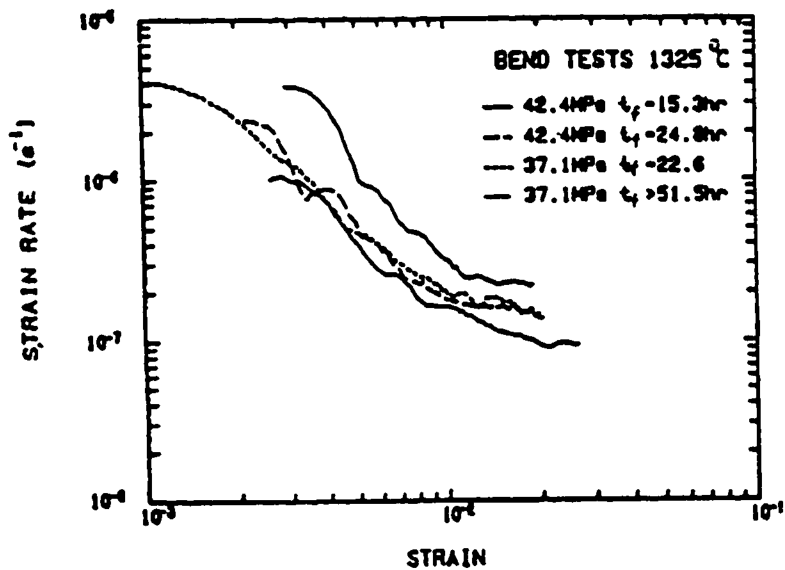

Figure 2.9 The creep response of SN220 tested in four point bending at 1325°C. Two plateaus occur during creep, which is different from Figure 2.6 (Chadwick 1990).

steady-state about one order of magnitude slower. This mixed behaviour was also observed in compressive creep of a high-purity silicon nitride and a 800 ppm Ba doped silicon nitride at 1400°C (Jin 1995).

It is evident that different materials may have different creep responses. However, the creep response depends not only on the material, but also on the testing temperature. Figure 2.9 illustrates the creep curve of SN220, tested at 1325°C in four point bending (Chadwick 1990); two plateaus occur, which is different from the creep curve shown in Figure 2.6 for the same material tested at 1200°C, where only one plateau occurs.

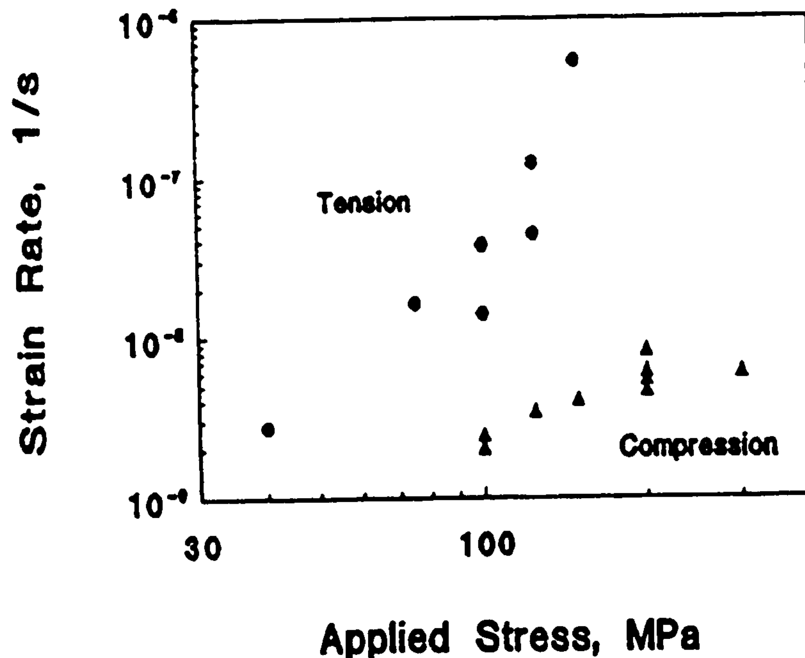

Figure 2.10 Creep of NT154 at 1430°C, showing creep asymmetry. Under the same applied stress, the creep rate in tension is from 10 to 100 times that in compression (Wiederhorn et al 1994).

Silicon nitride also exhibits creep asymmetry. The creep behaviour in tension and in compression can be totally different. For example, it has been found (Wiederhorn et al 1994) that in NT154 tested at 1430°C, for the same applied stress, the creep rate in tension is from 10 to 100 times greater than that in compression, as shown in Figure 2.10. This creep asymmetry only occurs in ceramics containing a softer phase at the grain bondaries.

2.4.2 Creep Models

Solid granular materials can creep either by changing the shape of the grains or by grain boundary sliding (Wiederhorn et al 1993), which can be attributed to dislocation motion, diffusional creep, or cavitation in most materials. If the solid contains an intergranular amorphous phase which is softer than the solid grains, then it can also creep by flow of the amorphous phase from one part to another, i.e., redistribution of the intergranular amorphous phase in the solid (Lange 1972, Dryden et al 1989, Chadwick et al 1992, 1993, Jin 1995). The dominant mechanism depends on the testing conditions, the microstructure of the material, and the quality and quantity of the intergranular amorphous phase. Now it is clear that the creep deformation of glass-containing ceramics may occur by several mechanisms, which have been modelled by previous investigators on the basis of their experimental results, and these are discussed next.

(1) Creep due to viscous flow creep

In this model, it is assumed that only the viscous glass phase deforms under stress. While the solid grains (e.g. Si_3N_4) do not change shape, relative displacement between the rigid grains can occur. This process is accommodated by flow of a viscous phase from high pressure grain boundaries to low pressure ones. The rate of change in grain boundary thickness will determine the overall creep rate. So far, several models have been proposed to describe viscous flow in ceramics containing a glass phase. Generally, two geometries have been used to treat the microstructure of silicon nitride. In two-dimensional analyses, both cubic grains (Lange 1975, Pharr and Ashby 1983) and hexagonal grains (Drucker 1964, Dryden et al 1989, Chadwick et al 1992) are used, while recently the three-dimensional problem has been treated using cubic grains (Dryden and Wilkinson 1997).

The earliest and simplest model was proposed by Lange (1975). He considered two cubic grains separated by an intergranular fluid. By using a solution for the rate of squeezing of a liquid layer between two surfaces as described in lubrication theory (Bikerman 1965), the bulk strain was found to vary as a function of the initial boundary thickness and the instantaneous value of thickness at that time. Pharr and Ashby (1983) considered the same geometry for the grains and assumed that the microstructure consists of an array of cubes of size d separated by an incompressive fluid of thickness w and viscosity η (Figure 2.11), then the calculated shear strain rate ($\dot{\varepsilon}$) is given by

$$\dot{\varepsilon} = \alpha\left(\frac{w}{w+d}\right)\frac{\bar{\sigma}}{\eta} \qquad (2.6)$$

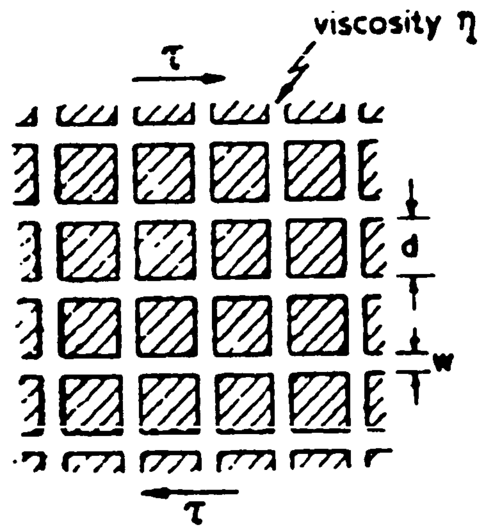

Figure 2.11 Model for viscous flow creep based on the assumption of cubic grains (Pharr and Ashby 1983).

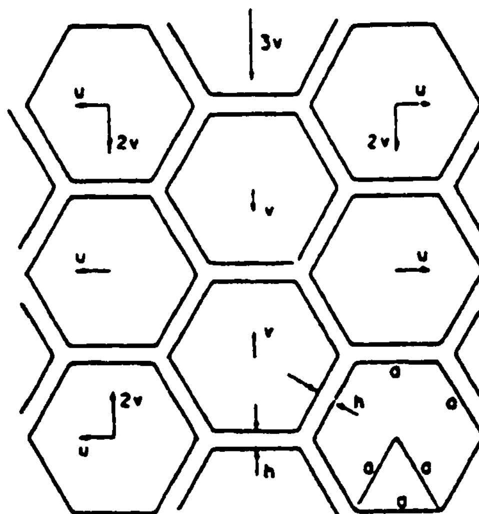

Figure 2.12 Two-dimensional model for incompressible fluid between rigid hexagons (Drucker 1964).

where $\overline{\sigma}$ is the deviatoric stress and α is a constant (about 1/3). This model involves free lubricated sliding of one grain over another. The strain rate is predicted to have a linear dependence on deviatoric stress, no dependence on pressure and exponential dependence on temperature through viscosity. Obviously, the geometry of grains is oversimplified and this mode of deformation is highly idealized since, in reality, grain boundary sliding is rapidly constrained by neighbouring grains.

The assumption of hexagonal grains separated by an incompressible fluid (Figure 2.12) offers a more realistic representations of the microstructure of Si_3N_4. This was first proposed by Drucker (1964), who calculated the average strain rate as a function of stress, viscosity and volume fraction of the amorphous phase. The average strain rate ($\dot{\varepsilon}$) is given by

$$\dot{\varepsilon} = \frac{\sigma}{\eta\sqrt{3}}\left(\frac{H}{L}\right)^3 \tag{2.7}$$

where σ is the far field applied stress, 2L is the grain facet length, 2H is the bonding phase thickness, and η is the viscosity of the bonding phase.

Drucker's model can only be applied at zero strain when the glass layer thickness is equal on all facets. Dryden et al (1989) therefore extended the model by considering the strain dependence of the creep rate for linear viscous flow. This model was further developed to include non-linear viscous flow (Chadwick et al 1992, Dryden and Wilkinson 1998). The strain rate ($\dot{\varepsilon}$) due to viscous flow is found to be (Dryden and Wilkinson 1998)

$$\dot{\varepsilon} = \dot{\varepsilon}_0 \left[\frac{|\sigma|}{\sigma^*} \right]^n S(\varepsilon_N) \tag{2.8}$$

where

$$\sigma^* = \frac{2n(1+2^{1/n})}{3(2n+1)} \left[\frac{2^{n+1}(n+2)}{3^{(n+1)/2}} \right]^{1/n} \frac{\sigma_0}{f^{(n+2)/n}} \tag{2.9}$$

$$S(\varepsilon_N) = (1+2^{1/n})^n \frac{(1+2\varepsilon_N)^{n+2}(1-\varepsilon_N)^{n+2}}{[(1+2\varepsilon_N)^{(n+2)/n} + 2^{1/n}(1-\varepsilon_N)^{(n+2)/n}]^n} \tag{2.10}$$

Here ε_N is the normalized strain equal to ε/f, and ε is the strain in the direction of the stress axis, f is the normalized glass layer thickness at zero strain ($f=2H/\sqrt{3}\,L$), and $\dot{\varepsilon}_0$, σ_0 and n are material constants. When n=1, $\sigma_0=1/\eta$, representing the result for a Newtonian glass.

The predicted strain rate behaviour due to linear and nonlinear viscous flow (for n=1,2, and 3) is shown in Figure 2.13. The model predicts a nearly constant strain rate at low strains followed by a rapid decrease in strain rate as the maximum strain is reached. Similar creep behaviour is expected for tension and bending using this model. Three-dimensional models (Dryden and Wilkinson 1997a, 1997b) are generally consistent with the two-dimensional results. This predicted creep response can be easily explained by the well-known phenomena described in lubrication theory (Bikerman 1968, Cameron 1976). The viscous fluid layer can be squeezed out from between two parallel plates under a compressive load. The rate of approach of the two plates is very sensitive to the current plate separation. Therefore, as the separation decreases the resistance to further squeezing

increases and the rate of separation drops. In a polycrystalline material containing an amorphous grain-boundary phase, like silicon nitride, the fluid is driven by the gradient of the normal stress acting on the adjacent facets. Strain is accumulated as fluid is squeezed out of the compressive boundaries. When the adjacent approaching grains eventually become interlocked, creep due to viscous flow stops. According to this model, the maximum strain equals the fraction of intergranular viscous phase in tension and half that value in compression. This creep asymmetry is inherent in glass-containing ceramics because in a microstructure of, for example, cubic or equiaxed grains,

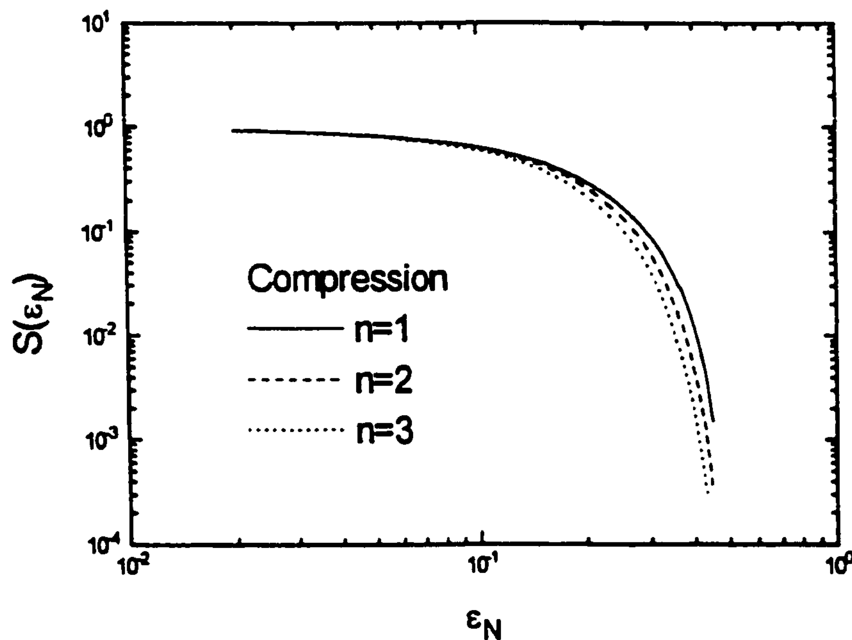

Figure 2.13 Strain dependence term of the creep rate $S(\varepsilon_N)$ as a function of normalized strain $\varepsilon_N=\varepsilon/f$ predicted theoretically from equation 2.8 (Jin 1995).

2/3rds of the grain boundaries can receive glass during compression, but only 1/3rd can during tensile creep. Therefore, this leads to a strain asymmetry factor (i.e., ratio of the maximum strain in tension to that in compression) equal to 2.

It should be mentioned that the viscous flow models (Dryden et al 1989, Chadwick et al 1992) assume that the maximum strain due to viscous flow corresponds to the situation in which all the glass (2H thick) is squeezed out from between grain boundaries in compression. Both theoretical work (Clarke 1987, 1993) and experimental observations (Jin 1995) indicate that the equilibrium thickness of a grain boundary subjected to a compressive stress is not zero but has a finite and stress dependent thickness (2H*). Wilkinson (1998) recently corrected this simplification made in the models by introducing the concept of the effective thickness of the grain boundary layer, i.e., 2H-2H*. Thus, all the results obtained from the models remain valid by replacing H with H-H*.

(2) Creep due to grain shape change: dissolution-reprecipitation and dislocations

This model ascribes the creep deformation of polycrystalline ceramics that contain a residual glass phase to material transport through the glass phase. The diffusional creep in single phase polycrystalline materials has been widely discussed in the literature (Herring 1950, Coble 1963). If there is a liquid phase in the grain boundaries, in which the grains are partly soluble, then deformation could occur by diffusional transport if the rate of dissolution and reprecipitation is rapid enough (Durney 1972). Apparently, a fast path of transport through the glass phase at the grain boundary favours Coble creep (Coble 1963) over Nabarro-Herring creep (Nabarro 1948, Herring 1950) as a deformation mechanism.

It is thus reasonable to attribute the deformation caused by solution-reprecipitation in glass-containing ceramics to Coble creep, but with grain boundary diffusion replaced by diffusion through the bonding phase.

The liquid enhanced solution-reprecipitation process has been investigated in a variety of systems (Raj and Chyung 1981, Raj 1982, Pharr and Ashby 1983). Pharr and Ashby (1983) studied the creep of porous KCl in both the dry state and with the pores filled with kerosene or a saturated solution of KCl in water. The viscosities of kerosene and water are almost the same. However, kerosene has no solubility for KCl and water has a high solubility. They found that creep of porous KCl saturated with KCl solution is accelerated and the stress exponent for creep is close to unity. A lower strain rate with a higher stress exponent occurs in both the dry state and in the kerosene solution. To explain the liquid-enhanced creep behaviour, they proposed a coupled-plasticity-plus-dissolution model in which the liquid must wet the grain boundaries of the solid. The role of the liquid is to reduce the sections of the necks by dissolution, which in turn, causes an increase in local stress and further creep deformation. This process leads to steady-state flow and the rate of deformation depends on both the yield strength of the solid and kinetics of dissolution and diffusion in the liquid.

Raj and Chyung (1981) were the first to model the dissolution-reprecipitation creep. Their experimental basis was the linear dependence of the strain rate on the stress when they investigated the creep behaviour of a glass ceramic. They proposed that the rate of creep is proportional to the rate of solution/precipitation, which can be limited either by the

interface reaction kinetics or the transport through the grain-boundary phase. The slower of these two processes is rate controlling.

The driving force for matter transport depends on the existence of a gradient of the normal traction along the surface of a grain. In other words, maintaining the pressure differentials is required for the solution/reprecipitation process. Another precondition for this process is the presence of a grain boundary phase. At the time this mechanism was first proposed, our understanding of the nature of grain boundary amorphous phase was very poor (Wilkinson 1998). It was then assumed that such an amorphous film at grain boundaries could not support a normal load since it would be rapidly squeezed out from between the grains. Thus Raj and Chyung (1981) introduced the concept of an island strucuture at grain boundaries. The islands represent regions of grains in contact across a boundary. Surrounding these islands are channels of the amorphous phase. In this structure the stresses are supported only at the islands and it is thus possible to sustain stress gradients while the amorphous phase would not be squeezed out from between grains. More recent work, both experimental and theoretical, has demonstrated that the intergranular amorphous film is indeed stable against a normal load without the requirement of island structure at grain boundaries. In the absence of an island structure at grain boundaries, the solutions of Raj and Chyung (1981) for creep rate can be modified to remove the dependence of the fraction of grain boundary available for mass transport. For creep controlled by diffusion through the glass phase, the constitutive equation for creep rate is given by (Wilkinson 1994)

$$\dot{\varepsilon} = \frac{Kc\sigma H}{L^3\eta} \tag{2.11}$$

where K is a material constant, c is the molar fraction of the diffusing species in the glass, σ is the applied stress, H is the half thickness of the grain boundary phase, L is the grain size, η is the viscosity of the glass phase. For creep controlled by the kinetics of dissolution, the creep rate is given by (Wilkinson 1998)

$$\dot{\varepsilon} = \frac{\sigma\Omega\kappa}{2kTL} \tag{2.12}$$

where Ω is the atomic volume and κ is the rate constant for dissolution, kT is the Boltzmann constant times the absolute temperature.

Dislocation motion is another mechanism which can change the shape of the grains. Unlike metallic materials, however, dislocation creep is generally assumed to be negligible in silicon nitride, because there is no clear evidence that dislocations are generated or that they move at the creep tempertures (Kossowsky et al 1991, Lange et al 1980a, Wiederhorn et al 1993). Lange et al (1980a) studied the compressive creep behaviour of four grades of silicon nitride and found no indication of dislocation structures that could be taken as evidence of dislocation generation. Wiederhorn et al (1993) conducted extensive studies on the tensile creep behaviour of a number of grades of silicon nitride in the temperature range of 1370 to 1430°C, and reached the same conclusion. The commonly accepted view about silicon nitride is that dislocations are immobile at temperatures below 1700°C (Evans et al 1971, Kossowsky 1973). According to

Wiederhorn et al (1993), although dislocations are observed in silicon nitride, the microstructure before and after creep deformation is similar, and no clear evidence could be found for the dislocation motion during the creep process. It should be mentioned that the dislocation density in silicon nitride was found to increase due to crystallization of β-$Y_2Si_2O_7$ at 1500°C in a Y_2O_3-fluxed silicon nitride (Lee et al 1988). Din and Nicholson (1975) also found dislocations near voids on the tensile side of bending samples crept at 1400°C. The question arises as to how much strain can be attributed to dislocation motion if dislocations were indeed active in silicon nitride at creep temperatures. Kossowsky (1973) also found dislocation tangles in the deformed material. However, the calculated dislocation strain contribution was less than 10^{-5}. Thus, it seems that dislocation motion is not a dominant creep mechanism even though dislocations are active in silicon nitride. So creep deformation by changing the shape of the grains can only occur through a diffusional process.

(3) Creep due to cavitation

The experimental evidence for this model is the ocurrence of cavitation in the crept material containing an intergranular amorphous phase. Cavitation may occur in the triple glass pockets or at two-grain boundaries. This has been repeatedly reported in the literature. For example, Lange et al (1980a) studied the compressive creep of Si_3N_4/MgO alloys and found wedge-shaped cavities at triple junctions and glass fibrils caused by cavitation between two grains which separated in a direction normal to their common boundary. Tighe et al (1984) found cavities and cracks in the microstructure of a Y_2O_3 doped material as the material was deformed. Extensive investigations on cavitational

creep in a 4 wt% Y_2O_3-doped material, NT154, have been made by Wiederhorn and his coworkers (1993, 1995). They found that cavitation contributes substantially to tensile creep of this material. The volume fraction of cavities increased linearly with strain and accounted for about 90% of the total strain. Among these cavities, most are at triple junctions as irregular or wedge shaped voids with only a small portion at two-grain boundaries as lenticular shaped or crack-like cavities. Multigrain junction cavities tend to be formed in the fine-grained regions where most of the residual glass is located, varying in size from several nanometers to about 1 micron (Marion et al 1983, Wiederhorn et al 1993). The morphology of cavities at two-grain boundaries depends on the chemical composition of the sintering aids (Wiederhorn 1993). It has been found (Lou et al 1978, Wiederhorn et al 1993, Yeckley et al 1989, Hockey et al 1991, Ferber et al 1992) that the lenticular cavities occur primarily in silicon nitride containing the more refractory sintering aids such as rare earth oxides. For silicon nitride with less refractory sintering aids such as Y_2O_3 + SrO, crack-like cavities form along the grain boundaries (Wiederhorn et al 1993). In both cases, the cavities initially nucleate in the grain boundary amorphous film, and then grow into the adjacent silicon nitride grains. The observed cavities are usually much larger than the thickness of the amorphous films between silicon nitride grains. Cavity growth seems to occur by the Hull-Rimmer process (Hull and Rimmer 1959) in which silicon nitride diffuses along the surface of the cavity into the amorphous grain boundary. Chuang and co-workers first described the origin of the difference in cavity morphology (Chuang et al 1973, 1979, Chuang 1982). They suggested that if diffusion is more rapid along the cavity surface than along the grain boundary, the cavity maintains its equilibrium lenticular shape. However, if diffusion is more rapid along the grain boundary than along

the cavity surface, then crack-like cavities form since the equilibrium shape cannot be maintained.

A comprehensive analysis of creep due to cavitation should include cavity nucleation and growth. Cavity nucleation has attracted much attention as an important aspect of creep failure, but our current understanding of this process is still far from clear. In a material containing a continuous amorphous phases such as in silicon nitride, cavity nucleation is expected to occur primarily within the amorphous phase. In general, both the thermodynamics and kinetics have to be considered in modelling cavity nucleation. Thermodynamics requires that the amorphous phase at the nucleation site is of sufficient size to accommodate a critical nucleus. If the nucleation site is large enough, such as some multigrain junctions, then a cavity may form a stable spherical shape. Otherwise, other shapes must form due to the constraints of geometry. For example, oblate cavities may form at the two-grain interfaces. Classical nucleation theory has been used to predict the cavity nucleation rates (Marion et al 1983, Thouless et al 1984). They are determined from the product of the number of nuclei at the critical size with the probability that the cavities will be enlarged to a supercritical size by the addition of a vacancy (Raj and Ashby 1975). If the cavity nucleation rate is set to a prescribed value, then the critical stress for cavity nucleation can be predicted.

Based on the above mentioned considerations, Marion et al (1983) and Thouless et al (1984) calculated the critical nucleation stresses for spherical cavities at triple junctions and oblate cavities along two-grain boundaries, and the results are shown in Figure 2.14 in terms of critical stresses as a function of temperature. The critical stresses predicted by

the model are generally much greater than the applied far field stress. This stress concentration could be produced however by either microstructural inhomogeneities or local stress transients. It is generally accepted (Dalgleish 1984) that the stress enhancement due to the presence of large-grained regions or inclusions is not sufficient. Most likely, therefore, large transient tensile stresses must be produced by abrupt grain boundary sliding and be responsible for the cavity nucleation. In analysing cavitation in triple junctions. Tsai and Raj (1982) proposed that grain boundary sliding can cause dilation of the interstitial free spaces in a granular solid. Thus, a negative pressure may develop within the intergranular phase which fills these spaces. On the other hand, grain boundary sliding can also induce very high transient tensile stresses on some grain boundaries. Page et al (1987) found that in liquid phase sintered alumina the cavity spacing after creep corresponds to that for grain boundary ledges, suggesting the ledges act as nucleation sites. It should be noted that even if the applied stress is compressive, nucleation may still occur at regions that are under local hydrostatic tension (Lange et al 1980a).

Cavity growth in silicon nitride is expected to occur primarily by viscous flow of the grain boundary amorphous phase or solution-reprecipitation process by surface diffusion in series with diffusion through this amorphous phase. Evans and Rana (1980) were the first to model the cavity growth process by viscous flow. They assumed that the amorphous phase is deposited by viscous flow along the cavitating boundaries with spatial uniformity, thus establishing an expression for cavity growth rate. The driving force is the stress differential between a cavity and its surrounding area.

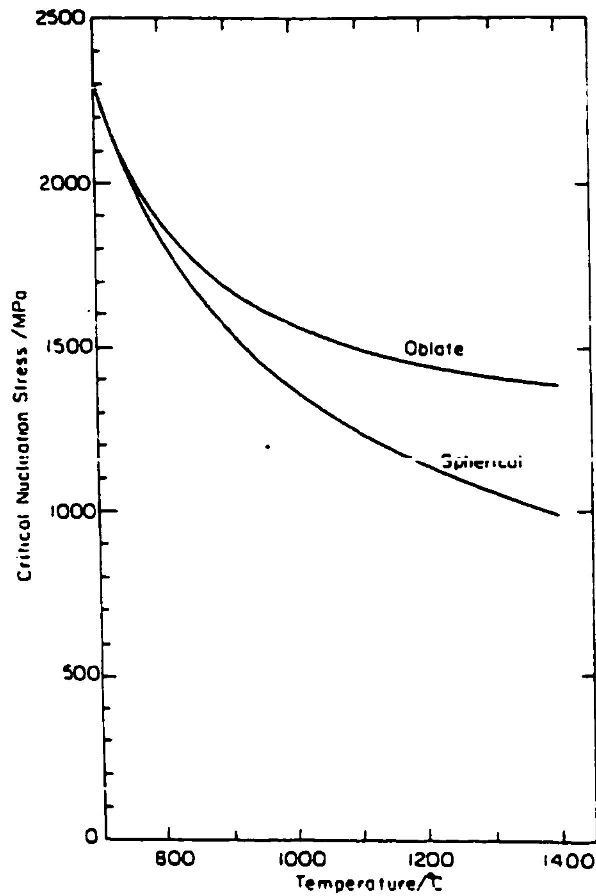

Figure 2.14 Plot of critical nucleation stresses for spherical and oblate cavities for hot-pressed silicon nitride (Thouless et al 1984).

It is generally assumed in most cavitation models that the cavities formed at the triple junctions and at the two-grain boundaries grow along the grain boundaries and form microcracks (i.e., full facet cavities according to Marion et al 1983). Coalescence of these microcracks can form cracks. The cracks so formed continue to grow under the applied stress, and creep failure ultimately occurs from one of these cracks. The effect of stress on

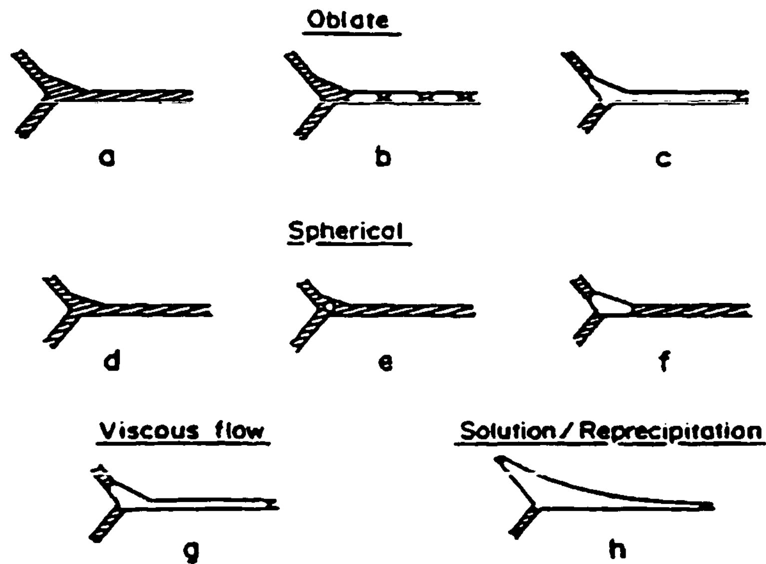

Figure 2.15 Schematic diagram illustrating the microcrack formation process. (a) uncavitated interface, (b) nucleation of oblate cavities along two-grain boundary,(c) coalescence to a full-facet microcrack, (d) an uncavitated triple pocket, (e) nucleation of a spherical cavity in the glass, (f) depletion of the pocket by viscous flow,(g) expansion to full-facet microcrack by viscous flow,(h) growth to full-facet size by solution-reprecipitation at low stress (Marion et al 1983).

the microcrack formation process is depicted in Fig.2.15 (Marion et al 1983). If the stress is high enough to nucleate cavities within two-grain interfaces, full-facet cavities develop by the growth and coalescence of the oblate cavities. If the stress is below that required to nucleate cavities on two-grain boundaries, but above that needed to nucleate cavities within triple pockets, then cavity growth occurs by the viscous flow of the glass phase into the adjacent two grain channels, or by solution-reprecipitation of the solid phase from the cavity surface to the grain surface within the channel. In the second case, cavities larger in size than the original grain pockets are expected, and this has been observed in silicon nitride and alumina (Marion et al 1983, Clarke 1985).

The lifetime to failure of materials depends on the time for cavity nucleation and microcrack formation, and crack growth rate. Expressions for these have been given by Tsai and Raj (1982) and Evans and Rana (1980). For example, an estimate for the time (t_c) required for cavity growth within the triple junctions is (Tsai and Raj 1982)

$$t_c = 20\eta / P \tag{2.13}$$

where η is the viscosity of the grain boundary phase and P is the hydrostatic tension in the triple junctions.

It should be pointed out that another mechanism for creep failure has been proposed by Wiederhorn et al (1994). Instead of forming cracks, cavities may nucleate and grow continuously during creep deformation. This can lead to the accumulation of substantial strains which trigger failure (Wiederhorn et al 1994). Obviously, cavitation and the acompanying dilation of the material result in a strain rate. Each cavity gives an increment of strain to the total creep deformation. The strain rate depends on the rate of cavity nucleation and growth. According to Wiederhorn et al (1994), cavitation occurs at the most highly stressed area, relaxing the stress locally and transfering it by grain boundary sliding to some other areas in the structure. The rate of grain boundary sliding is supposed to determine the rate at which cavitation occurs in the solid. With continuing creep, the strain accrues with an increase in the fraction of cavitation.

As indicated by Thouless et al (1987), a complete understanding of cavitation processes must include a detailed analysis of cavity formation and growth in conjunction with a

exact expression for the transient stresses. This is by no means realistic due to a number of stochastic aspects of the processes. Implications of the stochastic nature of cavitation have been discussed by Page and Chan (1987) in terms of the cavity nucleation, growth and coalescence processes.

2.4.3 Explanation of Creep Behaviour

The models discussed above are all possibly responsible for the creep behaviour of silicon nitride. However, it seems difficult to explain the typical creep curve (as shown in Figures 2.8-2.9) using a single mechanism. The occurence of steady-state creep after exhaustion creep indicates at least two creep mechanisms must be involved. It is now generally accepted that exhaustion creep is due to viscous flow of the amorphous phase at grain boundaries, whereas steady-state creep is due to cavitation or dissolution-reprecipitation creep.

The curves of strain rate versus strain predicted by the viscous flow model are consistent with the initial part of creep curves in some materials (Compare Figure 2.13 with Figures 2.6, 2.8-2.9). Both the experimental and theoretical data show an initial relatively constant strain rate followed by a rapid decrease in strain rate as the strain approaches a limiting value. According to the viscous flow models (Dryden et al 1989, Chadwick et al 1992) the limiting value scales as the ratio of the grain boundary thickness to the grain size. The widths of these films have been measured for a variety of compositions (Kleebe et al 1993a, 1993b, Jin 1995, Wang et al 1996). They are found to have a distinct value which depends on the composition of the films and varies in a range from 0.5 ~ 2 nm. This yields

strains of about 0.05%-0.2% if we assume the grain diameter is about 1 μm and all the glassy films at grain boundaries under compression are squeezed out completely. This is in approximate agreement with the experimental data (Chadwick 1990). Direct evidence of viscous flow creep was also obtained by comparing the film thickness distribution before and after creep in a high-purity silicon nitride and a Ba doped silicon nitride (Jin 1995). Using the Fresnel fringe imaging technique, we measured the widths of a number of grain boundary films in each material and found that the film thickness is confined to a narrow range in the as-sintered materials. However, the standard deviation of the film thickness distribution of a given material is considerably larger after creep than before while the mean value remains unchanged. These results suggest that redistribution of the grain boundary glass phase indeed occurs during creep deformation.

Both dissolution-reprecipitation and cavitation have been proposed as the mechanisms responsible for steady-state creep (Lange et al 1980a, Kleebe et al 1994b). The constitutive equation for the dissolution-reprecipitation process (equation 2.8) predicts a linear relationship between the creep rate and the applied stress. Lange et al (1980a) studied the compressive creep of four compositions within Si_3N_4/MgO alloys, and found that two compositions with less glass phase exhibited no cavitation and had a stress exponent of $n \approx 1$, sugesting the existence of the dissolution/reprecipitation mechanism. However, the other two compositions with more glass phase exhibited extensive cavitation and had a stress exponent of $n \approx 2$, suggesting another mechanism, i.e. cavitation. Based on the observations, they concluded that both dissolution/reprecipitation and cavitation mechanisms exist during steady-state creep of silicon nitride. A shift from one mechanism

to another depends on the additive composition. Similar conclusions have also been reached in our study on the compressive creep behaviour of undoped and Ba doped silicon nitride ceramics (Jin 1995). The Ba doped material gave a stress exponent of 2.6 and exhibited extensive cavitation. A large number of strain whorls were also observed at grain boundaries in the crept material. We ascribed the steady state creep of this material to grain boundary sliding accommodated by cavitation. The undoped material, however, exhibited no cavitation or strain whorls and had a stress exponent of about 1. This suggests that creep occurs by dissolution of silicon nitride from grain boundary in compression and reprecipitation to those in tension. Luecke and Wiederhorn (1994) analysed extensively the 1430°C creep of NT154, a commercial grade of silicon nitride doped with Y_2O_3 and found a significant difference between compressive creep and tensile creep of this material. In compression, this material creeps at a much lower rate than that in tension and the stress exponent is unity. In tension, however, the creep rate is 10~100 times faster than that in compression, and the stress exponent rises to 4. Furthermore, density measurements indicate cavitation contributes negligibly to the strain in compression, whereas in tension cavitation can account for about 85% of the creep strain. The cavity morphology observed at the two-grain boundaries suggests that cavity growth occurs by a diffusive process as predicted by theoretical models. The material diffuses from the cavity surface to the grain surface within two-grain channels and results in cavities larger in size than the original grain boundary thickness. Clearly, the creep behaviour in compression of NT154 suggests a solution-reprecipitation mechanism, whereas cavitation leads to tensile creep. In the latter case, the total strain scales linearly with the volume fraction of cavities produced in creep.

Wilkinson (1994) has given a comprehensive explanation of the different creep responses exhibited in silicon nitride. For the mixed behaviour of the exhaustion creep and steady-state creep (as shown in Figure 2.7), he suggests that the initial creep period is controlled by viscous flow of the intergranular glass phase, until this process is exhausted by grain impingement and a new equilibrium film thickness is established between two-grain boundaries under the applied stress. The creep rate then decreases and another mechanism appears following the viscous flow process. This suggests that the activation energy for viscous flow is smaller than that for the steady-state mechanism. According to his explanation, the temperature is very important in determining the creep response of silicon nitride. At lower temperatures the steady-state creep rate is too low and only viscous flow creep is seen, exhibiting an exhaustion creep. At higher temperatures, the viscosity of the grain boundary glass phase is too low, and thus the viscous flow process is exhausted so quickly that it is incorporated into the initial loading transients, and only steady-state creep can be seen.

2.4.4 Effect of Oxidation and Crystallization on Creep Behaviour

The presence of intergranular glass in silicon nitride ceramic materials has a strong influence on their high temperature properties. As mentioned above, softening of this glass phase can promote grain boundary sliding, cavitation creep and diffusional creep. Changing the glass composition may change the properties of the glass phase dramatically, thereby influencing the high temperature properties. For example, even small variations in grain-boundary film chemistry strongly influence the resulting film thickness. Obviously, the creep resistance of glass-containing ceramics is sensitive to the

efficiency of the grain boundary amorphous layers as transport paths for major species (Si, N) in diffusional creep. Therefore, the effect of oxidation and partial crystallization of the amorphous phase on creep behaviour should not be neglected, especially when these processes occur at the same time scale as the creep tests.

Crystallization of the grain-boundary amorphous phase has been proposed by several researchers (Tsuge et al 1975, Smith et al 1980) as a method for increasing the high temperature properties since it reduces the glass content. Secondary crystalline phases may form from the intergranular liquid in silicon nitride during cooling from the sintering temperature if the cooling rate is slow enough, thus leaving small amounts of residual intergranular glass in the microstructure (Clarke et al 1978, Krivanek et al 1979, Lange 1980). They can also form by a post-sintering heat treatment (Lewis et al 1980, Falk et al 1987). Tsuge et al (1975) demonstrated that the high temperature strength of silicon nitrides improved significantly when $Si_3N_4.Y_2O_3$ is crystallized. In the Si_3N_4-Y_2O_3 system, characterization of the crystallization products was also conducted by Rae et al (1975) and Lee et al (1989). In other systems, Wild et al (1972) found some evidence for the presence of $MgSiO_3$ in the grain boundary phase of Mg-containing silicon nitride. Lewis et al (1977) found that yttrium aluminum garnet could be crystallized in the yttrium SiAlON system. It is suggested (Lewis et al 1980) that the reduction in glass phase content accompanying the crystallization is associated with an improved creep resistance. Wiederhorn et al (1986) found that partial devitrification of a vitreous-bonded aluminum oxide could lower the strain rate and increase the failure time. On the other hand, crystallization of secondary phases may change the chemical composition of the residual

glass. If the impurities are not incorporated into crystalline phases formed upon heat treatment, the impuities will be concentrated in the residual glass. Kleebe et al (1994b) studied Yb_2O_3/Al_2O_3-fluxed Si_3N_4 with small additions of CaO and revealed the presence of a $Yb_2Si_2O_7$ crystalline phase. The Ca was found to segregate to the grain boundaries and increase substantially the grain boundary film thickness, resulting in a degradation of creep resistance.

Oxidation of silicon nitride can also change the composition of the intergranular glass phase. During this process, a thin protective film of SiO_2 (s) is formed according to reaction:

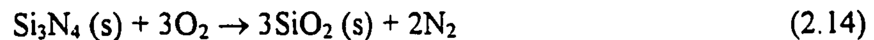

$$Si_3N_4\,(s) + 3O_2 \rightarrow 3SiO_2\,(s) + 2N_2 \qquad (2.14)$$

although in some cases, silicon oxynitride (Si_2ON_2) may form as an intermediate phase. This oxide-layer and the amorphous intergranular phase form a diffusion couple (Singhal 1976, Cubicciotti et al 1977, 1978,). The amorphous intergranular phase provides a path for the outward diffusion of additive cations, nitrogen and impurity cations, and the inward diffusion of oxygen (Cinibulk and Kleebe 1993). The presence of residual amorphous grain-boundary phases, which are never in equilibrium with SiO_2 (the oxide layer) results in the creation of a driving force for this diffusion. Therefore, oxidation can purify the chemistry of the intergranular glass film and shift it to a lower M/Si ratio (where M is the total cations present), thereby increasing the refractoriness of the grain boundary phase. Lange et al (1980a) studied the compressive creep behaviour of MgO doped Si_3N_4 materials and found that a true steady-state does not exist during the creep process. The creep rate was always observed to slowly decrease with time. They ascribed this

phenomenon to the effect of oxidation. Further work by the same investigators (Lange et al 1980b) shows that oxidation causes compositional changes and thus the creep mechanisms of the same materials shift from cavitational creep in the as-sintered state to diffusional creep after oxidation.

From the above discussions, the creep properties of the vitreous-bonded ceramics may change as the intergranular phase devitrifies or the materials are oxidized. Therefore, when microstructure development is correlated with resulting creep behaviour, crystallization or oxidation has to be considered.

Chapter 3

EXPERIMENTAL TECHNIQUES

3.1 Introduction

This chapter describes the experimental techniques and related background theories employed in microstructural and mechanical characterization of the samples. These include creep testing, TEM observations of the microstructural evolution during creep deformation, chemistry examination and intergranular film thickness measurements.

3.2 Materials

Three different materials were used in this work: a undoped silicon nitride, a 800 wt. ppm Ba doped silicon nitride and a 4 wt.% Y_2O_3 doped silicon nitride. The first two materials were provided by Dr. H.-J. Kleebe from Technische Universität Bayreuth, Germany. They were prepared from high purity Si_3N_4 powder, hot-isostatically pressed (HIPed) at 1925°C for 1h. The Y_2O_3 doped material is a commercial HIPed silicon nitride designated as NT154 (Norton/TRW Co.).

The use of high purity Si_3N_4 powder in material fabrication was to minimize the amounts of minor impurities. X-ray fluorescence (XRF) analysis indicated that the impurities such as Al, Ca, Fe, K and Na were all below 50 ppm (detectability of the current XRF analysis). It has been suggested that the properties of the intergranular amorphous phase are determined by its composition. Impurities such as Ca, Fe and Al are often present in

silicon nitride in the order of 100 ppm. Even this level of impurities could change the material properties when they are localized in the intergranular amorphous phase. So special attention has to be paid to the starting powder and sample preparation in order to have a clear understanding of the relationship between the creep behaviour and composition of the intergranular amorphous phase.

The undoped material is expected to provide a simple model system for the study of creep of silicon nitride, especially viscous flow creep, since this material has a simple microstructure which only contains β-Si_3N_4 grains surrounded by an intergranular amorphous film and the film thickness of this material in the as-sintered state has been extensively studied by other investigators (Kleebe et al 1993, Pan et al 1996). To examine the effect of a small amount of sintering aid on the microstructure and creep behaviour , a Si_3N_4 material sintered with 800 ppm Ba was used in this work. As described elsewhere (Jin 1995), there are several reasons to choose Ba as the dopant. First, Ba doped Si_3N_4 is a new grade of material which has never been investigated before. It has been found (Tanaka et al 1994b) that Ca is a grain-boundary segregant in Si_3N_4-based materials, and can change the microstructure and the creep properties. Ba, belonging to the same group in the periodic table as Ca, is expected to have a similar function. Thus the composition of silicon nitride grains will not be affected and all the dopant is used to change the composition of the intergranular amorphous phase. On the other hand, since the general microstructure will not be influenced by a small amount of dopant (800 wt ppm), quantitative comparison between materials with and without the dopant thus become possible. The Y_2O_3 doped material was chosen in this work since it has a complex

microstructure which contains secondary crystalline phases. One purpose of this work was to extend the current viscous flow models to multiphase Si_3N_4 ceramics. The observed creep behaviour and microstructural evolution during creep deformation of the Y_2O_3 doped material, therefore, can be compared with the model.

SEM (scanning electron microscopy) was used to qualitatively assess the Si_3N_4 grain morphology. Samples were prepared following the standard ceramographic techniques which include grinding using SiC paper and polishing using diamond polishing media. To obtain good representations of grain size and grain aspect ratios, the polished specimens were etched in 49% HF for 48 h to dissolve the grain boundary phase (Chadwick 1990), thereby revealing the grain morphology. Prior to examination, the etched specimens were gold-coated to prevent static charging in the SEM. Representative views of the morphology of grain structure of the as-received materials are shown in Figure 3.1. All the experimental materials contained equiaxed and elongated β-Si_3N_4 grains. The undoped and Ba doped materials have a similar grain size, ranging from 0.2 to 0.5 μm in diameter for the equiaxed grains and 0.7 to 1.5 μm in length for the elongated ones. The Y_2O_3 doped material exhibits a larger grain size, which is about 0.2 to 1 μm for the equiaxed grains. The bright contrast of some grains suggests the presence of secondary phases which have different chemistry compared to Si_3N_4. Additional microstructural information was obtained using thin foils in the TEM, which will be described in detail in Chapter 5.

(a)

(b)

(c)

Figure 3.1 SEM microstructure of the experimental materials, (a) undoped, (b) 800 ppm Ba doped, and (c) 4 wt.% Y_2O_3 doped, showing the equiaxed and elongated Si_3N_4 grains. The bright grains in (c) represent secondary crystalline phases which contain yttrium.

3.3 High Temperature Creep Tests

Flexural tests are most commonly used to study the strength and creep resistance of structural ceramics at high temperatures since they are experimentally easy to perform. However, ceramics generally creep more rapidly in tension than in compression (Wiederhorn et al 1988, Morrell et al 1973, Wiederhorn et al 1986), which results in time and strain dependent changes in the stress distribution and position of the neutral axis when tests are conducted in flexure. As a consequence, accurate calculations of stress and strain require the creep data be obtained in both tension and compression. In the present work, both tension and compression tests were used to investigate the creep behaviour of the experimental materials.

3.3.1 Tension Tests

The study of the Y_2O_3 doped silicon nitride involved a collaboration with Drs. W.E. Luecke and S.M. Wiederhorn from the National Institute of Standards and Technology (NIST). Thus the tensile creep tests were performed by Luecke at NIST. The creep specimens of 2 mm × 2.5 mm cross section were tested at 1430 ±1°C under different stresses. Figure 3.2 shows the shape and dimensions of the specimen tested. The strain produced in tensile creep was measured continuously using a laser extensometer. The gauge length of the specimen was marked with two SiC flags attached to the gauge section. The laser extensometer consisted of a detector and a HeNe laser that scanned in a vertical line (Figure 3.3). Both the laser and the detector were protected from the heat of

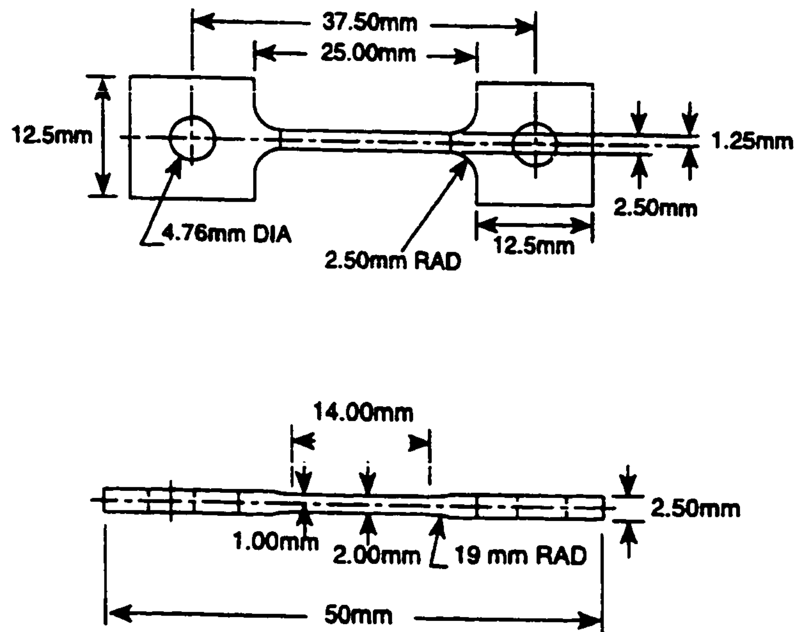

Figure 3.2 The tensile creep specimen used in this study (Luecke et al 1995).

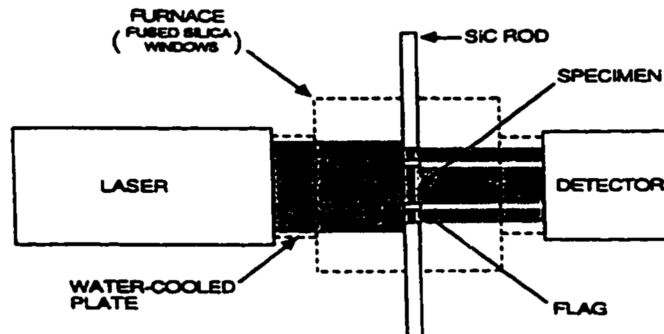

Figure 3.3 Schematic diagram for the laser extensometer used for measuring tensile creep deformation (Carroll et al 1989).

the furnace by water-cooled plates which were attached to the front of each unit. The laser passed through a silica glass window of the furnace toward the gauge section of the specimen and was interrupted by the two flags. A detector received the vertical scan from the furnace and sensed the interruption of the laser by the flags, thus measuring the gauge length of the specimen. By using a computer, the laser extensometer recorded the movement of the flags as a function of the time. This technique introduces several potential errors into the strain measurement that limit the accuracy of the measured strain to about ±10%. The origins of these errors and detailed description of the tensile creep testing procedure can be found elsewhere (Carroll et al 1989, Luecke et al 1995).

3.3.2 Compression Tests

Compressive creep specimens, approximately 2 x 5 x 7 mm^3, were also used in the present investigation. Special attention was paid to ensure the parallelism of the two end surfaces (±0.05mm). The specimen was "sandwiched" into two 10 mm thick SiC platens by using five-minute epoxy. When the glue had set, the rig was placed in the center of a furnace. The rig was loaded lightly, to prevent it from collapsing when the epoxy burned off at 300-400°C.

The testing machine was a resistance-heated furnace with loading and extensometer assemblies. The loading jig uses the lever arm principle. The extensometer consisted of three probes of alumina rods which were attached to a LVDT (linear variable differential transducer). The LVDT measured the relative displacement of the platens. As shown in Figure 3.4, the center probe was in contact with the lower platen and the two others were

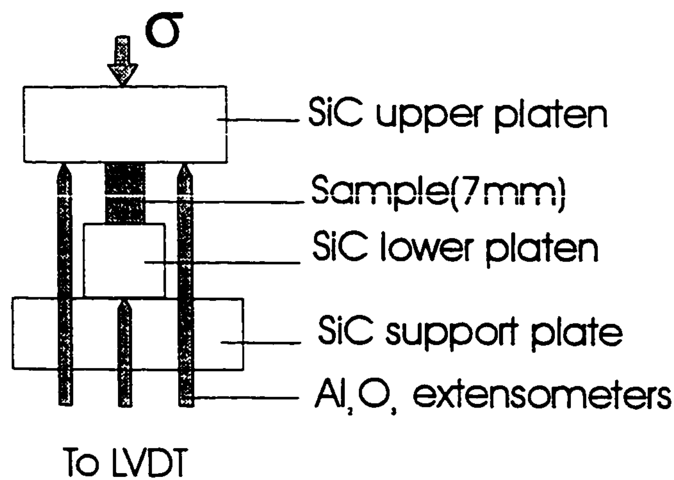

Figure 3.4 Schematic diagram of the loading system used for measuring the compressive creep deformation.

attached to the top platen. The output signals including test temperature, sample displacement, strain and time were monitored and recorded by a computer. The frequency of data acquisition varied with the creep deformation rate. At the beginning of a test, the data were recorded every 5-10 seconds since the deformation rate was fast. When the deformation slowed down, the data were acquired every 2-5 minutes. The accuracy of strain measurement ($\Delta\varepsilon$) in this experiment was about $\pm 3 \times 10^{-5}$. The strain rates in both tension and compression tests were calculated by differentiation from the strain-time data which exhibited some electronic noise (see Figure 6.1). A computer program was used to fit a smooth curve through the strain-time data prior to the strain rate calculations.

All tests were performed at 1400± 2°C in air. In order to minimize the effect of oxidation on the creep behaviour, a new sample was used at each stress level. Due to limited material, only one sample was tested at each experimental condition. To avoid strain

recovery during cooling, the applied load was not removed until the sample reached room temperature.

3.4 Transmission Electron Microscopy

Throughout this work, TEM (transmission electron microscopy) was extensively used for microstructural characterization. For a successful TEM observation, the most important thing is to prepare high quality samples having a large thin area. Thin foils used for TEM observations were prepared by slicing the crept sample parallel to the stress axis into 500 μm thick pieces using a diamond saw, grinding to a thickness of about 120 μm using SiC paper, then cutting 3 mm discs with an ultrasonic drill and dimpling to about 20μm in the center. The final thinning was by argon ion milling at 4kV, 0.5 μA at an angle of 12°, on a nitrogen cooled stage until perforation. The foils were subsequently carbon-coated to prevent electrostatic charging under the electron beam. TEM observations were performed in a microscope (JEOL 2010 FEG-STEM) with a point-to-point resolution of 0.2 nm at 200kV.

3.5 Grain-Boundary Film Thickness Measurements

One of the objectives of this work was direct measurements of grain-boundary film thickness distribution before and after creep. Quantitative information on the thickness of these thin films were obtained by using transmission electron microscopy (TEM). In this work, both the Fresnel fringe imaging (FFI) technique and the lattice fringe imaging (LFI) technique were used to determine the grain-boundary film thickness.

3.5.1 LFI Technique

The measurement of intergranular film thickness by lattice imaging has been described elsewhere by Clarke (1979) and Cinibulk et al (1993). It is essential that the grain boundary is viewed edge-on while obtaining good diffraction conditions from both grains on either side of the grain boundary. At least one set of lattice planes are imaged in both grains and the discontinuity in the lattice fringes is identified as an intergranular film. The thickness of the film corresponds directly to the area of the discontinuity. The principle of this technique is shown schematically in Figure 3.5. To ensure accurate measurements, the images are taken close to the optimum value of defocus ($-C_s\lambda^2|g|^2$) (Krivanek et al 1979), where C_s is the spherical aberration coefficient of the objective lens, λ is the wavelength

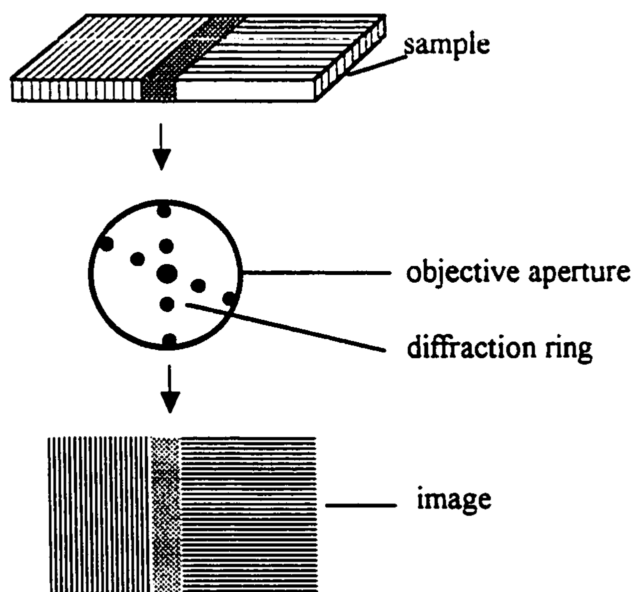

Figure 3.5 Principle of the LFI technique for measuring the grain-boundary amorphous film thickness.

of the electron beam, and $|g|$ is the magnitude of the reciprocal lattice vector. Using this technique, the film thickness can be measured to an accuracy of ± 0.1 nm.

3.5.2 FFI Technique

In the Fresnel fringe imaging mode, only the transmitted beam is allowed to pass through the objective aperture. By imaging out of focus, the presence of an intergranular film is revealed by the occurrence of fringes associated with the difference in mean inner potential of the amorphous film and the two crystalline grains. The thickness of the film, however, is not determined as straightforwardly as in the LFI mode. To obtain the thickness of the boundary amorphous film, the data of fringe spacing obtained from a series of defocus images are fitted to a curve. The thickness of the amorphous film corresponds to the spacing data at zero defocus. Since this method has been suggested only for detecting the presence of thin films rather than for accurately measuring their widths (Clarke 1979, Cinibulk et al 1993), the accuracy of this technique and its advantages over LFI in quantitative measurements of intergranular film thickness are described in detail in Chapter 4.

3.5.3 Statistical Analysis

The thickness distribution of grain-boundary amorphous films before and after creep was evaluated by a statistical analysis. In a given sample, twenty grain boundaries were selected randomly. A thickness data point was measured at three different locations at each grain boundary, thus giving 60 data points for a given sample. Using these data, the

distributions of the film-thickness values were plotted as histograms. For a Gaussian like distribution, the standard deviation σ was determined using the following equation:

$$\sigma = \sqrt{\frac{1}{n-1}\sum_{i=1}^{n}(X_i - X)^2} \tag{3.1}$$

where X_i is the ith thickness measurement, X is the mean thickness value, and n is the number of the film thickness measurements. For a bimodal distribution of film widths, the two peaks were deconvoluted before calculating the mean value of each peak.

3.6 Chemistry Analysis

The stability and crystallization of the intergranular amorphous phase in structural ceramics such as sintered Si_3N_4 strongly influence mechanical properties, particularly high temperature creep and damage processes. In order to interpret the mechanical test data, it is very important to understand the microstructural evolution. The behaviour of this amorphous phase is determined by its composition. While the amorphous phase at two-grain boundaries is thermodynamically stable (Kessler et al 1992), the amorphous phase at multigrain junctions can be crystallized into a variety of phases after heat treatment. Since the intergranular amorphous phase is only of the order of 10% by volume and the thickness of the amorphous films at two-grain boundaries is only 0.5-2 nm, careful analytical electron microscopy (AEM) is necessary to characterize the grain boundary chemistry and devitrification products. Energy dispersive x-ray spectroscopy (EDS) was used in this investigation.

The basic principle of EDS is that high voltage electrons excite the atom of interest when they transverse a thin foil specimen, thus ejecting an electron from an inner shell (inner shell ionization). The atom can return to the ground state by an electron jumping from an outer shell to the vacant inner shell position and at the same time emitting an x-ray of a characteristic energy. A spectrum of x-ray counts (or intensity) versus x-ray energy is thus collected. The emitted characteristic x-ray energy is unique to the ionized atom, giving chemical information of all elements in the area of interest. In general, EDS can only detect elements with atomic number (Z) ≥ 10. Lighter elements can be detected with an ultra-thin window or windowless detectors as they do not absorb all the low energy x-rays produced by the light elements. Due to x-ray absorption, fluorescence yield, peak overlap and sample damage (Chadwick 1990), an element is detectable only when its concentration is higher than a certain value. The detectability of elements depends on the system of interest. More details of the x-ray production process and the use of EDS for chemical analysis can be found in standard texts, e.g., Williams (1987).

Chemical analysis of the nano-scale grain boundary films requires a fine probe. The probe size is governed by the characteristics of the electron source. Three types of electron sources are commonly available, namely tungsten hairpin filaments, lanthanum hexaboride (LaB_6) filaments and field emission guns (FEGs). The smallest probe size is approximately 10 nm for a LaB_6 filament, and 20 to 30 nm for a tungsten filament. Apparently, they are not appropriate for grain boundary chemistry analysis. From the analytical standpoint alone, an FEG is the ideal electron source giving a very small probe size (it can be < 1 nm in diameter). In this work, EDS analysis was carried out in a JOEL 2010 FEG high-

resolution electron microscope (HREM) operating at 200kV, equipped with a scanning and EDAX attachment. The probe size of better than 1 nm of this microscope enabled high-resolution chemical analysis of intergranular regions.

Quantitative EDS analysis was used to identify the secondary crystalline phase grains in the Y_2O_3 doped material. The relationship between the intensities of x-ray peaks (I_A and I_B) and relative concentrations (C_A and C_B) can be expressed by :

$$\frac{C_A}{C_B} = K_{AB}\frac{I_A}{I_B} \qquad (3.2)$$

where K_{AB} is a proportionality constant (K factor) which can be determined experimentally. This equation assumes that the sample is so thin that absorption and fluorescence of x-rays are negligible as they pass through the sample.

X-ray mapping was also used to analyze the chemistry distribution throughout the microstructure. The x-ray image obtained by using an energy window of interest from a EDS spectrum shows contrast depending on the x-ray emission characteristics of the specimen. Assuming the specimen is of constant thickness and satisfies the thin foil criterion, the local image intensity would depend linearly on the local concentration of the element distributed throughout the area being scanned. In order to obtain good quality images, Poisson statistics require about 2×10^5 to 5×10^5 x-ray photons per image (Goldstein et al 1986). In this work, it generally took about 30 minutes of scanning to produce an image of good contrast as the TEM specimen is very thin.

Chapter 4

DETERMINATION OF GRAIN-BOUNDARY FILM THICKNESS BY THE FRESNEL FRINGE IMAGING TECHNIQUE

4.1 Introduction

A number of TEM techniques have been used to detect grain-boundary amorphous films. The width of these films can be determined by high-resolution lattice fringe imaging (LFI) as an area of discontinuity in the lattice fringes of the grains (Clarke et al 1977, Clarke 1979, Cinibulk et al 1993); by diffuse dark-field imaging (DDF) as an area of bright contrast relative to the bounding grains (Cinibulk et al 1993, Krivanek et al 1979, Ness et al 1986); or by defocus Fresnel fringe imaging (FFI), based on the extrapolation of defocus fringe-spacing data (Clarke 1979, Cinibulk et al 1993, Ness et al 1986). Although the DDF technique enables direct measurements of grain-boundary film thickness to be made, it suffers from some disadvantages which make the accurate determination of the film width difficult. For example, a poorly defined interface and a low intensity are usually associated with this method (Clarke 1979, Cinibulk et al 1993). Thickness determination by LFI can be limited by uncertainty in the degree of lattice fringe overlap into the amorphous region as a function of boundary tilt and objective defocus (Krivanek et al 1979). The FFI technique has been applied to the detection of the boundary film for some time. However, it has been suggested (Clarke 1979, Cinibulk et al 1993) that this technique is best suited for detecting the presence of thin films rather than for accurately measuring their widths. Thus the question arises as to which method can best be used to quantitatively measure the widths of intergranular films. The

advantages and disadvantages of these techniques in terms of experimental ease and accuracy of thickness determination have been discussed previously (Clarke 1979, Cinibulk et al 1993). Cinibulk et al (1993) concluded that LFI is the most accurate method for quantitative measurements of film thickness (± 0.1 nm) whereas DDF is the most inaccurate technique. In this Chapter, the FFI technique is used to measure intergranular film widths, and the results are compared with those obtained from LFI. Thus one aim of this work is to assess the accuracy to which the boundary film thickness can be determined by the FFI technique. The advantages of FFI over LFI in quantitative measurements of intergranular film thickness are also discussed. The material used is the undoped silicon nitride. To compare directly the two techniques for the measurement of intergranular film thickness, grain boundaries must be chosen to which both methods could be applied. Obviously, such a boundary must be parallel to the electron beam and also satisfy the necessary conditions for lattice fringe imaging. Since the Fresnel fringes produced on defocusing are only symmetric on both sides of the boundary when the interface is exactly parallel to the electron beam (Clarke 1979, Jepps et al 1982), the FFI method is used to align a grain boundary edge-on.

4.2 Results and Discussion

4.2.1 Determination of Grain-Boundary Film Thickness

The use of the Fresnel fringe imaging technique for detecting thin intergranular films was first reported by Clarke (1979). The formation of the Fresnel fringes along a grain

boundary is caused by the difference in the mean inner potential between the grains (V_g) and the intergranular phase (V_i), as shown schematically in Figure 4.1.

The behaviour of Fresnel fringes at a straight edge in a thin foil has been analyzed in detail (Fukushima et al 1974, Reimer 1989). The position of the first fringe from the edge has been found to be proportional to $\Delta f^{1/2}$, where Δf is the defocus distance of the objective lens (Reimer 1989). Applying this analysis to an intergranular amorphous film which has a smaller inner potential than that in the adjacent grains (as in Figure 4.1), the relationship between fringe spacing W and the boundary film thickness W_0 is obtained

$$W = W_0 + c\Delta f^{1/2} \tag{4.1}$$

where c is a microscope dependent constant approximately equal to $(3\lambda)^{1/2}$ (Reimer 1989), and λ is the wavelength of the electron beam. For the TEM used in this study c = 0.086 $nm^{1/2}$ with λ = 0.0025 nm.

To determine an intergranular film thickness, the images of the boundary film in the through-focus series are recorded. Figure 4.2 shows an intergranular film at four different defocus values. When the mean inner potential of the intergranular amorphous film is lower than that of the grains, as in Si_3N_4 ceramics, the underfocused images contain a bright line at the film and alternating dark and bright Fresnel fringes on either side (a and b). The overfocused images display the reverse contrast (c and d). The spacing of the fringes decreases with decreasing defocus, consistent with the expectation of equation (4.1). To obtain the thickness of the boundary amorphous film, the data of fringe spacing

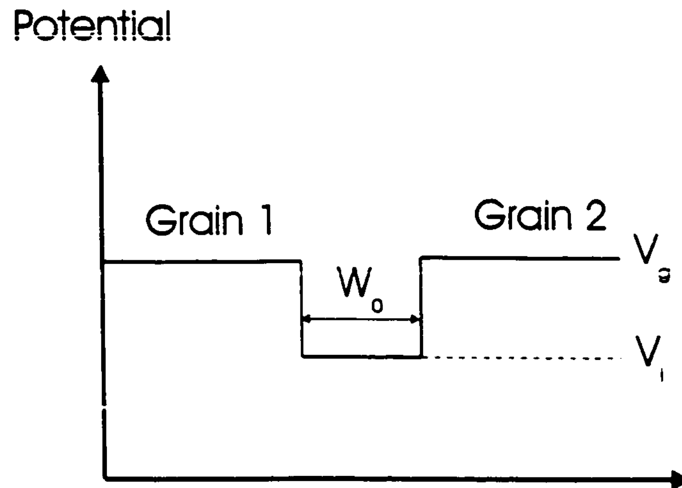

(a)

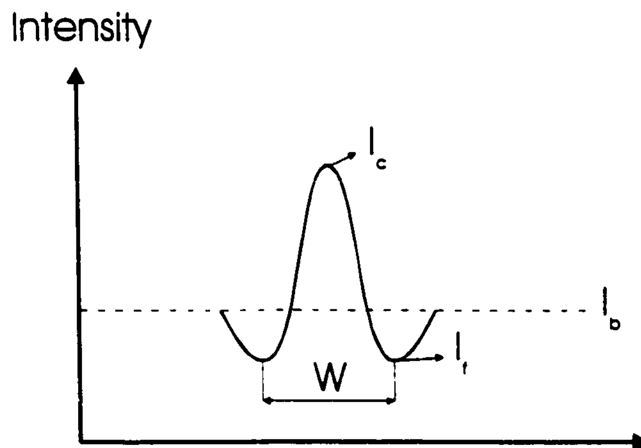

(b)

Figure 4.1 Schematic diagram representing the boundary potential model (a), and the corresponding schematic profile of intensity for underfocus (b). I_b is the background intensity; I_c is the intensity at the center of the boundary film; I_f is the intensity of the first set of fringes.

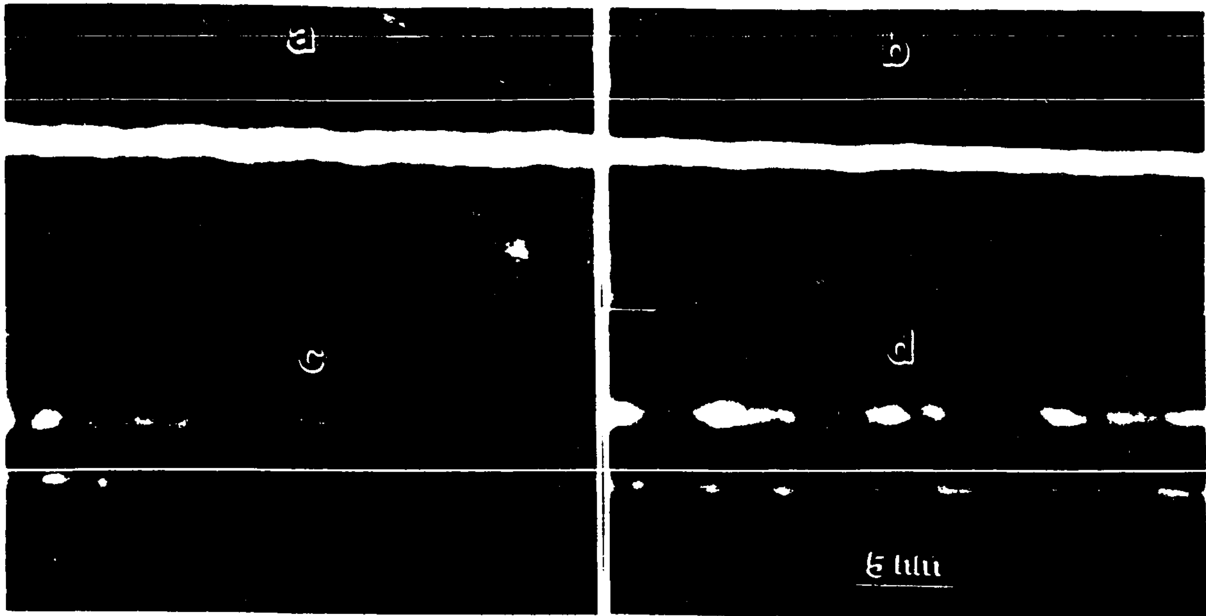

Figure 4.2 Through focal series of images of a grain boundary in silicon nitride; (a) underfocus of 1400 nm, (b) underfocus of 700 nm, (c) overfocus of 700 nm, and (d) overfocus of 1400 nm. The fringe spacing decreases with decreasing defocus.

obtained from a series of defocus images are fitted to a function defined by equation (4.1). The thickness of the amorphous film corresponds to the spacing found at zero defocus.

Figure 4.3 contains curves obtained by fitting the spacing data of the Fresnel fringes for a number of defocus values. The curve obtained from the underfocus series results in a boundary film thickness of 0.91 nm. The curve from the overfocus series gives a value of 1.0 nm, slightly greater than that determined from the underfocus series. This result is consistent with that obtained by Cinibulk et al (1993) in determining the grain-boundary film thickness by FFI. Straight lines are obtained by fitting the data of W vs $\Delta f^{1/2}$, as shown in Figure 4.3b. This confirms that the fringe spacing increases with $\Delta f^{1/2}$.

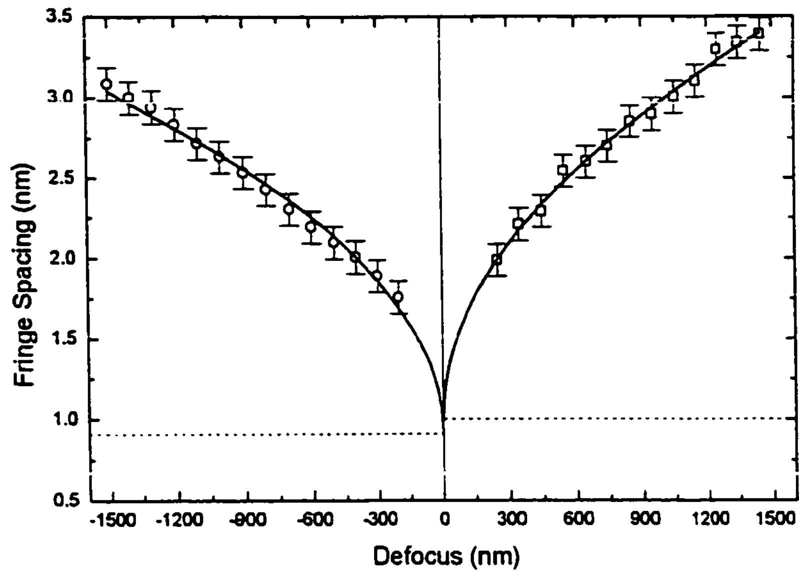

(a)

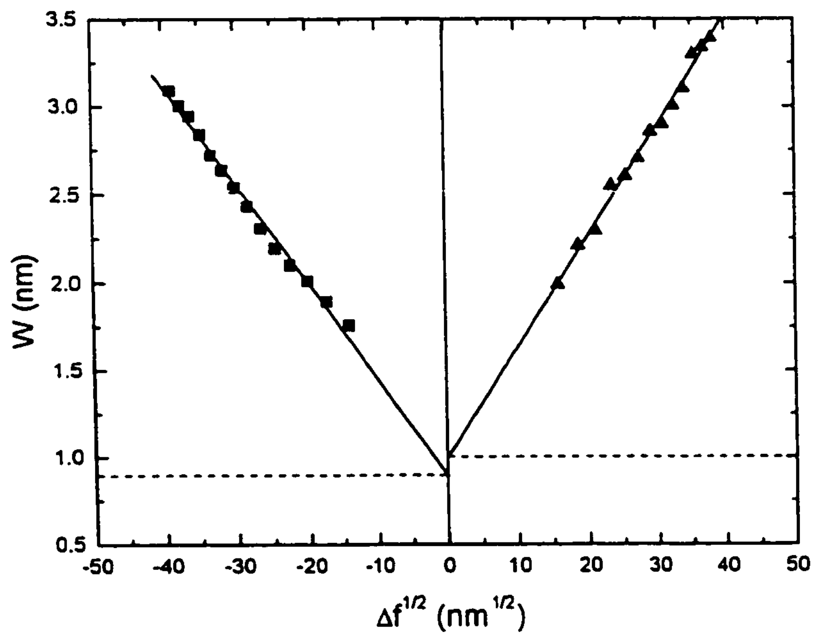

(b)

Figure 4.3 Measured fringe spacing data as a function of defocus for the boundary shown in Figure 4.2, (a) the fitting function $W = W_0 + c\Delta f^{1/2}$ is used to obtain the boundary film thickness; (b) linear fitting is used, confirming that the fringe spacing (W) is a function of $\Delta f^{1/2}$.

4.2.2 Accuracy and Validity of Measurement

To assess the accuracy of the FFI method, the same grain boundary was also characterized by LFI. To do this, an objective aperture was chosen that allowed a maximum number of diffracted beams to form the image while maintaining adequate image contrast. The high-resolution image of the grain boundary is shown in Figure 4.4. The thickness of the boundary film is found to be 1.05 nm, in good agreement with the results of FFI.

A key factor in applying the defocus Fresnel fringe technique involves how one fits the experimental data. Since the value of film thickness is obtained by extrapolation of a curve to $\Delta f = 0$, it is apparent that the data from the low-defocus images is more important for film thickness determination. In general, however, fringes become visible only when $\Delta f > 200$ nm. Therefore, higher defocus values have to be used to obtain sufficient data for extrapolation. This approach has also been suggested by Cinibulk et al (1993). In this case, selection of a fitting function is critical since different functions could result in significant differences in the value of film thickness. When the number of data are limited, it is difficult to identify what relationship the experimental data actually obeys. In this study, the relationship defined by equation (4.1) has been observed between the fringe spacing and the defocus.

Using the relation $W = W_0 + c\Delta f^{1/2}$ as a fitting function, the value of c can be obtained from the experimental data. For the boundary shown in Figure 4.2, c is 0.055 $nm^{1/2}$ for the underfocus series and 0.063 $nm^{1/2}$ for the overfocus series. These data are close to the

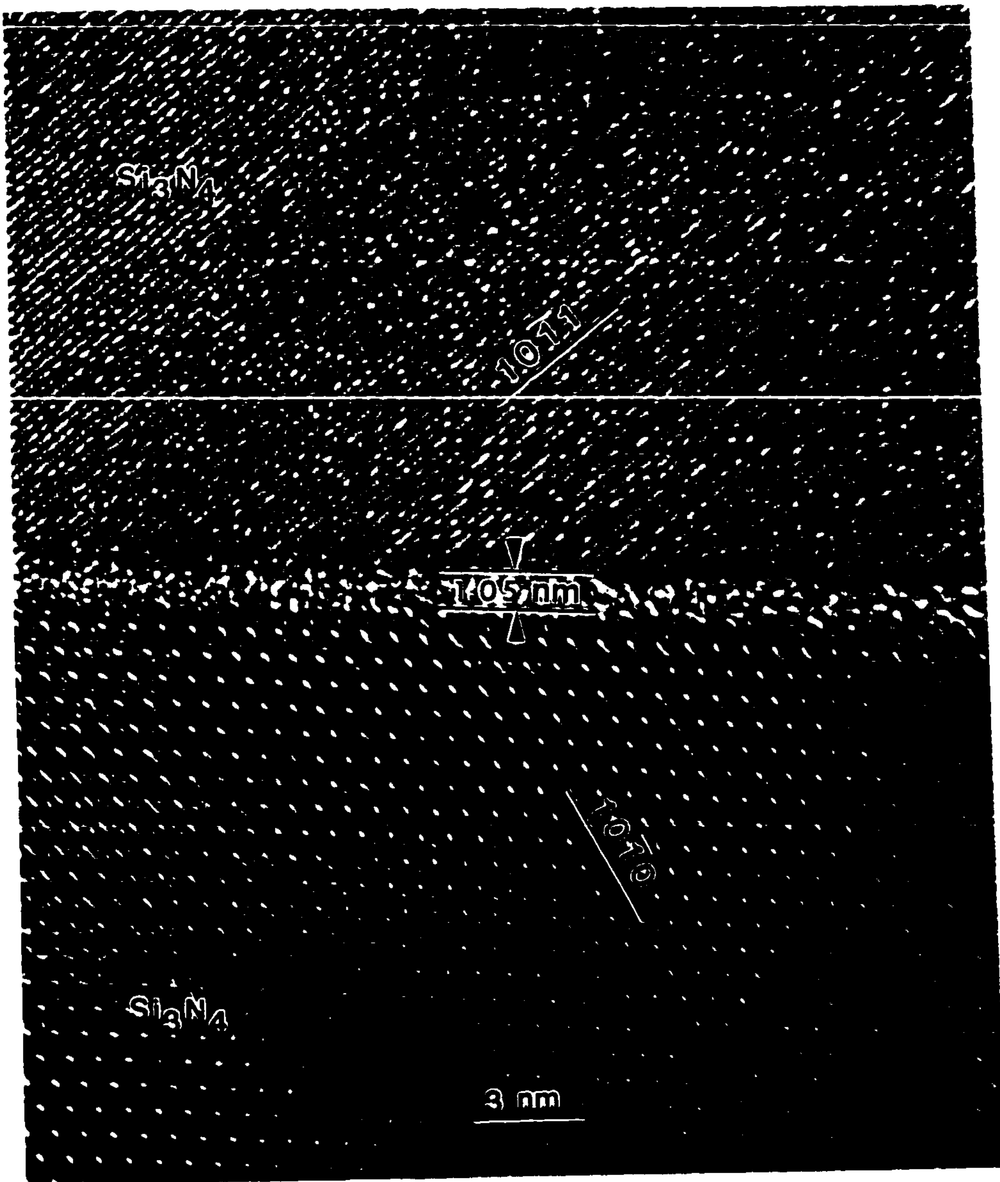

Figure 4.4 High-resolution lattice fringe image of the grain boundary shown in Figure 4.2.

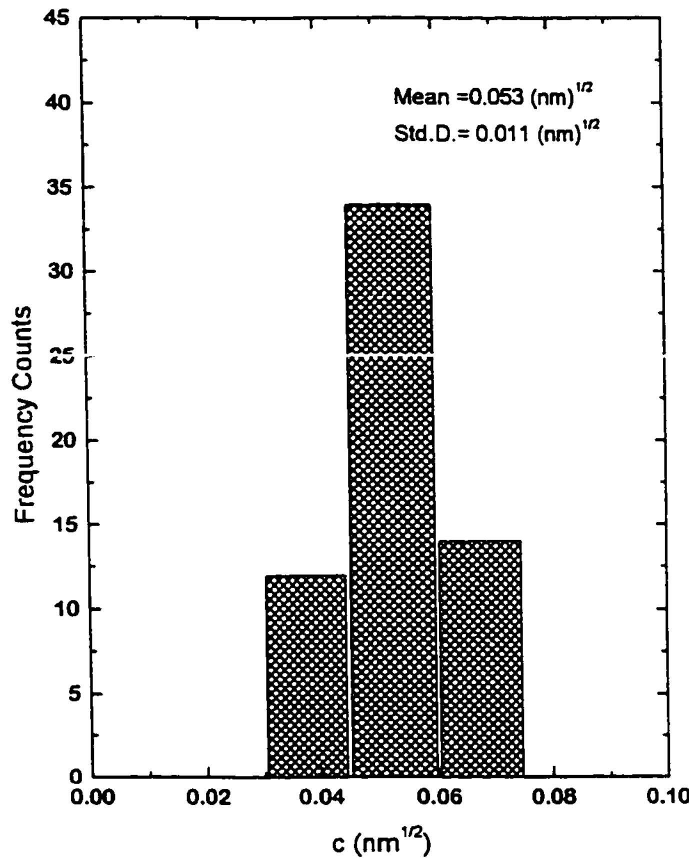

Figure 4.5 Histogram of the distribution of parameter c in the fitting function $W = W_0 + c\Delta f^{1/2}$ obtained from different grain boundaries.

value of c=0.086 $nm^{1/2}$ expected from equation (4.1) with λ=0.0025nm. To examine whether the value of c is constant for any grain boundary, twenty grain boundaries were selected randomly and the film thickness was measured by FFI at three different locations for each grain boundary. The values of c display a Gaussian distribution with a mean value of 0.053 $nm^{1/2}$ and a standard deviation of 0.011 $nm^{1/2}$, as shown in Figure 4.5. This

result suggests that the fitting function defined by equation (4.1) really does reflect the relation between the fringe spacing and defocus value. Jepps et al (1982) also found this relationship in their investigation of intergranular film widths in SiC materials.

Provided that the fitting function is correct, the main source of error in measuring the film thickness by the FFI method comes from the experimental uncertainty in defining the position of the first fringe maxima due to poor contrast at low defocus. The determination of the defocus value could also introduce an error to the value of film thickness. However, by carefully locating the position of the fringe maxima and by accurately calibrating the defocus, the film thickness can be determined to an accuracy of $\pm$ 0.15 nm. The accuracy has also been demonstrated by statistical analysis of intergranular film widths in two as-sintered silicon nitride ceramics (Jin 1995). In that study it was found that the widths of grain-boundary films display a Gaussian distribution with standard deviations $\leq$ 0.15nm. As indicated by Kleebe et al (1993a), two factors may contribute to the standard deviation. One is a real variation in film thickness at different grain boundaries. The other is the measurement error introduced by the measurement method. Clarke (1987) proposed that in a given Si_3N_4 ceramic, a stable equilibrium intergranular film thickness exists. TEM studies (Kleebe et al 1994b) of different Si_3N_4 materials supported his theory and have generally found that the film thickness has a characteristic value for a given chemical composition and is independent of grain boundary orientation. Based on this, it is reasonable to suggest that the value of the standard deviation found in that study (0.15nm) primarily reflects the accuracy of measurement of this technique.

4.2.3 Advantages of FFI and Limitations of LFI

LFI is capable of providing detailed information on a grain boundary at the atomic level. Moreover, an accuracy of ± 0.1 nm can be achieved in determining the boundary film thickness (Cinibulk et al 1993, Kleebe et al 1994b). However, the measurement of the intergranular film width by this method requires that strict geometrical conditions be met. The grain boundary must be viewed edge-on while maintaining good diffracting conditions for both adjacent grains. These requirements limit its application to a small number of grain boundaries in a typical TEM sample. For most grain boundaries, only one of the conditions can be satisfied. When a grain boundary is oriented edge-on by tilting to obtain symmetric Fresnel fringes, one or both of the adjacent grains are usually not at good diffracting conditions for LFI.

Interpretation of high-resolution images also complicates its application. Both a defocus change and specimen tilting cause the lattice fringes in the crystalline grains to extend into the amorphous phase and lead to a significant error in film thickness determination. The influence of boundary tilt on the lattice imaging method has been discussed by Lou et al (1978). As the lattice-fringe images are recorded in a defocus condition, relative shifts could occur between the two sets of fringes originating from the adjacent grains. According to Krivanek et al (1979), the displacement of the Bragg beam **r** is expressed as

$$\mathbf{r} = C_s \lambda^3 |g|^3 + \Delta f \lambda |g| \tag{4.2}$$

where C_s is the spherical aberration coefficient of the objective lens, λ is the wavelength of the electron beam, $|g|$ is the magnitude of the reciprocal lattice vector and Δf is the defocus. From this equation, it is obvious that only one defocus value ($-C_s\lambda^2 |g|^2$) places the lattice fringe terminations exactly at the crystal edge, i.e., no shift of the fringes occurs. At the Scherzer defocus (-60 nm) for the TEM used in this study (C_s=1.5 nm, λ=0.0025 nm), the lattice fringes of the β-Si_3N_4 $\{10\bar{1}0\}$ reflection will shift 0.12 nm from the edge of the crystal. For higher defocus values, the shift becomes more significant. A good example of the effect of a defocus change on the lattice-fringe images can be found in an article by Krivanek et al (1979). The amorphous phase at two-grain boundaries could disappear when the defocus does not coincide with the optimum value. Thus determination of the widths of thin intergranular films by lattice imaging may lead to false conclusions if the defocus value is not chosen carefully. Another factor to be taken into consideration in lattice imaging is the effect of the foil thickness. The sensitivity of lattice-fringe visibility to the foil thickness has been discussed by Clarke (1979) for silicon nitride. To measure the intergranular film thickness accurately by LFI, both adjacent grains must be of a thickness at which the lattice fringes display a high contrast. In general only grain boundaries in the very thinnest regions of a specimen satisfy this requirement.

From these considerations, it is clear that detecting very thin films (about 1 nm) by this method could be problematic. In order to ensure that the high-resolution images are a reliable reflection of the projection of both the adjacent grains and the intergranular film, the interface must be carefully oriented parallel to the electron beam, and the image must be taken from the thinnest regions of a specimen and recorded at the optimum value of

defocus. This was the procedures followed to obtain the LFI image shown in Figure 4.4. Due to these limitations, the LFI technique cannot be applied to an arbitrary grain boundary.

The major advantage of the FFI technique is that it can be applied to any grain boundary of interest. The symmetry of Fresnel fringes indicates clearly whether the boundary is parallel to the electron beam. This advantage enables a statistical analysis of a large number of grain-boundary films to be undertaken, e.g., to study the redistribution of a grain-boundary glass phase during high temperature creep of ceramic materials. For glass-containing ceramics such as silicon nitride, viscous flow is an important process contributing to creep deformation of the material. Although several models have been developed to describe this process (Drucker 1964, Dryden et al 1989, Chadwick et al 1992), the analysis is mainly based on indirect evidence such as the creep response or strain recovery phenomenon. By using the FFI method to measure the grain-boundary film widths before and after creep, direct evidence of the microstructural evolution due to viscous flow has been obtained (Jin 1995). The film thickness change on the boundaries perpendicular to the stress axis can be obtained from the difference in standard deviations before and after creep. This value enables a direct comparison between the creep response predicted by viscous flow models and the experimental observations. To undertake such a statistical analysis many grain boundaries have to be selected in a TEM specimen, a difficult procedure for LFI but straightforward for FFI studies.

4.3 SUMMARY

The defocus Fresnel fringe technique has been addressed as a method for determining the widths of intergranular films in materials such as silicon nitride. It has been shown that this method is capable of relatively precise determination of the boundary film thickness (±0.15 nm), and is easier to operate experimentally than the high-resolution lattice imaging technique. Therefore, it is suggested that the FFI method is a useful technique for quantitatively determining intergranular film thickness. To ensure a reliable value of film thickness the fitting function for the experimental data is very critical, in that the thickness of the boundary film is determined by the extrapolation to zero defocus. The determination of intergranular film thickness by the high-resolution lattice imaging technique is confined to some specific grain boundaries due to the set of very strict geometrical and electron-optical conditions that must be satisfied. If the defocus value is not appropriate the lattice imaging technique could lead to a large error in the value of the boundary film thickness. In contrast, the defocus Fresnel imaging technique can be applied to any grain boundary of interest. This method exhibits significant advantages when a statistical analysis of the intergranular film widths is required.

Chapter 5

MICROSTRUCTURE OF SILICON NITRIDE

5.1 Introduction

The main interest in silicon nitride ceramics is in their application as high-temperature structural materials. These materials, which are fabricated by a liquid phase sintering process, contain a residual intergranular phase inherited from the sintering liquid (Lange 1980). This liquid forms above the relevant eutectic temperature through reaction between the sintering additives, the inherent surface SiO_2 on the starting α-Si_3N_4, and the Si_3N_4 itself (Lange 1980, Lewis et al 1983). The α-Si_3N_4 in the starting powder compact is dissolved in the liquid, and β-Si_3N_4 is precipitated either homogeneously in the supersaturated liquid or on pre-existing β-Si_3N_4 particles. This process results in a microstructure consisting of β-Si_3N_4 grains and a small percentage of an intergranular phase, consisting usually of silicon, oxygen, nitrogen and cations of the sintering additives. The β-Si_3N_4 grains will adopt a shape close to that of a hexagonal prism if they are allowed to grow without steric hindrance in a suitable liquid environment (Lewis et al 1977). This intergranular phase, which is present in both multigrain junctions and as thin films between essentially all grains, is thought to limit the high temperature properties of the materials (Tsuge et al 1975, Clarke et al 1982).

The intergranular phase is usually amorphous after sintering, but secondary crystalline phases may partition from the liquid phase sintering medium. While the thin films at two-grain boundaries are always amorphous, larger volumes of residual phase at multigrain

junctions may, in some systems, be crystallized during post-sintering heat treatment (Tsuge et al 1975, Falk 1987). The volume fraction, composition, distribution and crystalline state of the intergranular phase are determined by the type and amount of additives (Kleebe et al 1992). In case of absence of sintering additives (except SiO_2), the microstructure of silicon nitride consists of β-Si_3N_4 grains surrounded by a continuous grain boundary phase which is assumed to be pure silica. With the addition of sintering aids such as Ca (Tanaka et al. 1994b) or Ba (Jin 1995), the general microstructure may remain the same in that only Si_3N_4 grains are present with the grain boundary phase, but the properties of the grain boundary phase may change compared with those of undoped silicon nitride. The addition of sintering aids such as Y_2O_3 (Clarke et al 1978, Vetrano et al 1993), however, may introduce secondary crystalline phases, thus changing both the general microstructure and characteristics of grain boundary films.

Thin amorphous films are observed between all but low angle boundaries or specially-orientated grain boundaries in sintered silicon nitride and have a characteristic film thickness in the range of 0.5 - 2 nm (Schmid et al 1984). Since almost all grain boundaries contain an amorphous intergranular phase, the thickness of these films becomes important with respect to material performance, especially at high temperatures. The formation of an amorphous film with a characteristic thickness in some ceramics has been explained by Clarke (1987). He considered attractive and repulsive forces acting on the adjacent grains across the intergranular film and was able to derive a formula which allows, in theory, the calculation of the grain-boundary film thickness. However, some of the parameters involved in the derived equation are still unknown (e.g., the dielectric constants of the

intergranular film and/or the secondary crystalline phases). Hence, a calculation of the equilibrium grain-boundary film thickness in most silicon nitride ceramics is not yet possible. Therefore, high-resolution electron microscopy (HREM) has been used to image grain boundary films in Si_3N_4 materials to determine the corresponding film width (Kleebe 1991, Clarke 1989).

The present chapter describes an investigation of the microstructure of silicon nitride with and without the sintering aids. The sintering aids include 800 wt ppm Ba and 4 wt. % Y_2O_3. The typical microstructural features of the Ba doped and Y_2O_3 doped silicon nitride have been characterized and compared with the undoped material. This includes the characterization of the crystalline secondary phases as well as the structure and chemistry of the thin amorphous intergranular films. As the main creep mechanisms in Si_3N_4-based materials are grain boundary sliding accommodated by cavitation (Wiederhorn et al 1993), dissolution-reprecipitation (Raj 1982) and viscous flow (Dryden et al 1989), the thickness and viscosity of the amorphous intergranular film are believed to play an important role in the high temperature properties of the materials. The lattice fringe imaging technique was employed as the main method to measure the interfacial amorphous film widths. To ensure accurate measurements, the boundaries were tilted to edge-on, and images were taken close to Gaussian focus. This technique has been described in detail in Chapter 4. The probe size of about 1 nm of the microscope used (JEOL 2010 FEG) enabled high-spatial resolution chemical analysis of the intergranular regions by energy dispersive X-ray spectroscopy (EDS). Phase identification in the TEM was carried out by nano-beam electron diffraction combined with fine probe EDS analysis due to the small size of most

of the secondary phase grains. HREM in combination with AEM provides important information for a deeper understanding of the correlation between grain boundary film characteristics and resulting creep behaviour of liquid phase sintered silicon nitride ceramics.

5.2 Results

5.2.1 General Microstructure

Both TEM and SEM were used to characterize the microstructure of the experimental materials. SEM micrographs (Figure 3.1) were used to provide information about grain size and aspect ratio. More detailed information on the microstructure was obtained by TEM. The general microstructure of all materials investigated consisted of equiaxed and elongated β-Si_3N_4 grains, and multigrain junctions filled with the remnant liquid formed during sintering either in the amorphous or crystalline state. The multigrain junctions were randomly distributed throughout the samples. All Si_3N_4 grains and Si_3N_4/secondary crystalline phase boundaries were separated by a thin amorphous intergranular film with the only exception being low energy boundaries where no amorphous film was found.

(1) Undoped and Ba doped Si_3N_4

The undoped and Ba doped materials displayed a similar microstructure, as shown in Figure 5.1. The hexagonal β-Si_3N_4 grains were about 0.2 to 0.3 μm in diameter across the basal plane, with some elongated grains exhibiting aspect ratios of up to 10. Based on TEM observations, no other crystalline phases were observed. Virtually all of the

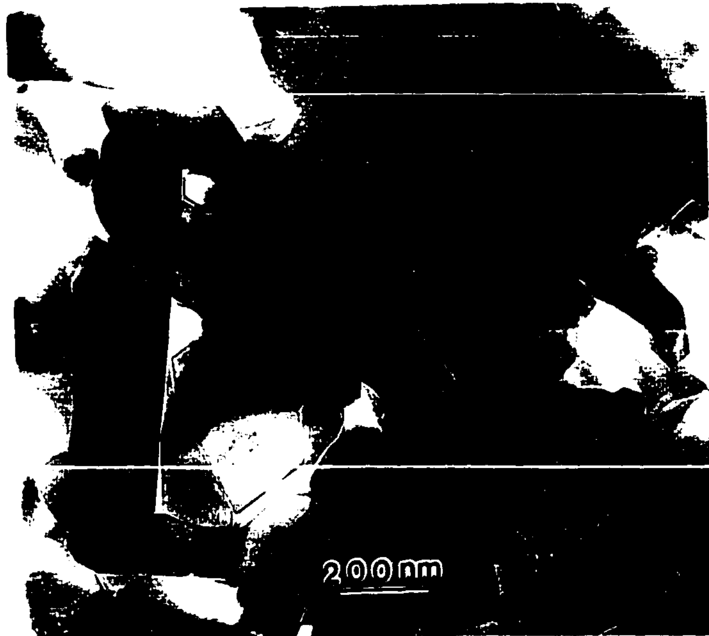

(a)

(b)

Figure 5.1 TEM micrographs of the undoped (a) and Ba doped material (b), showing equiaxed and elongated β-Si_3N_4 grains.

multigrain junctions were amorphous. The amorphous multigrain junctions were connected by thin amorphous grain-boundary films covering the Si_3N_4 particles. Figure 5.2 shows an intergranular phase both in a triple junction and at two-grain boundaries. No change in contrast on tilting demonstrates its amorphous structure. The addition of Ba has little influence on the general microstructure of silicon nitride. This is consistent with our previous work on the microstructure of Ba doped material, which was HIPed at 1925°C for 0.5 h (Jin 1995) whereas in this work, the Ba doped material was HIPed at 1925°C for 1h.

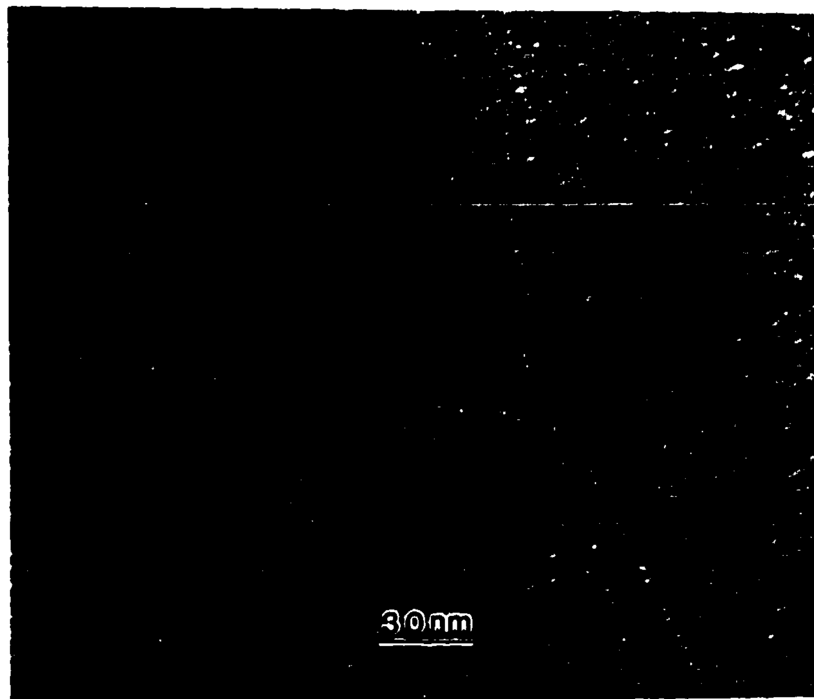

Figure 5.2 TEM micrograph of an amorphous intergranular phase in a triple junction and at two-grain boundaries.

(2) Y_2O_3 doped Si_3N_4

The microstructure of the Y_2O_3 doped material was substantially different compared to the undoped and Ba doped materials. After heat treatment at 1430°C for 690 h, complete crystallization of the intergranular phase occurred at multigrain junctions. It is important to note that the term "complete crystallization" is used here with the understanding that the aforementioned thin amorphous intergranular films still exist along grain and phase boundaries. The general microstructure of this material after complete multigrain crystallization is shown in Figure 5.3a. Both silicon nitride and secondary phases varied in grain size and morphology. The secondary phases are much darker than silicon nitride grains in almost all cases in bright-field images, suggesting the presence of yttrium, which has a much higher scattering factor (Clarke 1978). An example of a completely crystallized multigrain junction can be seen in Figure 5.4.

Three secondary crystalline phases, α-$Y_2Si_2O_7$ and δ-$Y_2Si_2O_7$ and $Y_5(SiO_4)_3N$ (Y,N-apatite), were identified by selected-area diffraction (SAD) and EDS in the TEM together with powder X-ray diffractometry (XRD). Results of XRD analysis are given in Figure 5.5. This is essentially consistent with the previous investigations of this material (Menon et al 1994, Yeckley et al 1989). Quantitative EDS analyses were carried out and the results matched very well with the $Y_2Si_2O_7$ phase. The EDS spectra corresponding to these two phases are shown in Figures 5.3b and 5.3c. Although the presence of nitrogen in the apatite phase made quantitative analysis difficult due to a detection limit of nitrogen and the overlap with carbon (carbon coating), silicon and yttrium were found in the ratio

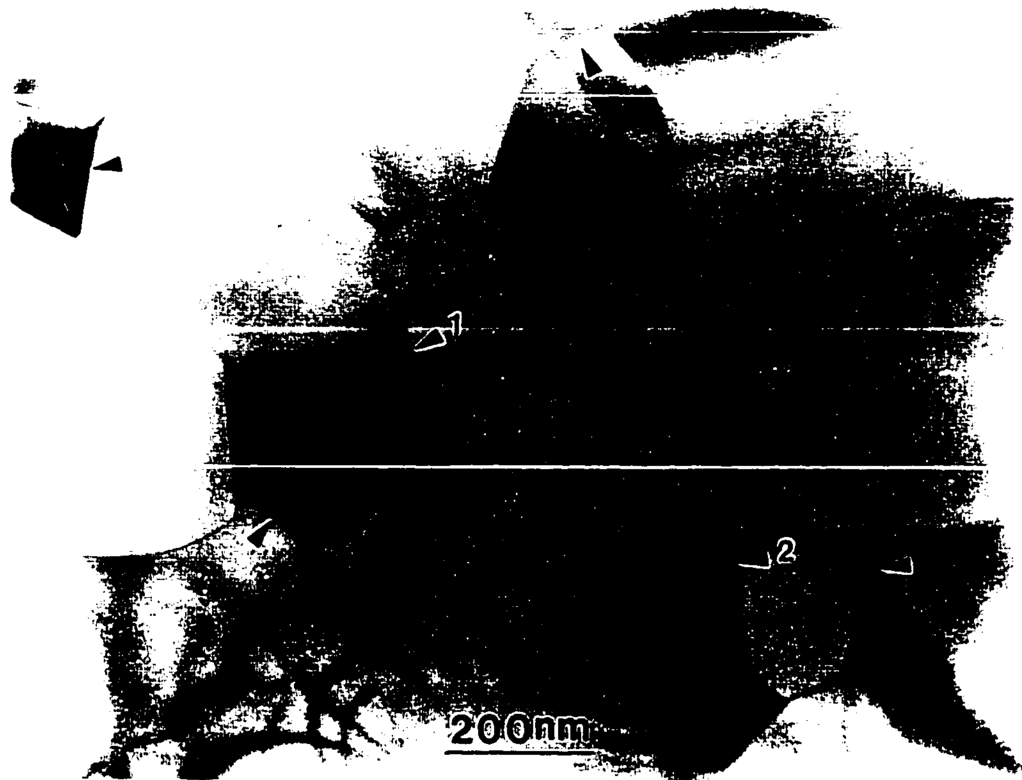

(a)

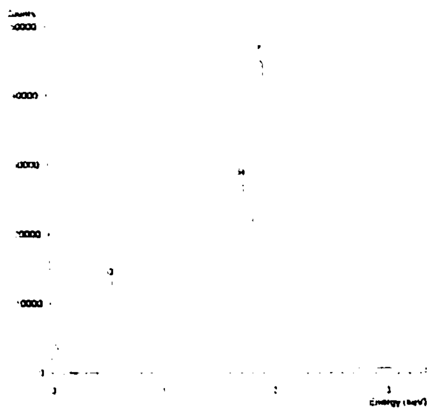

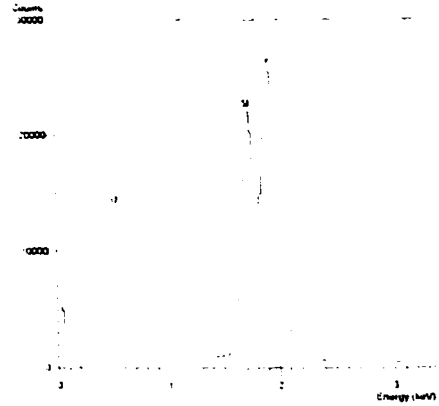

(b) (c)

Figure 5.3 (a) TEM micrograph of the Y_2O_3 doped material after heat treatment at 1430°C for 690h, showing secondary crystalline phases formed at multigrain junctions (indicated by arrows); (b) a EDX spectrum corresponding to $Y_5(SiO_4)_3N$ (indicated by a 1 in a); (c) a EDX spectrum corresponding to $Y_2Si_2O_7$ (indicated by a 2 in a).

(a)

(b)

Figure 5.4 Micrographs of a multigrain junction in the Y_2O_3 doped heat-treated sample showing complete crystallinity in (a) bright-field and (b) dark-field.

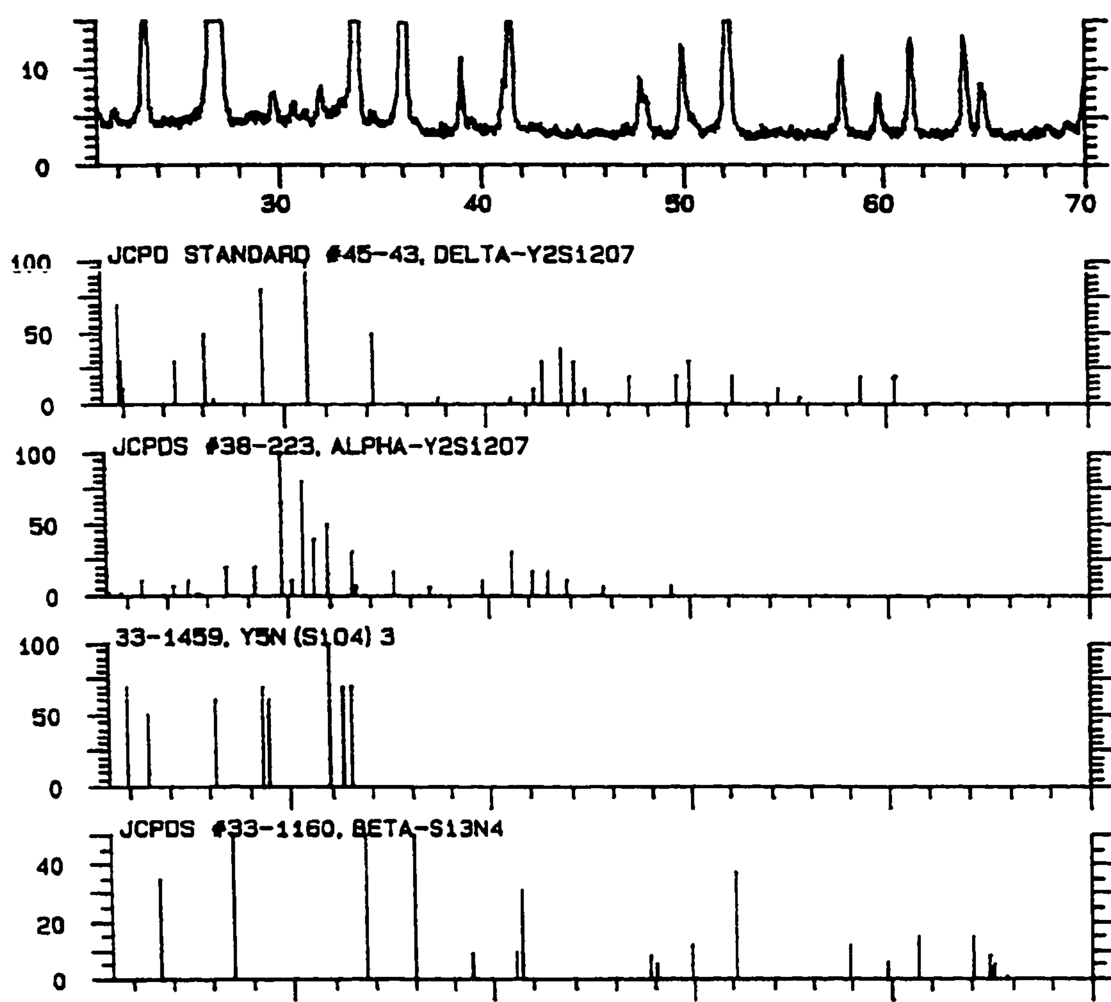

Figure 5.5 Results of XRD analysis of the Y_2O_3 doped material, showing the presence of β-Si_3N_4, α- and δ-$Y_2Si_2O_7$, and N-apatite phase in the microstructure.

of 3:5 by using the Cliff and Lorimer method (Cliff and Lorimer 1975). With the chemical information from EDS, the available crystallographic data of the three secondary phases from the JCPDS files enabled an unambiguous phase identification by indexing the electron diffraction pattern. An overview of the distribution of the secondary phases in the microstructure is revealed in the SEM (Figure 5.6). Images obtained by secondary electrons showed bright contrast from the secondary phases. These were used for quantitative determination of the volume fraction of the secondary phases, which is about 10 vol. % in the sample.

The secondary phases were usually seen at multi-grain junctions (Figure 5.3) but occasionally polyphase pockets containing both secondary phase grains and silicon nitride grains could be observed. Figure 5.7 is an annular dark-field image of such a region, viewed in the STEM. The yttrium-containing secondary phases exhibit a bright contrast due to the so-called 'Z contrast'. In this case, the secondary phase (or phases) completely (or partially) envelops the Si_3N_4 grains. This implies that a solution-reprecipitation process occurred during densification. Si_3N_4 grains with rounded shapes would be dissolving in the liquid phase while grains with faceted shapes would be growing (Falk 1996). Electron diffraction from grains with faceted sections showed that these grains had the β-Si_3N_4 polytype. The faceted shape is, hence, reflecting the hexagonal crystal structure of the β-Si_3N_4. The proposed solution-reprecipitation process would give a certain contribution to the densification of the Si_3N_4 ceramics. But this process did not result in any detectable incorporation of Y or Ba into the Si_3N_4 grains. It should be noted that although two morphologies (i.e., at multigrain junctions or enveloping Si_3N_4 grains) exist for the

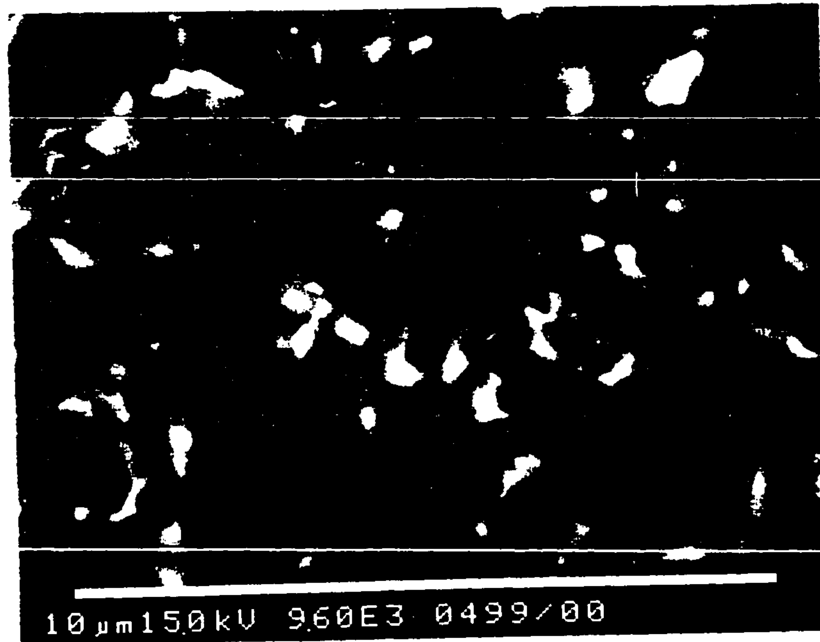

Figure 5.6 SEM microstructure of the Y_2O_3 doped sample (polished without etching) showing the distribution of the secondary crystalline phases (bright particles).

Figure 5.7 Annular dark-field image showing secondary crystalline phases enveloping the Si_3N_4 grains. The bright contrast of the secondary crystalline phases is due to the presence of Y. The bright film between two Si_3N_4 grains (indicated by an arrow) suggests that the film contains Y.

secondary crystalline phases, no specific relationships have been found between the type and morphology of the secondary phases.

5.2.2 Structure of Grain-Boundary Films

The lattice fringe imaging technique was used to measure the thickness distribution of grain boundary films in the undoped and Ba doped material. The results are shown in Figure 5.8 and Figure 5.9. Both materials display a Gaussian distribution for the film widths of the uncrept samples, with a mean value of 1.00 ± 0.1 nm and 1.2 ± 0.1 nm for the undoped and Ba doped Si_3N_4, respectively. The standard deviation of 0.1 nm is within the experimental error expected for the high resolution lattice imaging technique (Cinibulk et al 1993). This suggests that grain boundary films have a constant value in a given material, independent of grain misorientation. The addition of 800 ppm Ba increased the film thickness by about 20%. In our previous work (Jin 1995), we measured the film thickness distribution in the undoped material and a Ba doped material using the Fresnel fringe imaging technique and obtained similar results. While the undoped material had a film thickness of 1 nm, the Ba doped material had a film thickness of 1.4 nm. It should be noted that the Ba doped materials in our previous work and in the present work are essentially two different materials. They were fabricated at 1925°C for different times (0.5 h for previous work and 1 h for present work) and had different densities (87% theoretical density for previous work and 95% theoretical density for present work). Although they have the same nominal composition of the starting powder (800 ppm Ba), the composition of the residual intergranular amorphous phase may be different after

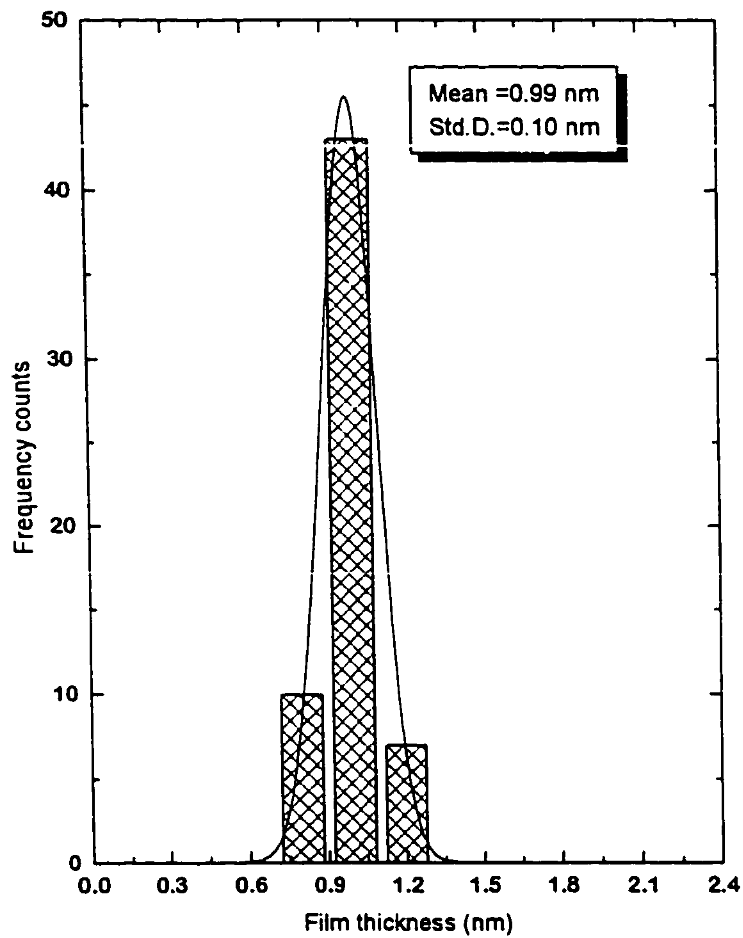

Figure 5.8 Histogram of the grain-boundary film thickness distribution in the as-sintered undoped material. The mean thickness value and the standard deviation are shown.

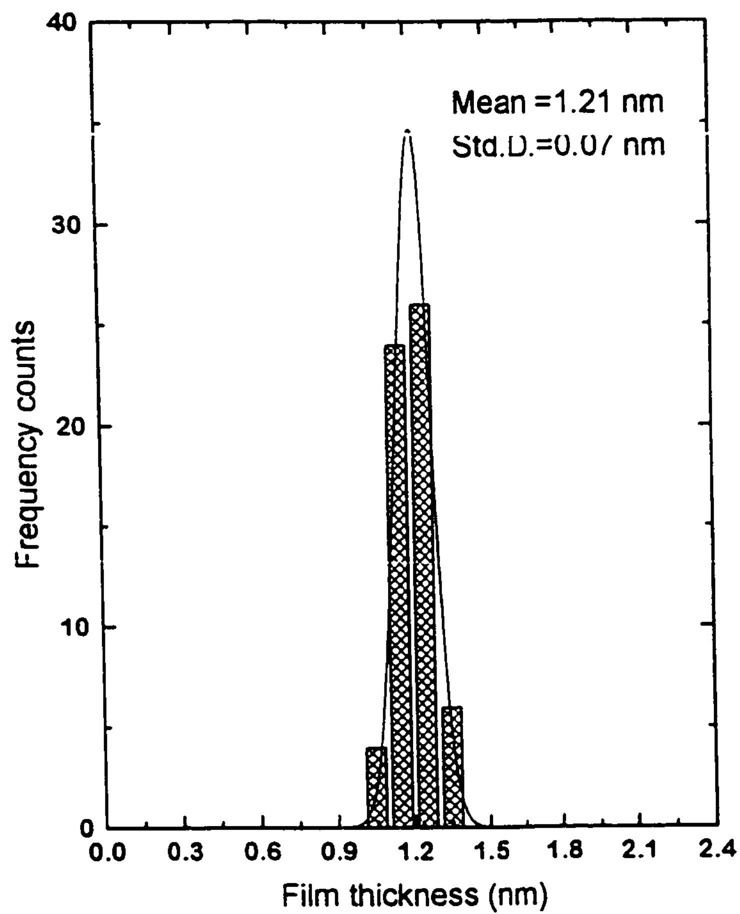

Figure 5.9 Histogram of the grain-boundary film thickness distribution in the as-sintered Ba doped material. The mean thickness value and the standard deviation are shown.

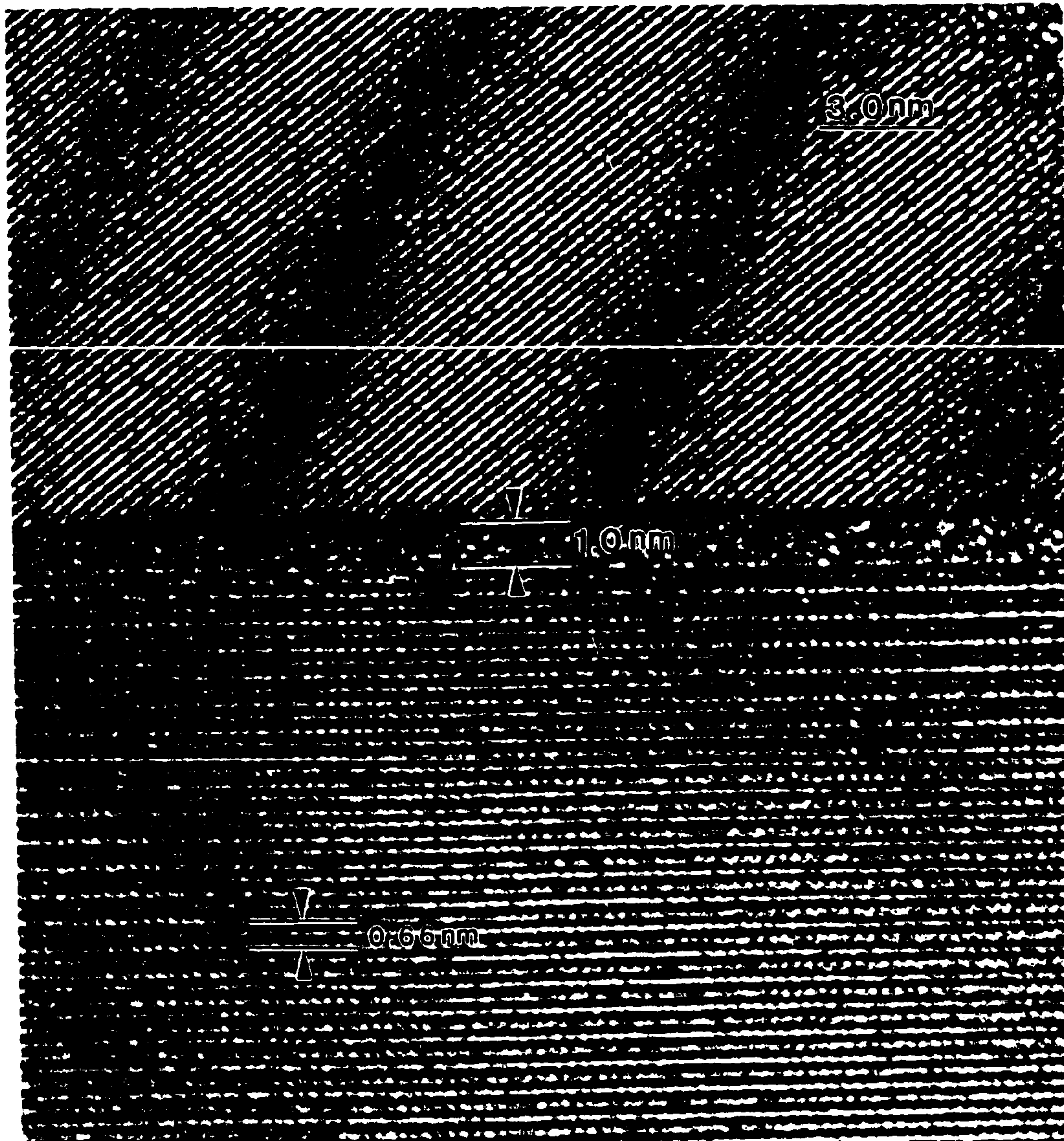

Figure 5.10 High-resolution lattice image of a Si_3N_4 grain boundary in the as-sintered undoped material, showing an amorphous intergranular film thickness of 1.0 nm. The lattice fringes in the lower grain are parallel to the $\{10\bar{1}0\}$ plane whose planar spacing is 0.66 nm.

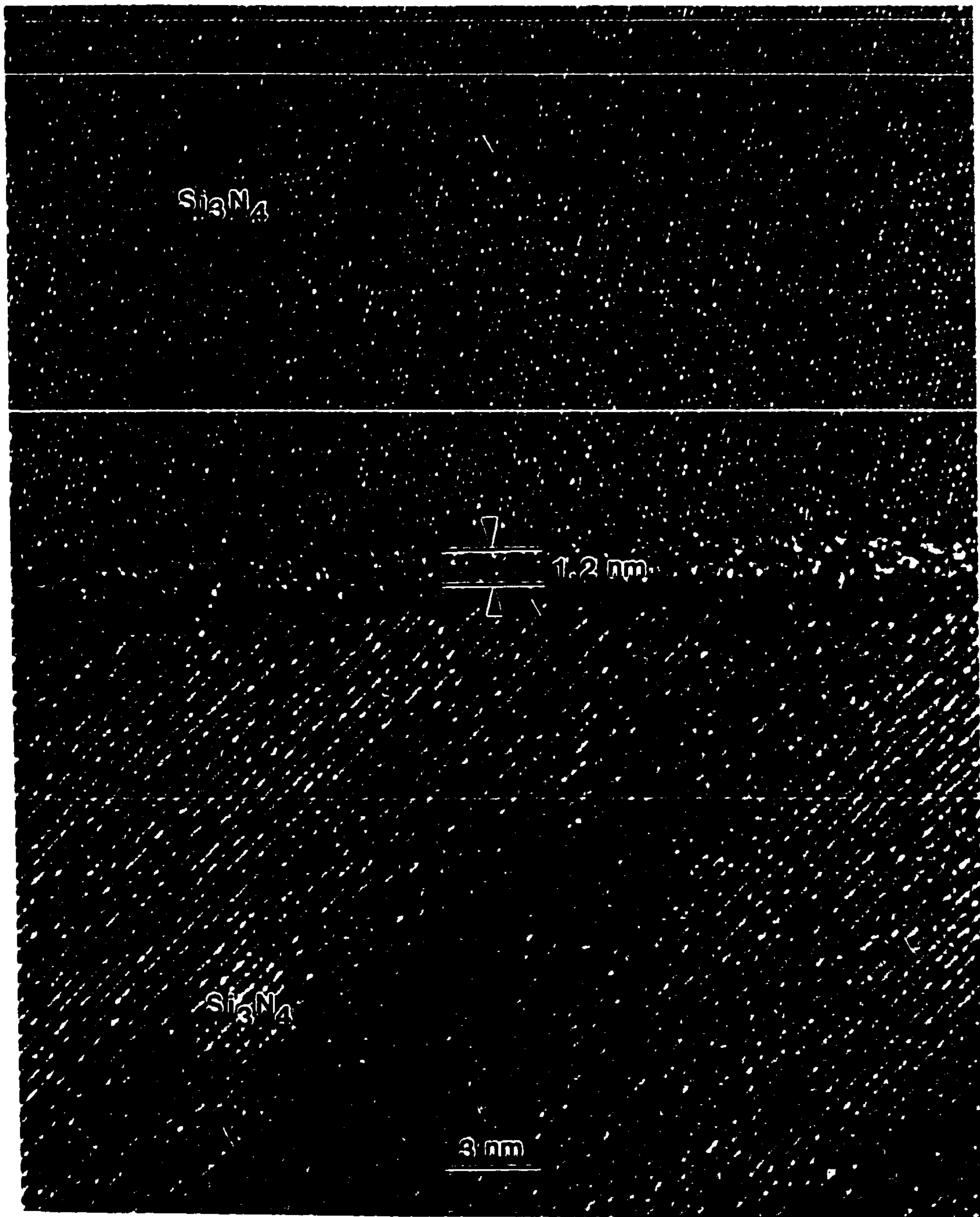

Figure 5.11 High-resolution lattice image of a Si_3N_4 grain boundary in the as-sintered Ba doped material, showing an amorphous intergranular film thickness of 1.2 nm. The lattice fringes in the lower grain are parallel to the $\{10\bar{1}0\}$ plane whose planar spacing is 0.66 nm.

sintering. Representative grain boundary films obtained by the HREM technique are shown in Figures 5.10 and 5.11 for the two materials.

The Fresnel fringe imaging technique was used to measure the film widths at Si_3N_4 grain boundaries in the Y_2O_3 doped material. At the uncrept grip end of the tensile creep specimen, the data show a Gaussian distribution with a mean value of 0.72 ± 0.13 nm (Fig.5.12). The standard deviation of 0.13 nm is within the experimental error of ± 0.15 nm expected for the Fresnel fringe imaging technique (Tanaka et al 1994c, Jin et al 1998). Similar to the undoped and Ba doped material, this also suggests that there exists a characteristic value of grain boundary film widths in the undeformed Y_2O_3 doped material, independent of the grain boundary misorientation.

Three types of secondary crystalline phases were present in the Y_2O_3 doped material. Since four different phases co-exist in the microstructure, i.e., three secondary crystalline phases and the β-Si_3N_4 matrix, there should be ten different types of boundaries in total which include both "homophase" boundaries (between grains of the same phase) and "heterophase" boundaries (between grains of different phases). In general, only four types of boundaries (i.e., Si_3N_4/Si_3N_4 and Si_3N_4/secondary phase) were commonly observed while the boundaries between the secondary phases themselves were rarely seen. This is because most of the secondary phases were present at multigrain junctions as single crystals (denoted by arrows in Figure 5.3). Investigation of a number of Si_3N_4-grain boundaries by using the lattice fringe imaging technique confirmed the results obtained from the Fresnel fringe imaging technique (Figure 5.12), which indicate that the film

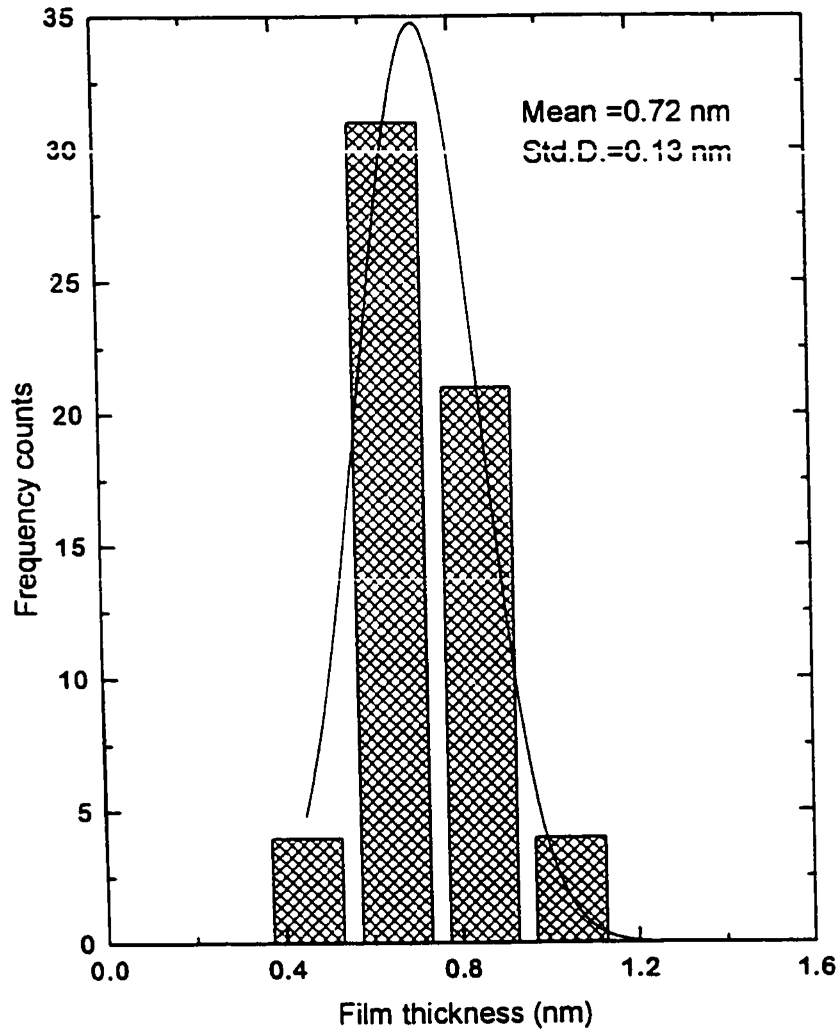

Figure 5.12 Histogram of the two-Si_3N_4-grain-boundary film thickness distribution in the Y_2O_3 doped material after complete crystallization. The mean thickness value and standard deviation are shown.

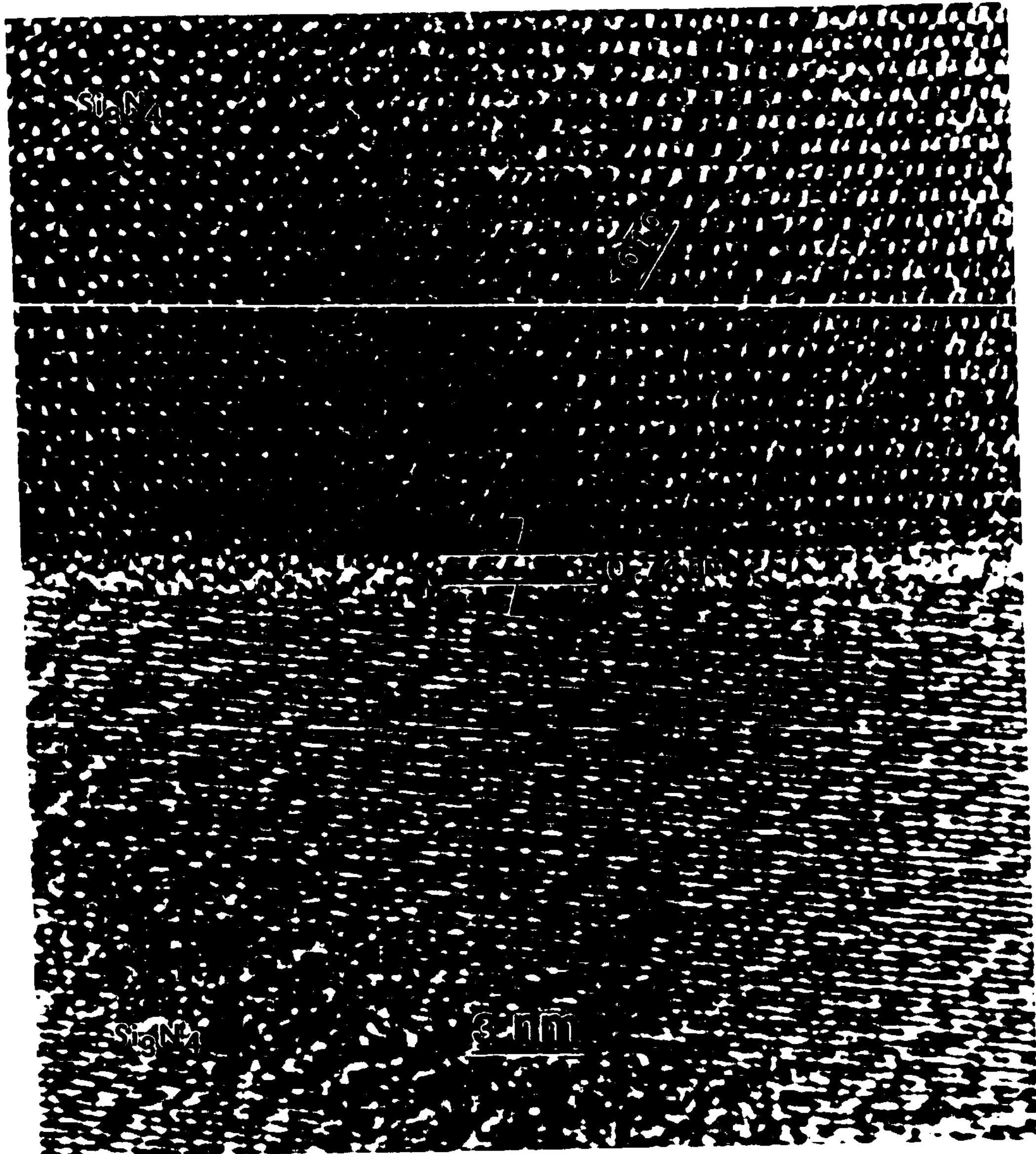

Figure 5.13 High-resolution lattice image of a homophase boundary in the grip end of the Y_2O_3 doped material after complete crystallization (1430°C, 690h), showing the film thickness of 0.74 nm.

thickness is a characteristic value, regardless of the grain misorientation. Even when atomic ledges exist at the Si_3N_4/glass interfaces, the thickness of the film remains constant. A representative lattice fringe image of the amorphous film along two-Si_3N_4-grain boundaries is given in Figure 5.13, showing the film thickness of 0.74 nm. It should be noted that the measured film width is relatively thin compared to Si_3N_4 fluxed with other rare-earth oxides (Wang et al 1996). In general, the amorphous films at all the three types of heterophase boundaries are much thicker than those at Si_3N_4-grain boundaries. Figure 5.14 shows the amorphous films at $Si_3N_4/Y_5(SiO_4)_3N$ and $Si_3N_4/Y_2Si_2O_7$ interfaces, indicating the film widths of 3-5 nm. No apparent difference in film thickness has been found between Si_3N_4/α-$Y_2Si_2O_7$ and Si_3N_4/δ-$Y_2Si_2O_7$ boundaries.

5.2.3 Chemical Composition of Grain-Boundary Films

The chemical composition of intergranular and/or interphase films was investigated by EDS in the STEM. The probe size used for EDS analysis of intergranular regions in the FEG TEM is nominally around 1 nm. In the undoped material, the grain-boundary films were found to contain excess oxygen. This is shown by the difference in the EDS spectra (Figure 5.15) taken at an edge-on grain boundary (solid line) and from within a Si_3N_4 grain (dashed line). The higher oxygen signal from the grain boundary compared to a measured point into the Si_3N_4 grain indicates the existence of oxygen in the grain boundary amorphous films. This is shown more clearly using x-ray mapping technique. The distributions of Si, O, N in the microstructure are shown in Figure 5.16. Compared with Si_3N_4 grains, less nitrogen and silicon are found in the grain boundary films. Similar results

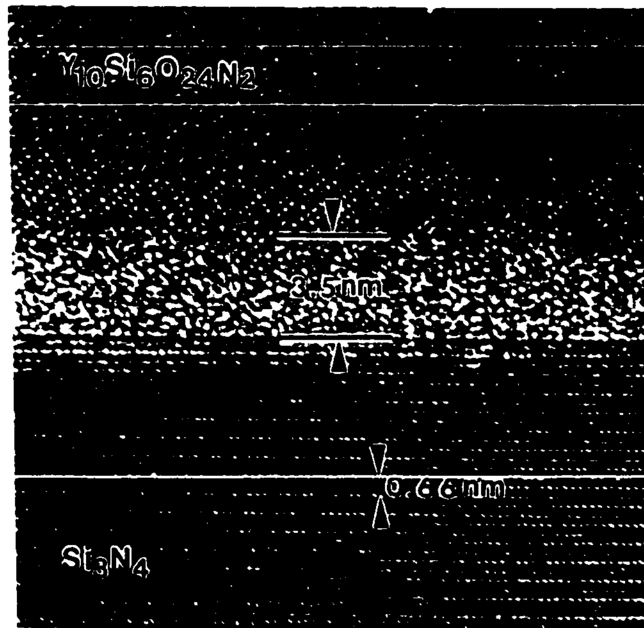

(a)

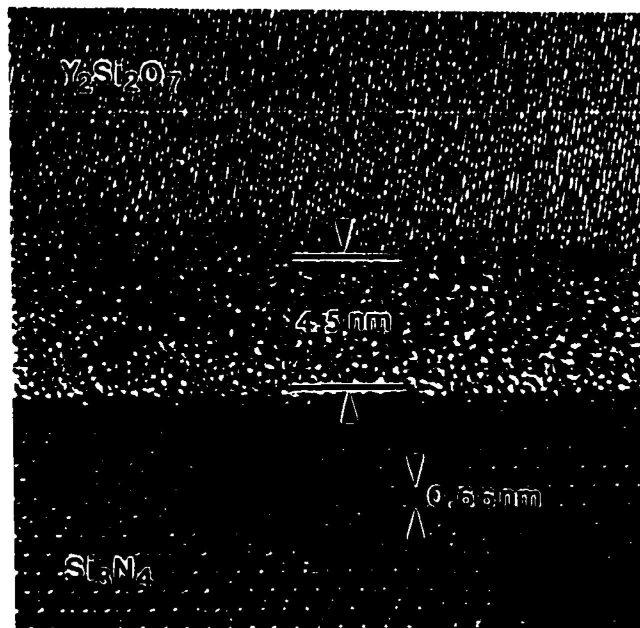

(b)

Figure 5.14 High-resolution lattice images of amorphous films at heterophase boundaries, (a) between Si_3N_4 and $Y_5(SiO_4)_3N$ showing a film thickness of 3.5 nm.; (b) between Si_3N_4 and $Y_2Si_2O_7$ showing a film thickness of 4.5 nm.

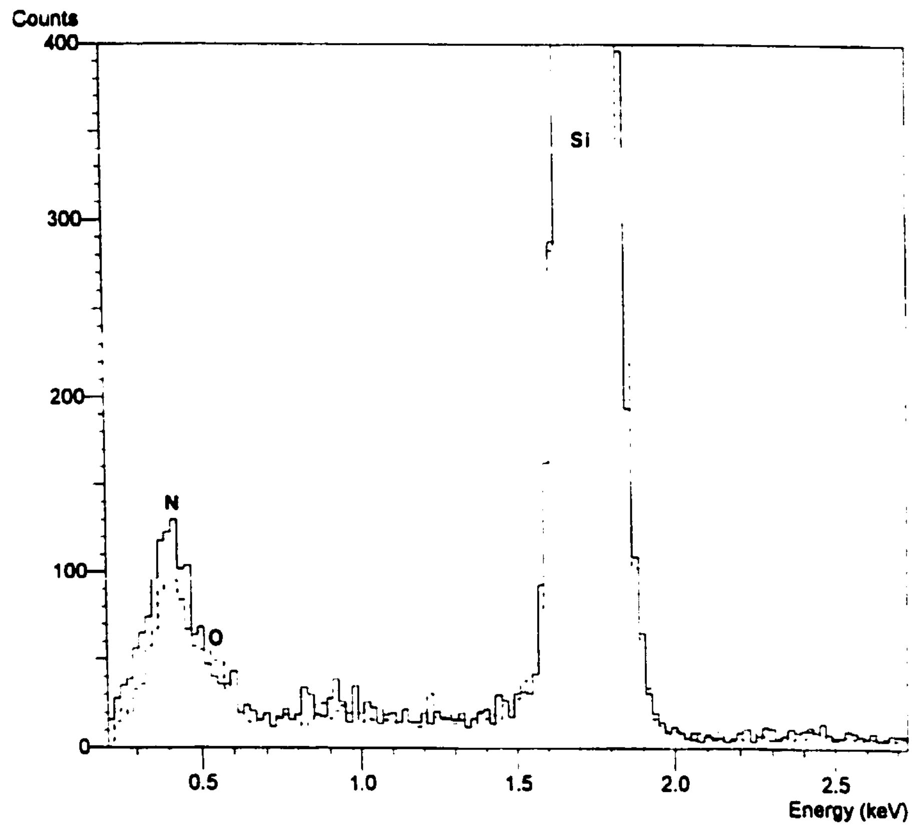

Figure 5.15 EDS spectra from the grain boundary film (dashed line) and 20 nm into the Si_3N_4 grain (solid line), indicating the presence of O in the grain boundary film.

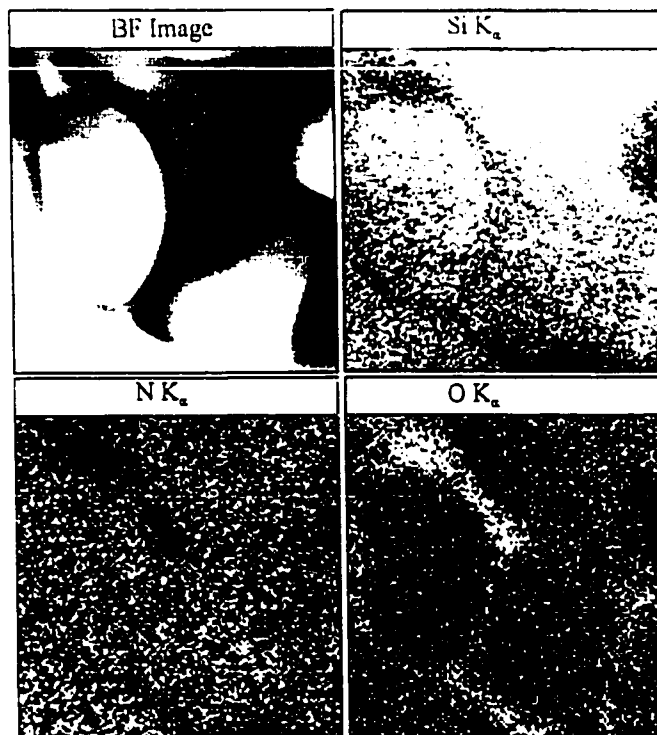

Figure 5.16 X-ray energy filtered images showing the excess of O, less Si and N at a grain boundary: (a) bright-field image: (b) Si-Kα X-ray mapping; (c) O-Kα X-ray mapping; (d) N-Kα X-ray mapping.

were obtained from the Ba doped material. Due to the very small amount of Ba in the material, no Ba could be detected in the grain-boundary films.

In the Y_2O_3 doped material, all the interfacial films were found to contain excess yttrium and oxygen (Figure 5.17). At a boundary amorphous layer between two Si_3N_4 grains, the presence of the heavy element yttrium caused a bright line in the annular dark-field micrograph (Figure 5.7). This is also confirmed by X-ray energy filtered imaging (Figure 5.18b) and X-ray line scanning across the grain boundary (Figure 18d). The image and signals were acquired by using an energy window of K_α for Y. The distribution of Y across and along a grain boundary was also analyzed using a 1 nm probe (Figure 5.19). Concentration profiles were obtained by point analysis using a step size of 1nm. The results show that the yttrium was concentrated in the amorphous film and homogeneously distributed along the grain boundary.

Quantitative composition analysis of the interfacial amorphous films could not be carried out due to interference from surrounding crystalline grains. At the Si_3N_4 grain boundaries, the surrounding Si_3N_4 grains contribute to some extent to the X-ray intensities of Si and N. In case of heterophase boundaries, the signal from all the elements in the amorphous film, i.e., Si, N, Y and O, will suffer from interference from the same elements in the Si_3N_4 grain and the secondary crystalline phase (containing Y and O).

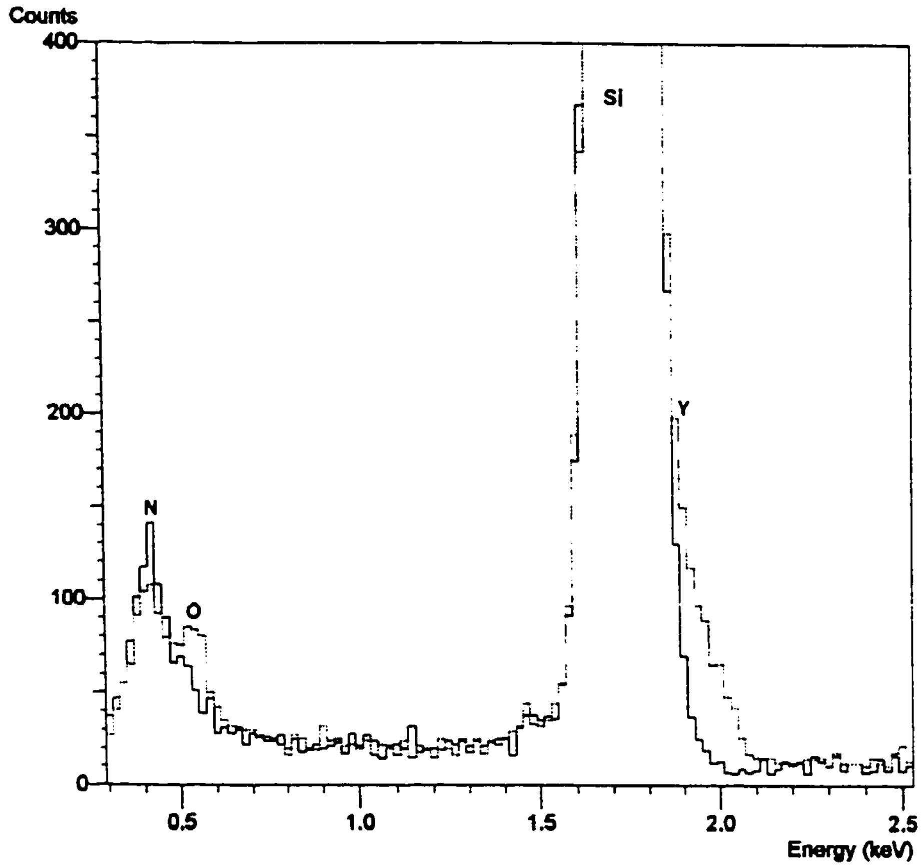

Figure 5.17 EDS spectra from the Si_3N_4 grain boundary (dash line) and 20 nm into the Si_3N_4 grain (solid line), indicating the presence of Y and O in the thin intergranular film.

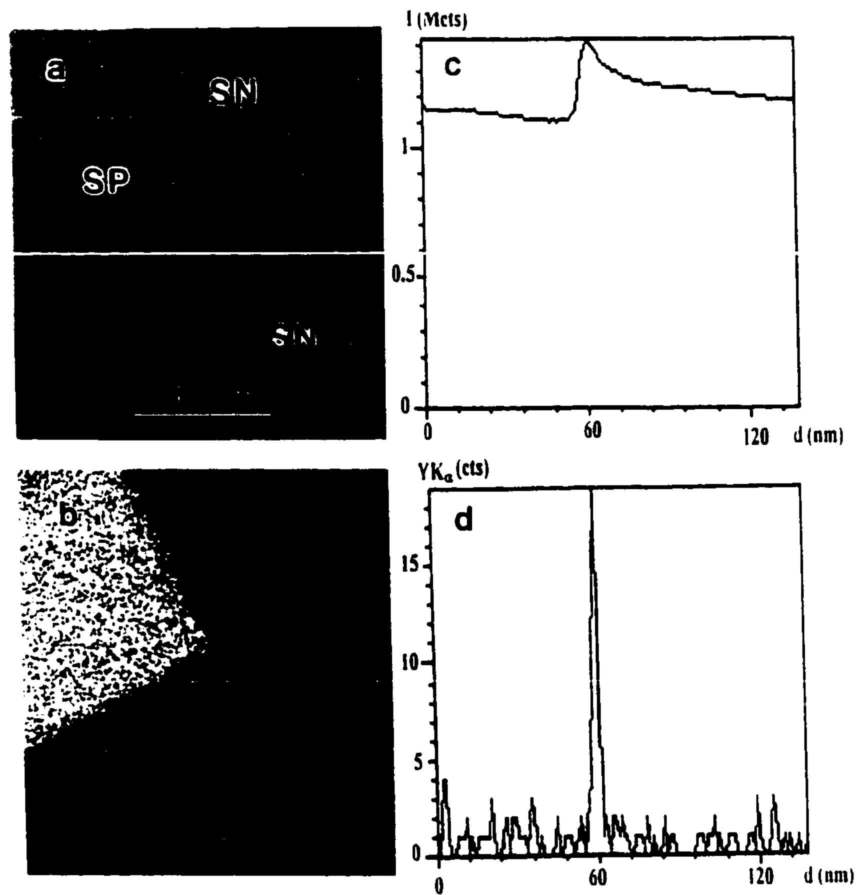

Figure 5.18 X-ray energy filtered images showing an Y-rich glassy phase at a Si_3N_4 grain boundary: (a) bright-field image; (b) Y-Kα X-ray mapping; (c) brightness across the grain boundary; (d) line scanning of Y-Kα across the grain boundary.

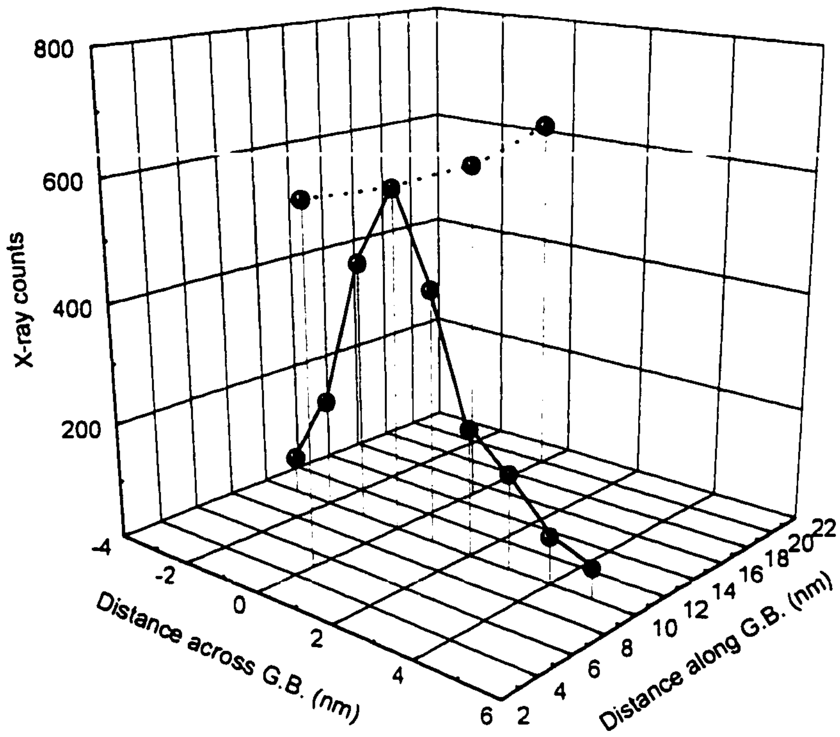

Figure 5.19 Yttrium concentration profile across (solid line) and along (dashed line) a grain boundary film. This profile was obtained from measurements in a step of 1 nm.

5.3 Discussion

5.3.1 Chemical Composition Dependence of Intergranular Film Thickness

Thin amorphous intergranular films were observed at all the grain and phase boundaries. They are generally assumed to consist of cations of the sintering aids and SiO_2 from the particle surfaces of the starting Si_3N_4 grains. Due to interference from adjacent grains and beam broadening, a quantitative chemical analysis has not been accomplished. Furthermore, the intergranular films are so thin (0.5-2 nm) and the amount of some sintering aids are usually too dilute, so even qualitative confirmation of the existence of sintering aids in the amorphous films has been difficult. In the present work, excess oxygen was found at grain boundaries in the undoped and Ba doped materials. This suggests that the intergranular phase is mainly SiO_2, which comes from the starting Si_3N_4 powder. No Ba was detected in the Ba doped material indicating that the barium level was below the limit of detectability. Both excess oxygen and yttrium were found at grain boundaries in the Y_2O_3 doped material, indicating that the thin intergranular amorphous film consists of Y_2O_3 and SiO_2.

The presence of sintering aids in the intergranular films strongly influences the properties of the films. Although measurements of the viscosity of the intergranular phase were not attempted in this work*, the film thicknesses observed were different, depending on

---

* For example, internal friction measurement at high temperature can be used to measure the viscosity of grain boundary films (Mosher et al 1976). However, this represents a major study in its own right.

the sintering additives. While the undoped material has a 1 nm grain boundary film, the addition of the sintering aids increases the film thickness to 1.2 nm (Ba addition) or decreases it to 0.7 nm (Y_2O_3 addition). In addition to this, the heterophase boundaries (i.e., Si_3N_4/secondary phase) always reveal a larger width of the amorphous interlayer compared to homophase boundaries (i.e., Si_3N_4/Si_3N_4).

The observations of this work, together with others (Kleebe et al 1992, Tanaka et al 1994b, Wang et al 1996), strongly suggest that the thickness of the intergranular film depends on the composition of the intergranular film and the two grains on either side of the film. It should be noted that differences in the thickness of the films for different additive systems have been correlated with the chemistry of the intergranular film by other investigators. Clear examples include the Si_3N_4 densified with Ca doped liquid (Tanaka et al 1994b) and lanthanide-based liquids (Wang et al 1996). In both cases, the film thickness increases either with the content of Ca addition or with the ionic radius of the lanthanide. Clarke (1987) was the first to postulate the existence of a stable equilibrium film thickness based on a continuum approach. He suggested that the equilibrium thickness is balanced by the interaction of an attractive van der Waals dispersion force (equation 2.2) and a repulsive steric force (equation 2.3) resulting from distortions of SiO_4^{4-} tetrahedra in the glass. In the undoped material, if the intergranular amorphous phase is assumed to be pure silica, the force balance at an equilibrium film thickness h is given by

$$\Pi_{disp} = \Pi_{st} \tag{5.1}$$

$$\frac{H_{\alpha\beta\alpha}}{6\pi h^3} = -\frac{a\eta_0^{\ 2}}{\sinh^2(h/2\xi)} \qquad (5.2)$$

where the Hamaker constant $H_{\alpha\beta\alpha}$ is 76×10^{-21} J for $Si_3N_4/SiO_2/Si_3N_4$, and $a\eta_0^2$ is 100MPa for SiO_2, as given by Clarke (1987). It has been suggested (Clarke 1987, Kleebe et al 1994b) that the correlation length ξ can be interpreted as the molecular unit of a SiO_4^{4-} tetrahedron which is 0.21 nm in height with a 0.26 nm O-O bond length. Using these parameters with ξ=0.22 nm (Kleebe et al 1994b), Clarke's theory (Clarke 1987) predicts an equilibrium film thickness of 1.03 nm. This estimate is in good agreement with the thickness measurements in the undoped material. The measured film thickness of the Ba doped material is about 1.2 nm, indicating that the addition of 800 ppm Ba increases the film thickness by about 20%. This result is consistent with the previous report by Tanaka et al (1994b). They studied the calcium concentration dependence of the intergranular film thickness in silicon nitride and found that 450 ppm Ca addition increased the grain boundary film thickness of a high purity Si_3N_4 from about 1 nm to about 1.5 nm. To explain the effect of impurity cations on the grain boundary film thickness, Clarke and his coworkers (1993) introduced a third force, i.e., an electrical double layer force (equation 2.4), to balance the film thickness equilibrium. It is thought (Tanaka et al 1994b, Kleebe et al 1994b) that the segregation of Ca^{2+} cations to the boundary provides charged species which results in the formation of a repulsive electric double layer force. A higher addition of Ca^{2+} can increase this repulsive force, leading to an increase in film thickness. Ca and Ba may influence the magnitude of the repulsive force in similar ways, therefore, the film thickness in the Ba doped material is higher compared to that in the undoped material.

Although the incorporation of impurities in the residual glass is generally expected to lead to a widening of the boundary width, the decreased film thickness in the Y_2O_3 doped material can still be explained by Clarke's theory (1987). As shown in equation 2.3, the magnitude of the repulsive steric force depends on the structural correlation length (ξ) and η_0. The latter describes the degree of epitaxy of SiO_4^{4-} tetrahedra to the Si_3N_4 grains. Although the influence of Y cations on the value of η_0 (0~1) is not known, it has been proposed (Tanaka et al 1994b) that Ca^{2+} in the otherwise pure SiO_2 is likely to reduce the structural correlation length of the glass by disrupting the network structure of the silica. They used this to explain why the film thickness initially decreases with a small amount of Ca addition (see Figure 2.2). If Y has a similar effect, then the film thickness becomes smaller due to a decrease in the structural correlation length. Obviously, the structural correlation length of different cation-modified glasses of equivalent composition is likely to depend on the specific cation. It has been proposed (Wang et al 1996) that a larger ionic radius of the cations would result in a larger structural correlation length, which in turn leads to an increase of the steric repulsive force. Generally, the rare earth ions all have similar electron configurations and a common form of oxide, R_2O_3. Compared to lanthanides such as La, Nd and Yb, Y has a smaller ionic radius. This probably is the reason why the film thickness in the Y_2O_3 doped material is smaller than those in the lanthanide doped materials investigated by Wang et al (1996), see Figure 2.3. It should be noted that there is no reason to exclude the possibility of the existence of an electrical double layer force in the Y_2O_3 doped material. In that case, the competition between the effects of a decrease in the steric repulsive force and the development of a repulsive electrical force determines the boundary width. The present observation of about 0.7 nm

for the film thickness suggests that the decrease in the steric force is determining. The decrease in film thickness due to the addition of impurities has also been reported in a ZrO_2 doped silicon nitrde, in which the grain boundary film thickness is only 0.5 nm (Kleebe et al 1992).

An interesting phenomenon noted in this work is that the amorphous films at heterophase boundaries are generally thicker than those at homophase boundaries. Similar results have also been reported by Vetrano et al (1993) and Kleebe et al (1992) in their studies of Yb_2O_3 doped silicon nitride materials. They found that the thickness of heterophase boundary films between Si_3N_4/Yb_2SiO_5 or $Si_3N_4/Yb_2Si_2O_7$ was always larger by 1 to 3 nm compared to the film width along Si_3N_4 grain boundaries. Clarke (1987) has suggested that the attractive van der Waals interaction is weaker at boundaries formed between dissimilar phases, therefore, the net equilibrium separation is wider. According to Kleebe et al (1992), some compounds such as $Y_2Si_2O_7$ are thought to be non-stoichiometric and may have higher surface charges at the crystal/glass interface. Therefore, the electrical double layer force may also contribute to the widening of the phase boundary film.

5.3.2 Crystallization of Intergranular Phase in Y_2O_3 Doped Material

It is evident that crystallization of the intergranular amorphous phase depends on the sintering additives and post-sintering heat treatments. No crystallization of the intergranular phase has been found in the undoped and Ba doped materials, even after heat treatment at 1400°C for up to 200h. This suggests that the as-sintered microstructure of these materials represents essentially the stable microstructure at creep temperatures

(about 1400°C in this study), at least prior to loading. As for the Y_2O_3 doped material, however, the ease of crystallization of the intergranular phase results in a very different microstructure at high temperatures compared to the as-sintered material. In the as-sintered state, most multigrain junctions were found to contain residual silicate glass (Wiederhorn et al 1993). The devitrification of the amorphous phase in the multigrain junctions occurs so rapidly during creep deformation that it is complete prior to loading (Wiederhorn et al 1993). Thus, to understand the high temperature creep mechanisms of this material, it is necessary to characterize the devitrified microstructure. Fortunately, both the extent and nature of the intergranular crystallization was found to be the same after annealing from 4h to over 4000h in the temperature range of 1330°C-1430°C (Wiederhorn et al 1993). In fact, advanced silicon nitride ceramics typically use Y_2O_3 or other rare-earth oxides as sintering aids (Gazza 1973, Rae et al 1975, Yeckley et al 1989). A high temperature heat treatment is usually applied to this class of silicon nitride to crystallize most of the amorphous intergranular phase, resulting in an increase in creep resistance (Tsuge et al 1975). In this section, discussions are focused on the crystallization of the intergranular phase in the Y_2O_3 doped material.

Three secondary crystalline phases, $Y_{10}(SiO_4)_6N_2$ and α and δ polymorphs of $Y_2Si_2O_7$ were found in this work by electron diffraction and EDS. Only the first two of these secondary crystalline phases have been reported in previous investigations of this material (Menon et al 1994, Yeckley et al 1989). The results suggest that the composition of the residual intergranular phase after sintering was in the compatibility triangle of Si_3N_4-$Y_2Si_2O_7$-$Y_{10}(SiO_4)_6N_2$ (shaded region in Figure 5.20). According to previous

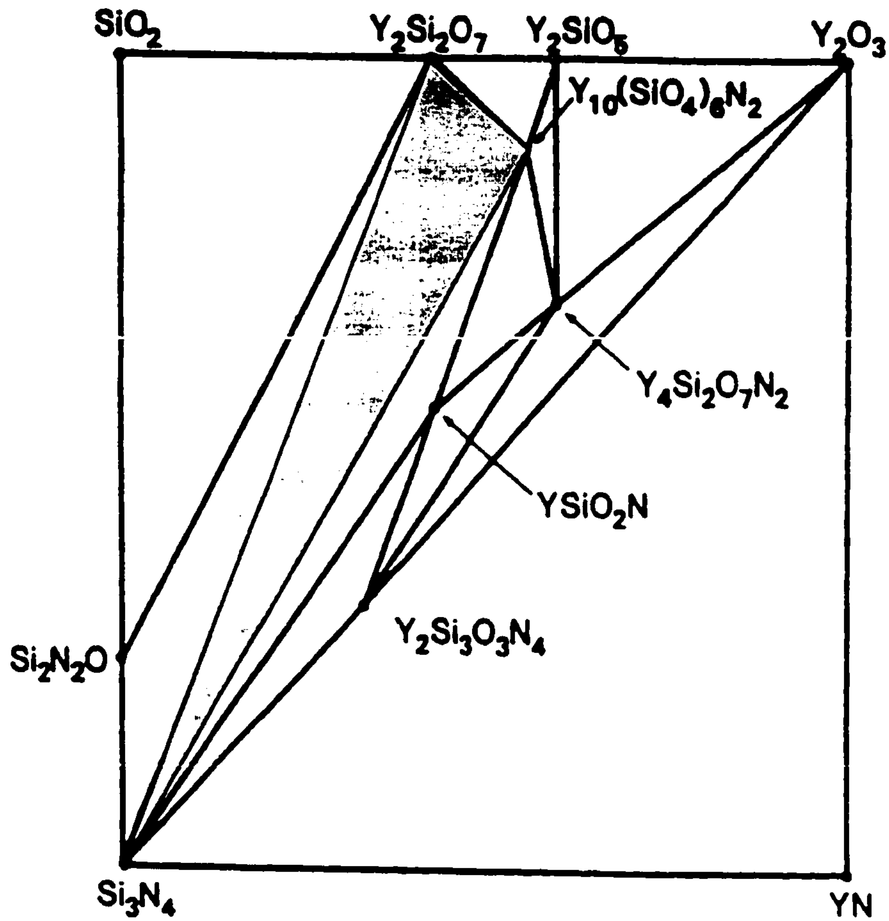

Figure 5.20 Phase relations in the system Si_3N_4-SiO_2-Y_2O_3-YN (Gauckler et al 1980).

investigations (Liddel and Thompson 1986), there are various polymorphs of $Y_2Si_2O_7$. Among them, α is the low temperature form (<1225°C) while δ is the high temperature form (>1550°C). Ito and Johnson (1968) have reported that the transition of $\alpha \rightarrow \beta$ polymorph occurs at a temperature of 1225°C. However, the β polymorph was not found in the present investigation. Since crystallization was carried out at 1430°C, the β to α transformation may occur during cooling. The δ polymorph was probably formed during cool-down from the processing temperature. This suggestion is supported by the observation of some small secondary-phase crystallites in the as-sintered material (Wiederhorn et al 1993). In fact, so far there is no clear understanding about the polymorphic transformations of $Y_2Si_2O_7$. According to Dinger et al (1988), δ-$Y_2Si_2O_7$ is the predominant species in glass crystallized at temperatures of 1300°C to 1400°C. Thus, another possibility is that the δ polymorph exists in the microstructure at high temperatures (1330°C-1430°C) as a stable form and transforms to the low temperature form, i.e., the α polymorph, during cooling.

The ease of crystallization of the intergranular phase in the 4 wt% Y_2O_3 doped material after heat treatment may be one important reason for the excellent high temperature properties such as creep resistance (Wiederhorn et al 1993). In the case of no crystallization, the amorphous phase is distributed at multigrain junctions as well as at grain boundaries. Cavity nucleation usually occurs at these multigrain junctions (Luecke et al 1995) whose size depends on the volume content of the sintering aids (Kleebe et al 1992). After annealing, most of the triple junctions are completely crystallized, except for some very small ones (a few nanometers in size). The fact that smaller pockets did not

crystallize is in agreement with the predictions of Raj and Lange (1981). The volume change associated with crystallization introduces a strain energy which opposes the transformation. So Raj and Lange's theory predicts that a glass pocket in a polyphase material must have a certain volume before crystallization can take place. It is not well understood why the intergranular phase is so easily crystallized. One possibility is that the amorphous phase undergoes only a very small volume change upon crystallization, thereby reducing the internal stresses that can accumulate and hinder further devitrification. However, while the densities of the secondary crystalline phases are available, the densities of their amorphous forms are not. Formation of secondary crystalline phases did not result in full crystallization of the intergranular regions; thin glassy films separated these phases from the surrounding Si_3N_4 grains. Therefore, crystallization does not eliminate the triple junctions but reduces their size significantly. Figure 5.21 shows a triple junction formed by two silicon nitride grains and one secondary phase grain, indicating the size of triple junction is of the same order as the heterophase boundary film thickness. Obviously, a much higher stress is required for cavity nucleation in such a small triple junction. It is interesting to note that the amorphous film thickness remains constant even for a curved crystal/glass interface. This indicates that the amorphous film at the Si_3N_4/secondary phase boundaries also tends to have an equilibrium thickness.

It should be mentioned that the partitioning of secondary crystalline phases from the liquid phase sintering medium may introduce a change in composition of the residual grain boundary phase. According to a previous investigation on the as-sintered material

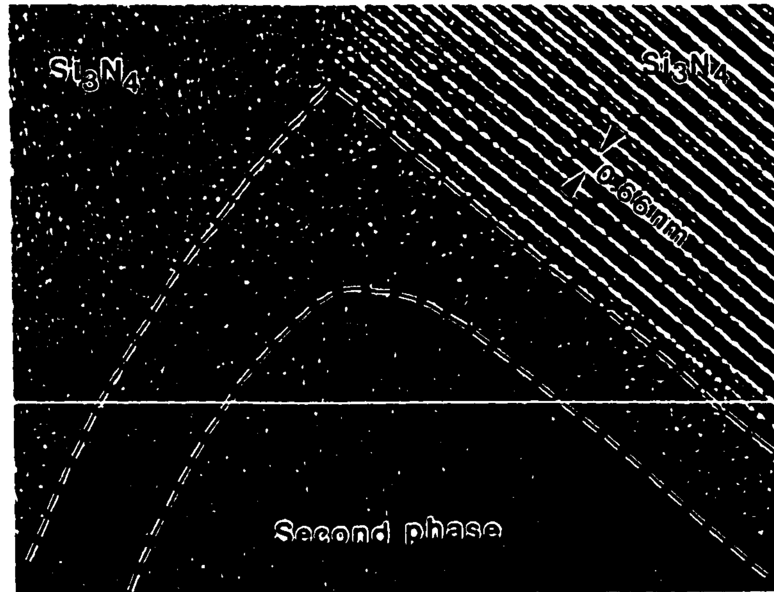

Figure 5.21 High-resolution lattice image of a triple junction formed by two Si_3N_4 grains and one secondary phase grain, showing the small size of triple junctions left after multigrain junction crystallization.

(Wiederhorn et al 1993), the composition of the amorphous phase is roughly 0.4 SiO_2 and 0.6 Y_2O_3. This implies that the formation of $Y_2Si_2O_7$ or $Y_5(SiO_4)_3N$ depleted the remaining liquid of Y and hence shifted the composition of the residual liquid/glass phase towards a lower ratio of Y/Si.

Investigation of the effect of oxidation on the crystallization of the intergranular phase was not attempted. Theoretically, an outward diffusion of Y moves the composition of the material towards the Si_3N_4-SiO_2 side of the Si_3N_4-SiO_2-Y_2O_3-YN phase diagram (Figure

5.20). This may result in the formation of secondary crystalline phases which contain less Y. On the other hand, the grain boundary amorphous phase provides a favourable diffusion path for oxygen into the material (McDonough et al 1981). This favours the formation of secondary crystalline phases which have a higher O:N ratio in their total anion content (Falk et al 1987). Among the secondary crystalline phases observed, $Y_2Si_2O_7$ and Y,N-apatite, only $Y_2Si_2O_7$ has less Y and high ratio of O:N. It is possible that yttrium disilicate forms in the region close to the oxide scale at high temperatures whereas Y,N-apatite phase is favoured in the interior of the material.

5.4 Summary

The present study has shown that the general microstructure of silicon nitride consists of equiaxed and acicular β-Si_3N_4. An intergranular amorphous phase is always present at grain- and phase-boundaries. The residual sintering liquid at multigrain junctions exists either in the crystalline or amorphous form, depending on the sintering aids and post-sintering heat treatments. Both the undoped and Ba doped materials contain an amorphous phase at the multigrain junctions as well as at grain boundaries. The high temperature microstructure of the Y_2O_3 doped material contains secondary crystalline phases. Crystallization takes place in the larger glass pockets while smaller ones and intergranular films remain undevitrified.

High resolution and analytical electron microscopy was performed to study the amorphous intergranular films. Within experimental error, each material reveals a characteristic film thickness independent of grain misorientation. This strongly suggests that an equilibrium

thickness exists, supporting Clarke's theory. The variation of the grain boundary film thickness in different materials is closely related to changes in grain-boundary phase composition, which is shown to contain the cations of the sintering aids and SiO_2 from the starting powders. The undoped material exhibited a film thickness of 1nm. The addition of BaO increased the film thickness to 1.2 nm whereas the Y_2O_3 fluxed material showed an amorphous grain boundary film (0.7 nm) in width. In general, the heterophase boundary film thickness is always larger than the film width along grain boundaries. Depending on the chemistry of the grain boundary film and the adjacent grains on either side of the film, the attractive van der Waals force and repulsive forces (steric force and electrical double layer force) are changed, thus stabilizing an equilibrium film thickness, characteristic for each material or for each type of boundary.

Chapter 6

VISCOUS FLOW CREEP OF SILICON NITRIDE

Part I Experimental Observations

6.1 Introduction

Viscous flow of intergranular amorphous films has been suggested as one of the mechanisms responsible for high-temperature creep deformation of glass-containing ceramics such as silicon nitride (Lange 1975, Pharr and Ashby 1983, Drucker 1964, Dryden et al 1989, Chadwick et al 1992, Wilkinson 1994). The presence of intergranular amorphous films in silicon nitride results from the liquid which forms during processing when the silica on the surface of the Si_3N_4 powders reacts with the sintering additives (see Chapter 5). Upon application of a load at high temperatures, the amorphous films may flow from grain boundaries under compression to those under tension due to their low viscosity, while the Si_3N_4 grains remain rigid. This process has been described by several models, based on the assumption of a regular array of cubic (Lange 1975, Pharr et al 1983) or hexagonal (Drucker 1964, Dryden et al 1989, Chadwick et al 1992) grains. The creep response due to viscous flow predicted by the models (Dryden et al 1989, Chadwick 1992) is a relatively constant initial strain rate followed by a rapid decrease in strain rate when a limiting strain is approached. The limiting strain corresponds to the situation in which there is no fluid left between the boundaries under compression. This limiting strain is $H_o/\sqrt{3}\,L$ in compressive creep, where $2H_o$ is the initial grain-boundary film thickness and 2L is the facet length of the hexagonal grains (Dryden et al 1989). This "exhaustion creep" (Wilkinson 1994) behaviour has been observed experimentally in several Si_3N_4

ceramics (Chadwick et al 1993, Wilkinson 1994, Jin 1995), thus providing indirect evidence for viscous flow as a creep mechanism. Obviously, to obtain direct evidence for viscous flow, information of the film thickness distribution before and after creep is required.

The intergranular film widths in the as-sintered materials (i.e. before creep) are believed to have a unique value, independent of grain misorientation. Experimental evidence for this comes from the present study on microstructural characterization of the experimental materials (Chapter 5), together with extensive studies of the grain-boundary films in different materials by other investigators (Kleebe et al 1992, 1993b, 1994b, Tanaka et al 1994b, Pan et al 1996). The thickness of an intergranular film has been explained by Clarke and co-workers (Clarke 1987, Clarke et al 1993) as due to a balance between the attractive van der Waals force and repulsive forces produced in the intergranular film. The constant intergranular film thickness in the as-sintered materials not only facilitates the study of the film thickness distribution before and after creep, but is also useful for validating existing viscous flow models which are invariably based on an initial uniform thickness of the intergranular films.

In our previous work (Jin 1995), the distribution of intergranular film widths in the undoped and a Ba doped material after compressive creep was also investigated. The widths of grain-boundary films were measured by the defocus Fresnel fringe imaging (FFI) technique. The results of a statistical analysis of a number of grain-boundary films indicated that the standard deviation of the film widths of a given material was considerably larger after creep than before, supporting the viscous flow mechanism. It

should be noted, however, that high-resolution lattice fringe imaging (LFI) has been suggested as the method capable of providing the most direct and the most accurate (±0.1 nm) measurements of nano-scale grain-boundary film thickness (Cinibulk et al 1993). FFI, on the other hand, is an indirect and less accurate (±0.15 nm) method (see Chapter 4). These two techniques have been discussed in detail by several investigators (Cinibulk et al 1993, Clarke 1979, Krivanek et al 1979). The advantage of FFI over LFI in determining grain-boundary film thickness is that the former is much easier to operate experimentally. Obviously, the film thickness distribution before and after creep, as measured by LFI can provide more convincing evidence for viscous flow creep.

Assuming that viscous flow indeed occurs during compressive creep of silicon nitride ceramics with a simple microstructure as in the undoped and Ba doped materials (Jin 1995), one may ask such questions: Is viscous flow a general phenomenon regardless of the stress state and the complexity of microstructure? Does viscous flow occur only in the initial stage of creep as suggested previously (Chadwick et al 1993, Wilkinson 1994) or throughout the whole creep process? This chapter tries to answer these questions. Firstly, LFI was employed to measure the film thickness distribution of the undoped Si_3N_4 material after compressive creep. The purpose is to provide a clear confirmation of the redistribution of the intergranular amorphous films during creep deformation. Secondly, interrupted creep tests were conducted at 1400°C under a compressive stress of 100MPa using the Ba doped material. The film thickness distribution at different strain values was measured and compared with the uncrept material. Finally, the tensile creep tests were conducted for the Y_2O_3 doped material at 1430°C under different stresses. The

measurements of the film thickness distribution before and after creep together with the creep response were used to investigate the viscous flow process in this material.

6.2 Results

6.2.1 Creep Response

The creep behaviour of the undoped material at 1400°C under different compressive stresses is shown in Figure 6.1. The strain-time curves exhibit a continously decreasing creep rate (Figure 6.1a). In order to highlight the initial creep behaviour, the data are presented in terms of strain rate as a function of strain on a log-log plot (Figure 6.1b). The initial creep rate does not vary significantly with strain. After a strain of about 1×10^{-3} to 4×10^{-3}, the strain rate decreases by about one order of magnitude, suggesting two distinct creep stages. This behaviour is not caused by densification of the porous material under the applied load. Precise density measurements (Jin 1995) show that there is no density increase after creep. The stress exponent n of the strain rate in the first creep stage (first plateau) is 1.7 ± 0.4 while it is about 1 in the second creep stage (second plateau).

The Ba doped material was tested at 1400°C under different compressive stresses (50, 100 and 200MPa). Two distinct creep stages were also observed, with about one order of magnitude difference in strain rate between them. The stress exponent of strain rate in the second creep stage is about 2. For the stress level of 100MPa, the tests were interrupted at three different times (7h, 40h, 200h), corresponding to three different strain values, with one at the end of the first stage (ε=0.0049) and the other two in the second stage

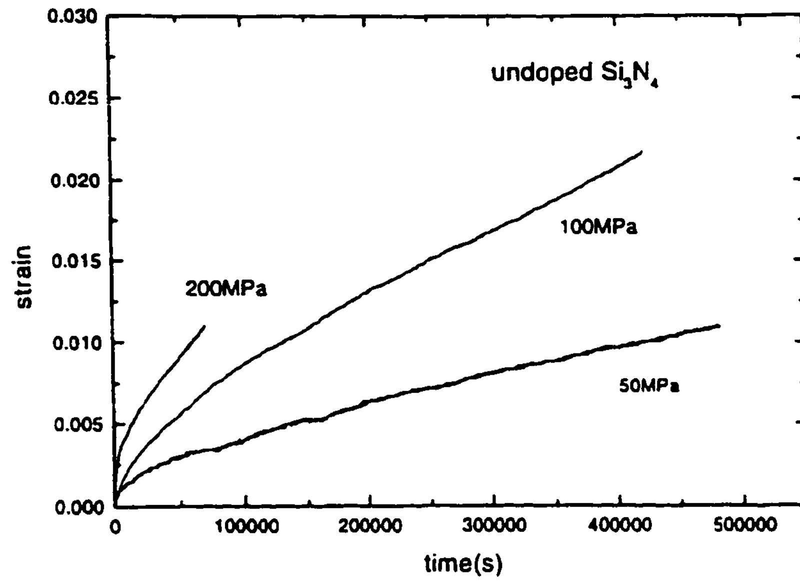

(a)

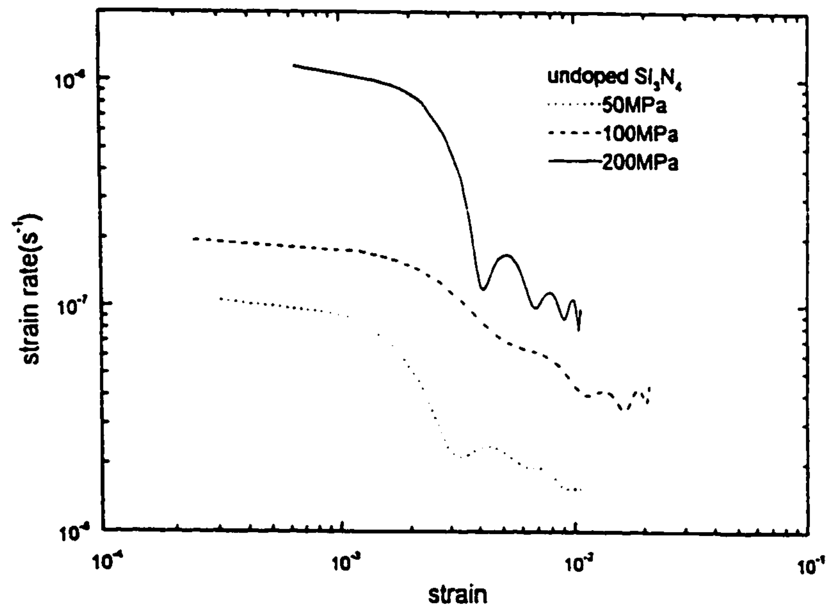

(b)

Figure 6.1 Creep response for the undoped material at 1400°C under different compressive stresses (Jin 1995): (a) strain-time curves, (b) strain rate vs strain curves.

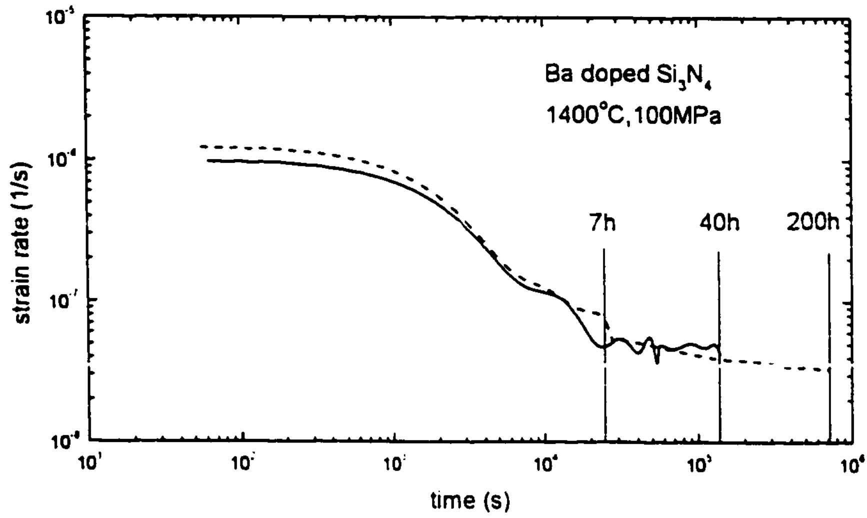

(a)

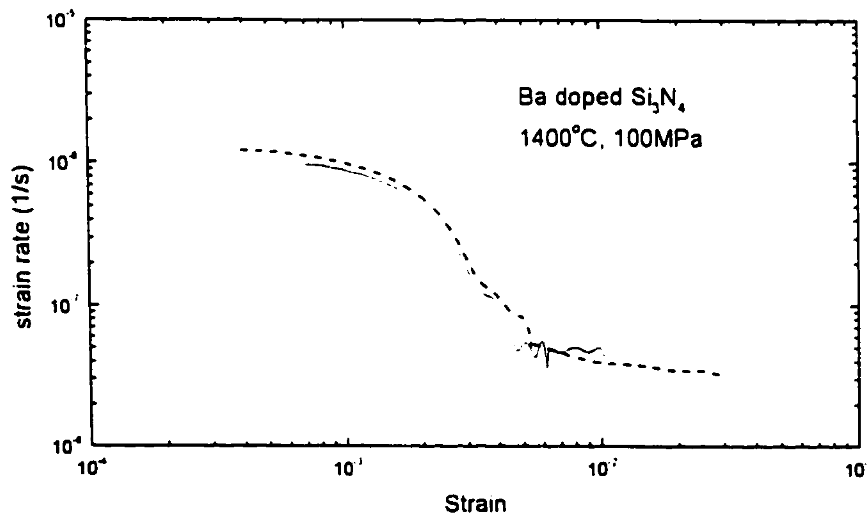

(b)

Figure 6.2 Creep response for the Ba doped material at 1400°C, 100MPa for different time periods (7h, 40h, 200h): (a) strain rate vs time curves; (b) strain rate vs strain curves. The solid curve is for creep of 40h while the dashed curve is for creep of 200h.

(ε=0.0104 and 0.0307). The strain rate-time and strain rate-strain curves for the interrupted creep tests are shown in Figure 6.2. The solid curve is for creep of 40h while the dash line is for creep of 200h. As can be seen, the creep testing results are very reproducible.

The creep response of the Y_2O_3 doped material at 1430°C under different tensile stresses is presented in Figure 6.3. A plateau region of constant strain rate is seen in the initial stage. The larger the applied stress, the higher is the initial strain rate. After a strain of about 3×10^{-3}, the strain rate decreases measurably. This behaviour is very similar to the creep response exhibited in the undoped and Ba doped materials which have no secondary crystalline phase grains. The stress exponent of the second creep stage depends on the

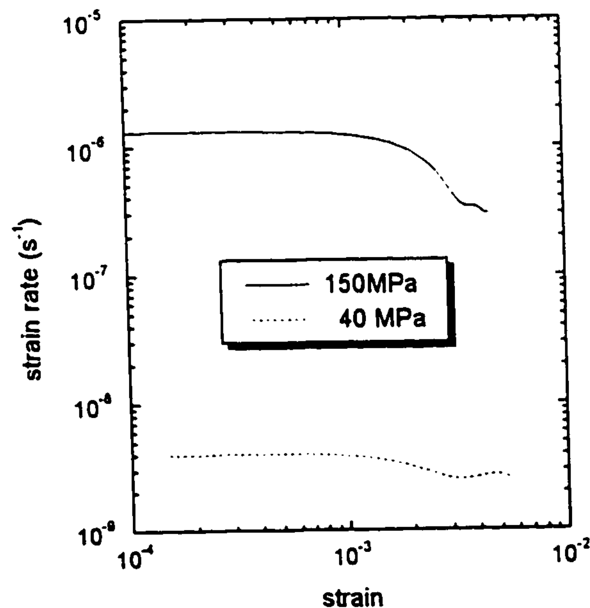

Figure 6.3 Creep response of the Y_2O_3 doped material crept at 1430°C under stresses of 40 MPa and 150MPa, showing initial constant strain rate followed by a measurable decrease in strain rate at a strain of 3×10^{-3} (Luecke 1997).

stress, with a value of 2.3 ± 0.7 for the low stress range (40 MPa ≤ σ ≤ 100MPa) and a value of 7.3 ± 2.0 for the high stress range (100MPa ≤ σ ≤ 150 MPa) (Luecke et al 1995).

6.2.2 Film Thickness Distribution After Creep

Direct evidence for viscous flow of the intergranular phase can be obtained by measuring the film thickness distribution before and after creep. The film thickness distribution in the uncrept samples of the experimental materials has been discussed in Chapter 5. HREM investigations indicated that the amorphous film had a constant thickness along the entire grain boundary. Statistical analysis of a number of grain boundaries in each of the materials reached the same conclusion: the film thickness is a characteristic value, independent of grain misorientation. After creep, however, the film thickness distribution exhibits a significant difference.

In the crept sample of the undoped material (1400°C, 200MPa for 20h), the film widths displayed a bimodal distribution with the first peak at 0.60 nm and a second peak at 1.53 nm (Figure 6.4). It should be noted that oxidation during the creep process has little effect on this distribution since no change in film thickness was observed in this material after annealing in air at 1400°C for 120 h (Jin 1995). The bimodal distribution in the film widths indicates that some grain boundaries become thinner and others become thicker. It is known that the film widths are confined to a narrow range before creep, therefore, this strongly suggests that viscous flow indeed occurs during creep deformation. Representative HREM images of a thinner boundary and a thicker boundary are shown in Figure 6.5.

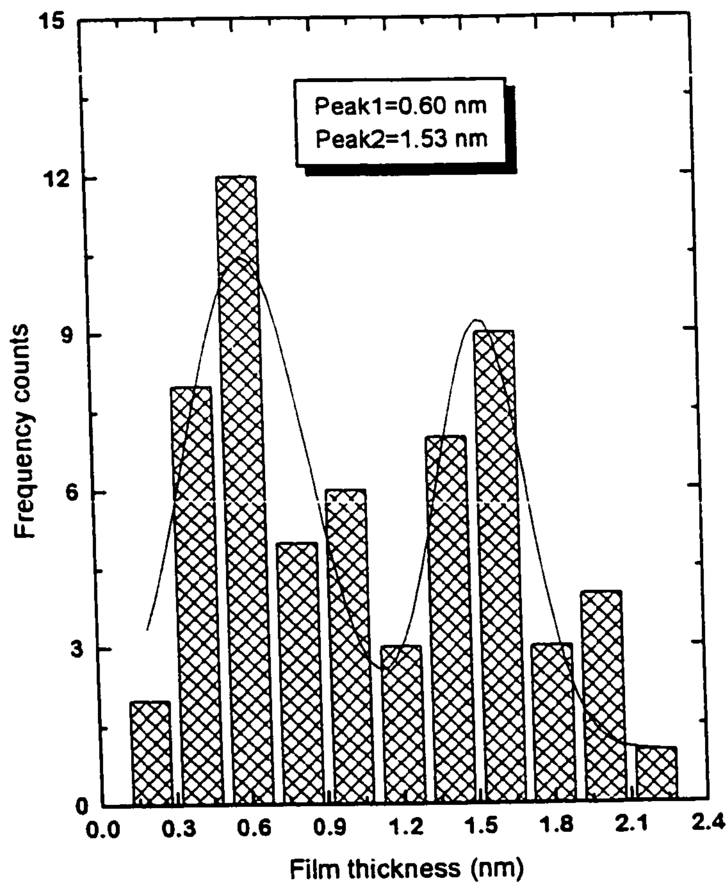

Figure 6.4 Histogram of the grain-boundary film thickness distribution in the undoped material after creep at 1400°C for 20h under a stress of 200MPa (total strain 1.1%). Two peaks at 0.6 nm and 1.53 nm indicate a bimodal distribution of the grain-boundary film widths after creep.

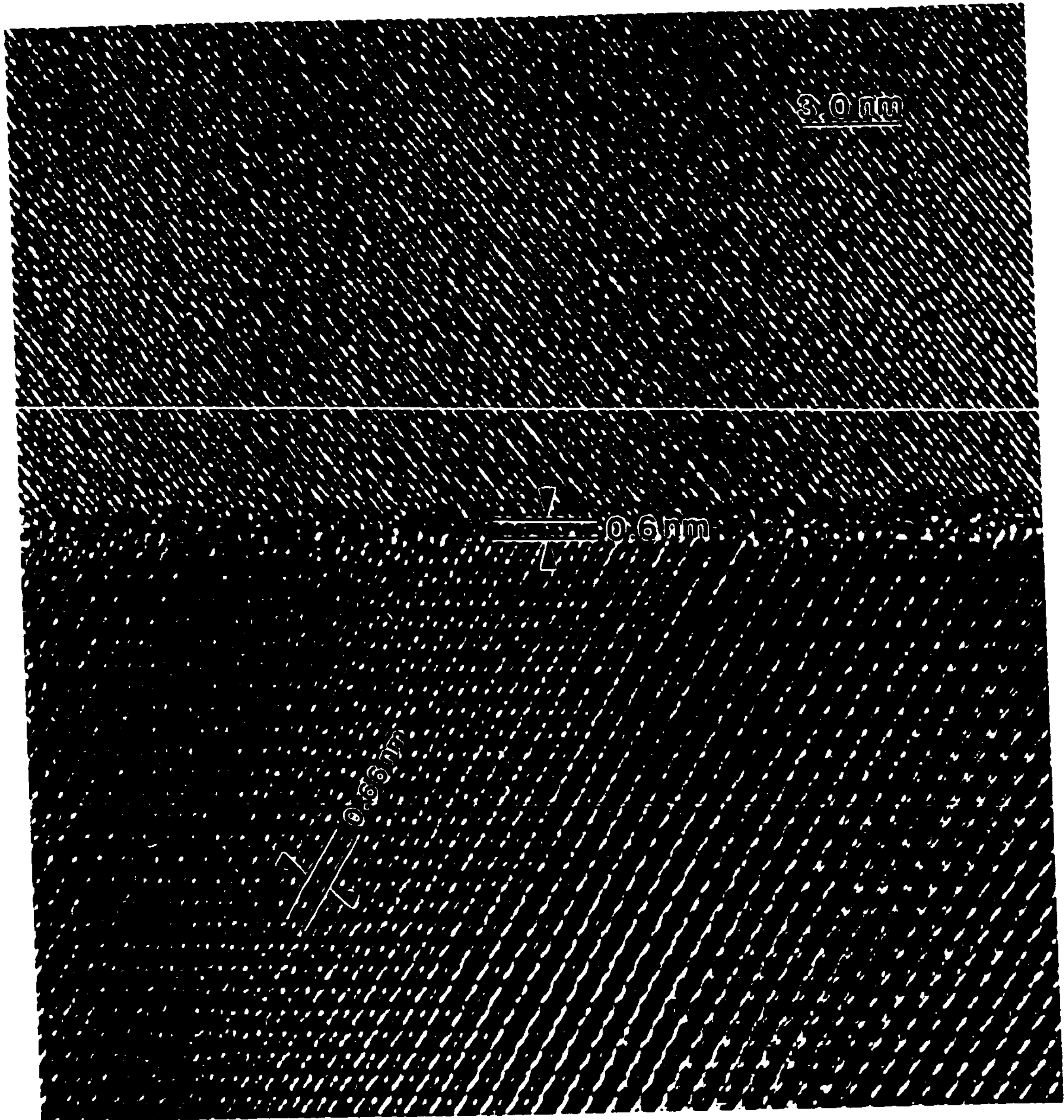

(a)

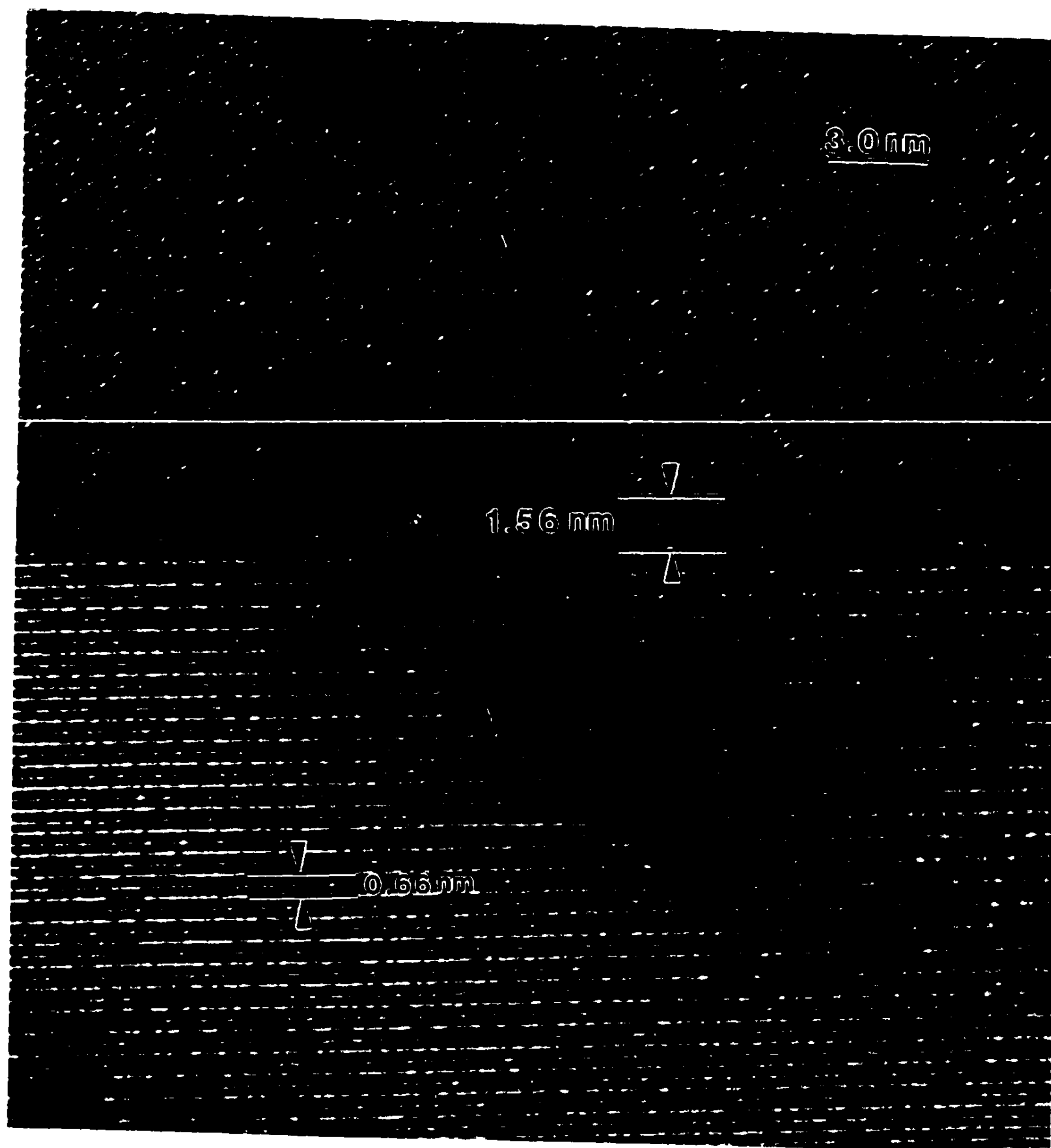

(b)

Figure 6.5 High-resolution lattice images of grain-boundary amorphous films in the experimental material crept at 1400°C under 200MPa for 20h, showing a large difference in film thickness: (a) a thinner grain boundary with a film thickness of 0.6 nm; (b) a thicker grain boundary with a film thickness of 1.56 nm. In both micrographs, the $\{10\bar{1}0\}$ planar spacing of 0.66 nm were used for accurate determination of the grain-boundary film thickness.

The film thickness distributions at different strains were measured in the Ba doped material (1400°C, 100MPa), and the results are shown in Figure 6.6. As can be seen, a bimodal thickness distribution was displayed for all the grain boundary films examined in a given sample (or at least most grain boundaries in the sample crept for 200h). No apparent difference was found in the positions of the two peaks after creep from 7h to 200h. In all cases, the first peak is around 0.85 nm while the second peak is about 1.4 nm. This suggests that viscous flow mainly occurs in the initial stage of creep. Once a new equilibrium film thickness distribution is established under an applied stress, it would become stable during the second stage of creep unless other processes, which could cause redistribution of the boundary phase, occur. It is worth noting that after creep of 200h, some very thick grain boundaries (3-4 nm) were occasionally observed (Figure 6.6c). This may be caused by local cavitation during the second creep stage and will be discussed in the next section. A thinner film and a thicker film in the crept samples are shown in Figure 6.7.

The distribution of homophase-boundary (i.e., Si_3N_4/Si_3N_4) film widths in the Y_2O_3 doped material after tensile creep (1430°C,40MPa,690h) is shown in Figure 6.8. Similar to the undoped and Ba doped materials, the film widths exhibit a bimodal distribution, with the first peak around 0.52 nm and a second peak around 1.33 nm. In the uncrept grip section, the data show a Gaussian distribution with a mean value of 0.72 ± 0.13 nm (Figure 5.13). Therefore, the results indicate that viscous flow also occurs during tensile creep of multiphase ceramics such as Y_2O_3 doped material. The film thickness distribution in this material was obtained by the Fresnel fringe imaging technique. High-resolution lattice

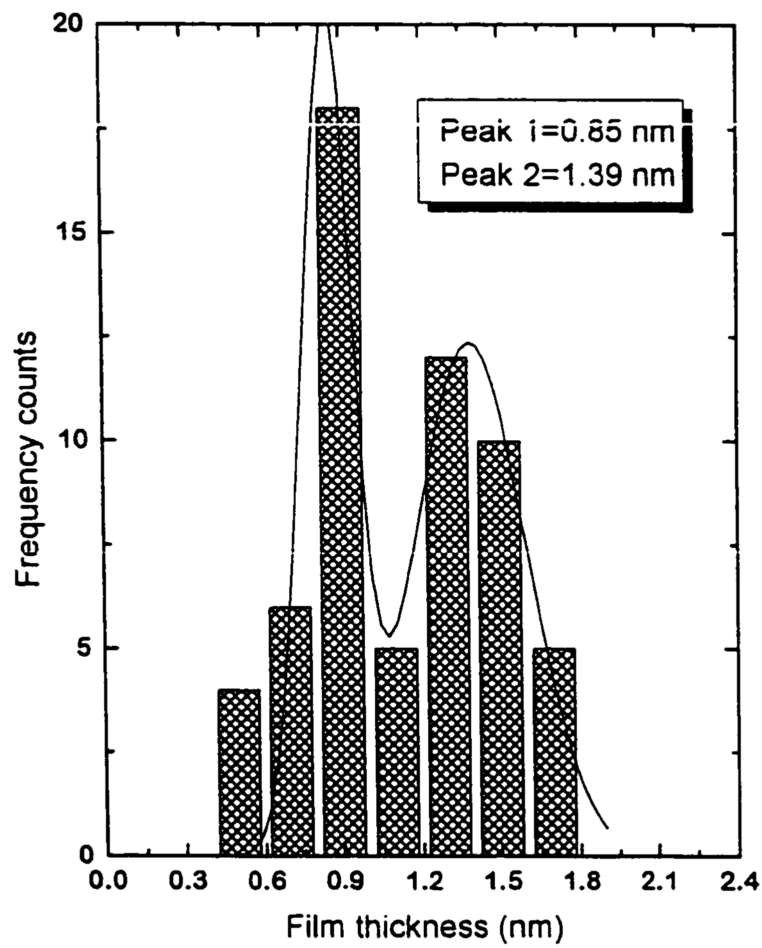

(a)

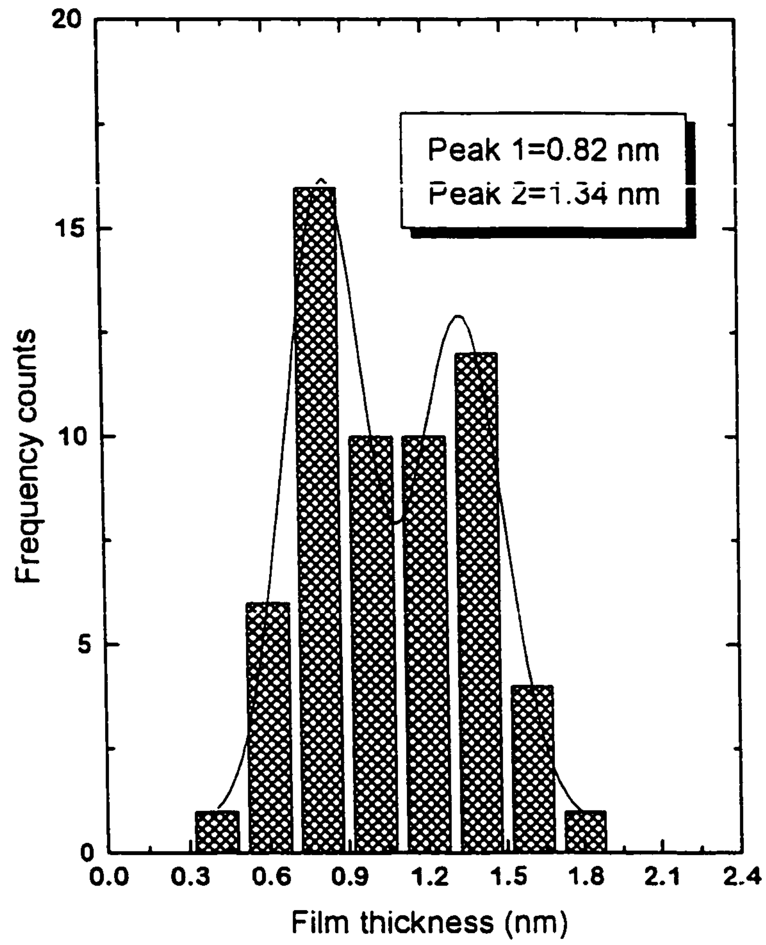

(b)

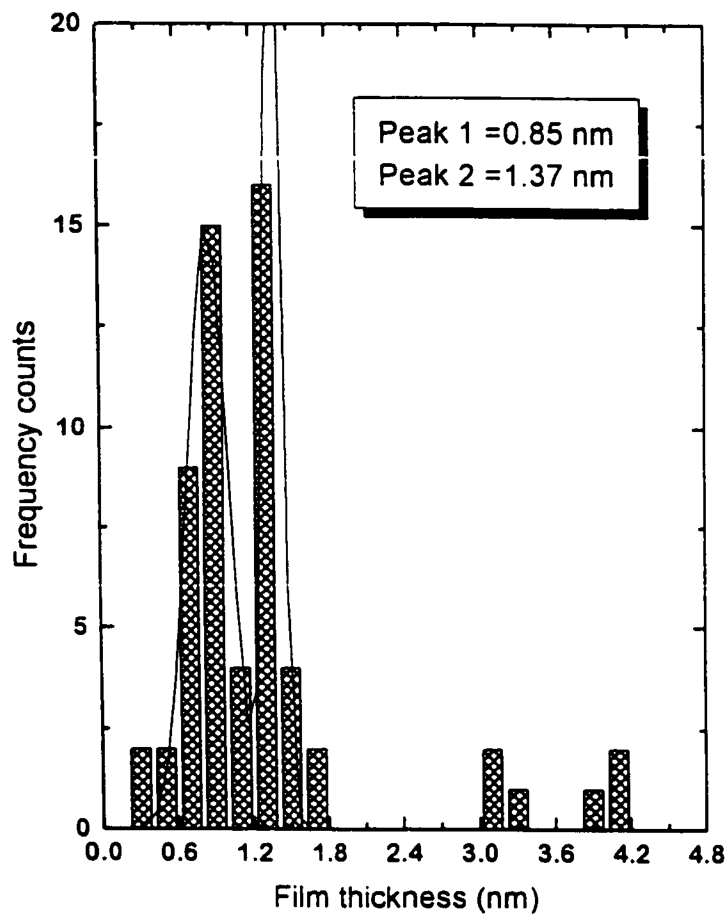

(c)

Figure 6.6 Film thickness distribution in the Ba doped material after creep for different times; (a) 7h (ε=0.0049) ; (b) 40h (ε=0.0104); (3) 200h (ε=0.0307).

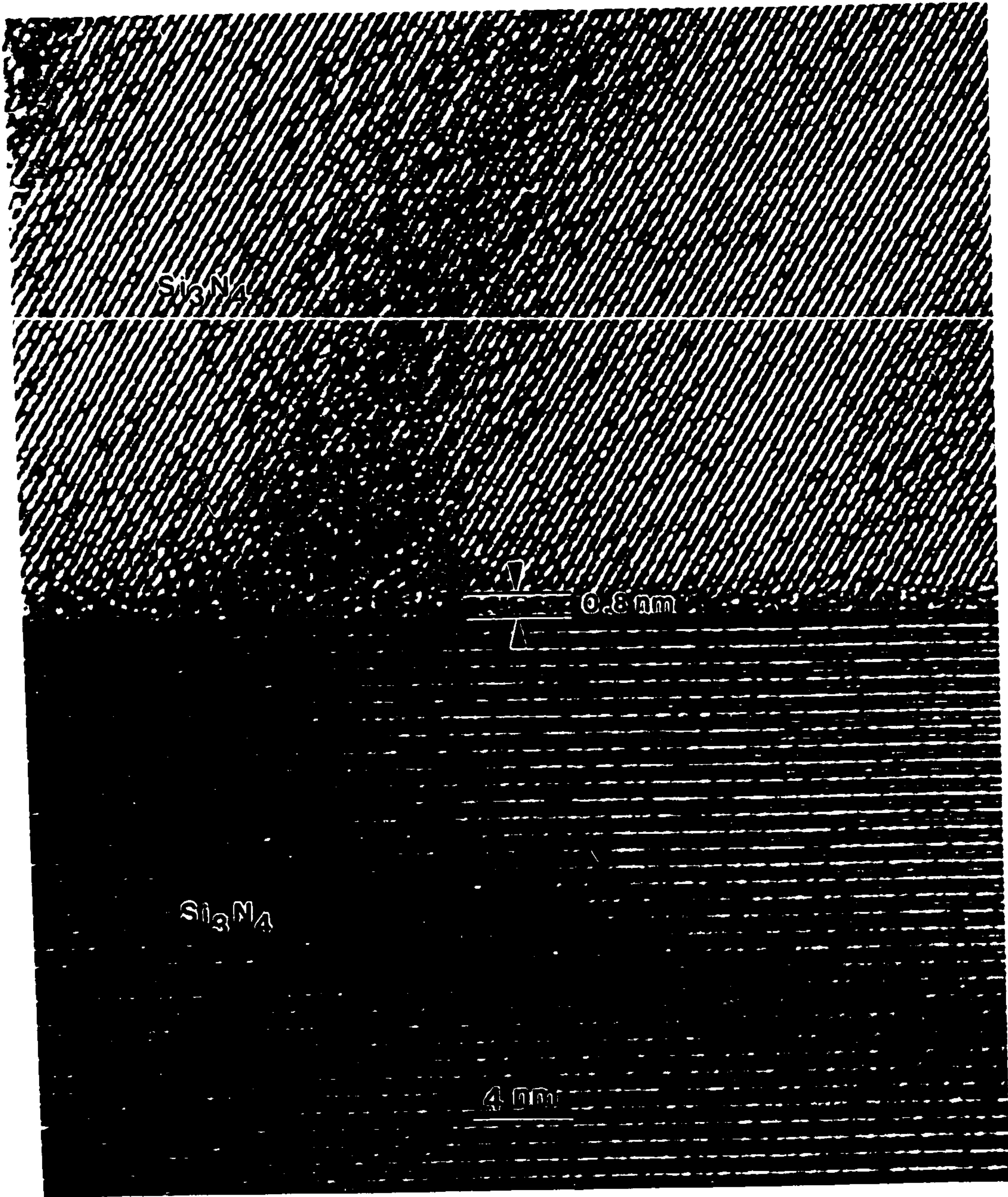

(a)

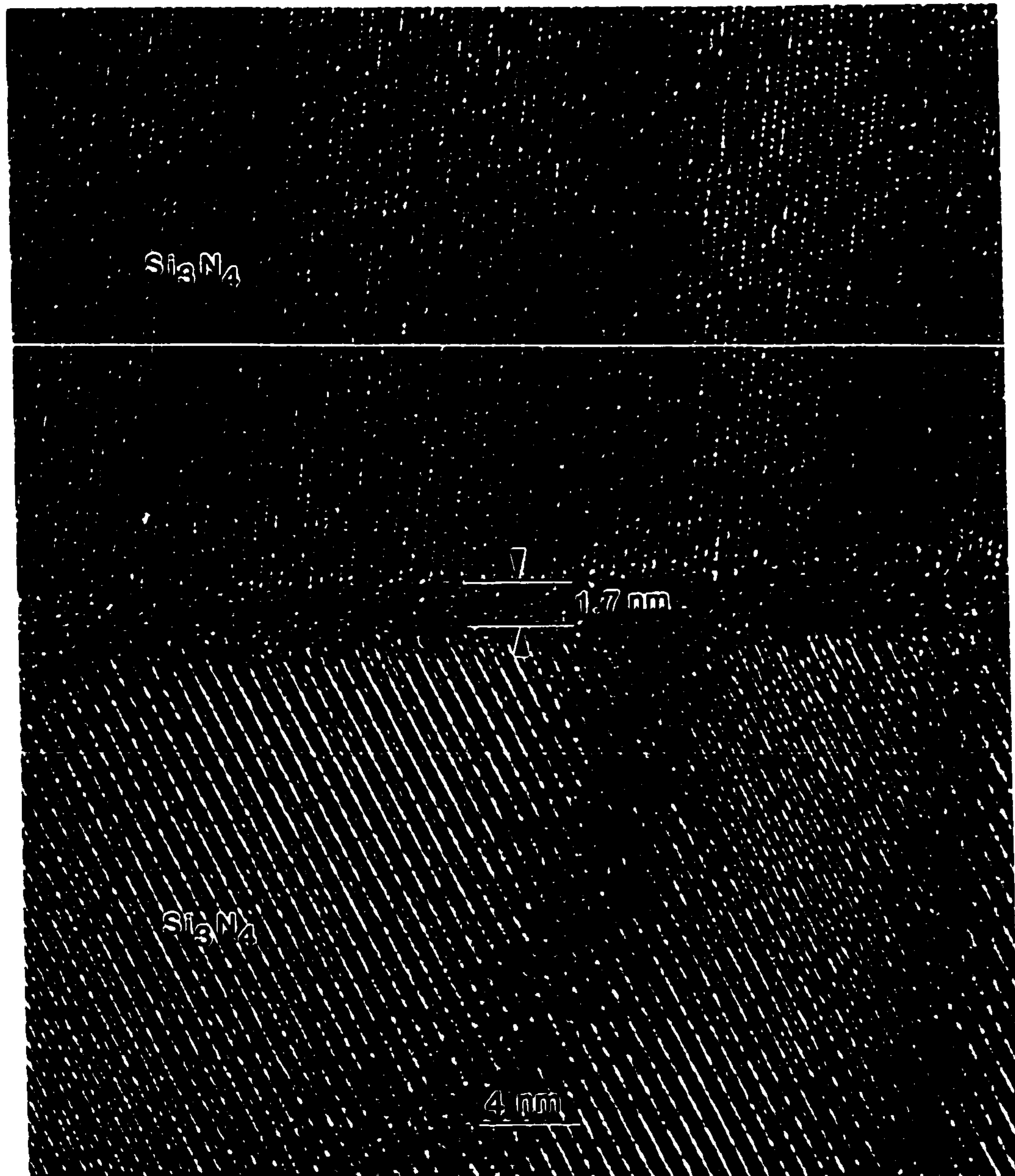

(b)

Figure 6.7 High-resolution lattice fringe images of grain boundary films in the Ba doped material crept under 100MPa for 40h, showing (a) a film thickness of 0.8 nm at one grain boundary, and (b) a film thickness of 1.7 nm at another grain boundary.

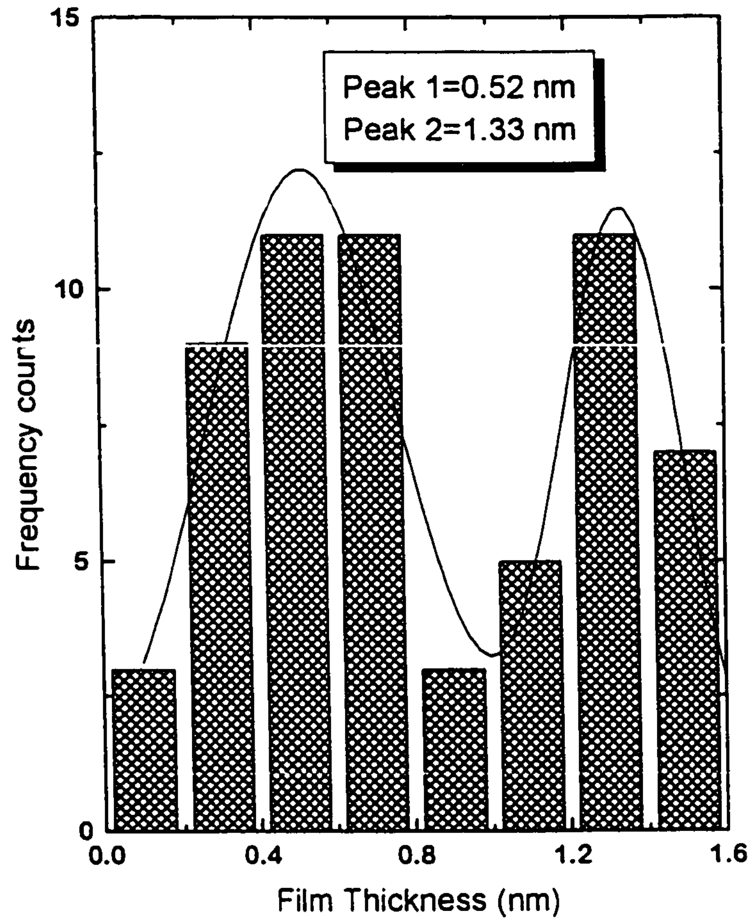

Figure 6.8 Histogram of film thickness distribution of homophase boundaries of the Y_2O_3 doped material crept at 1430°C under 40MPa for 690h, showing a bimodal distribution with the first peak at 0.52 nm and a second peak at 1.33 nm.

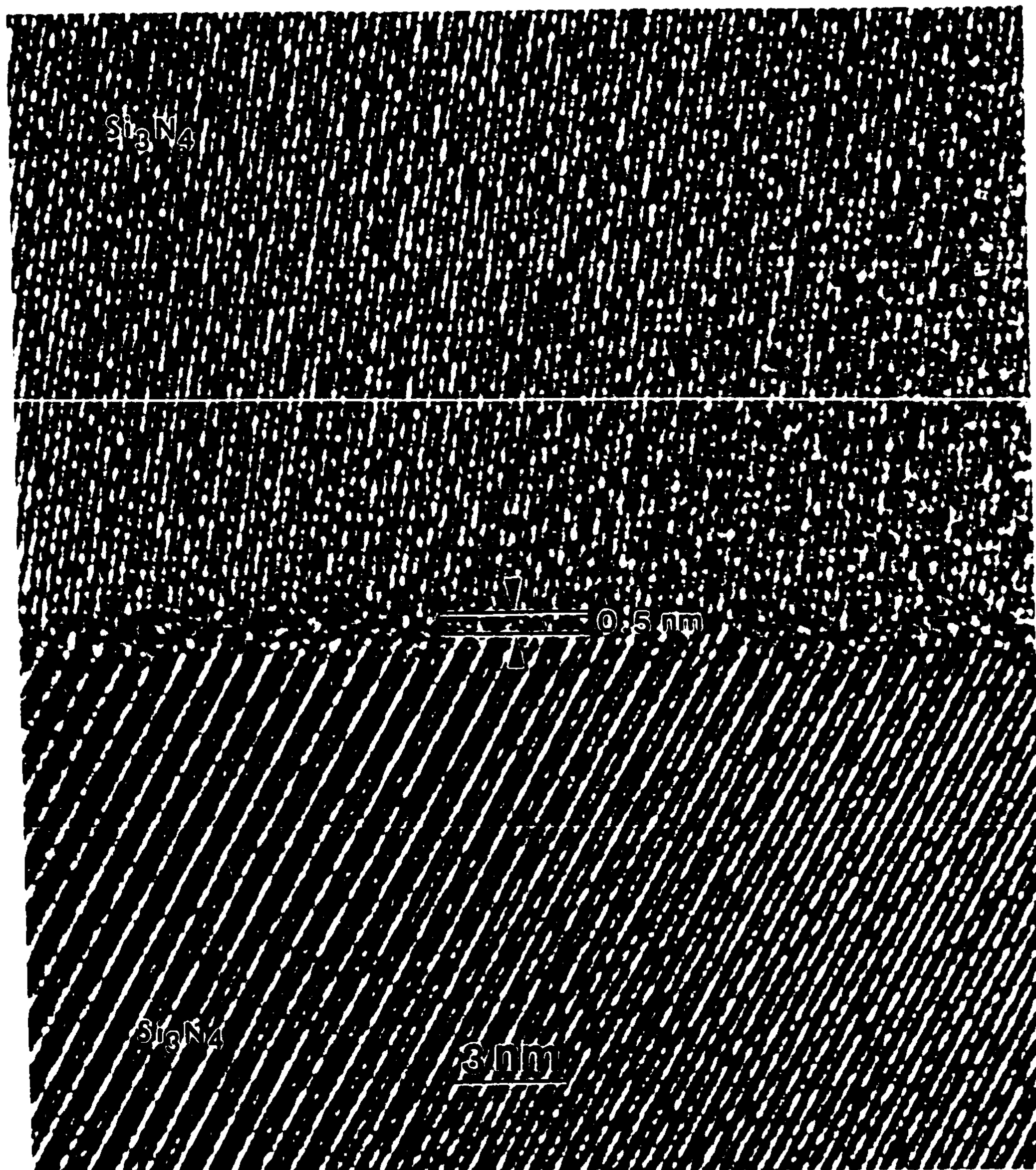

(a)

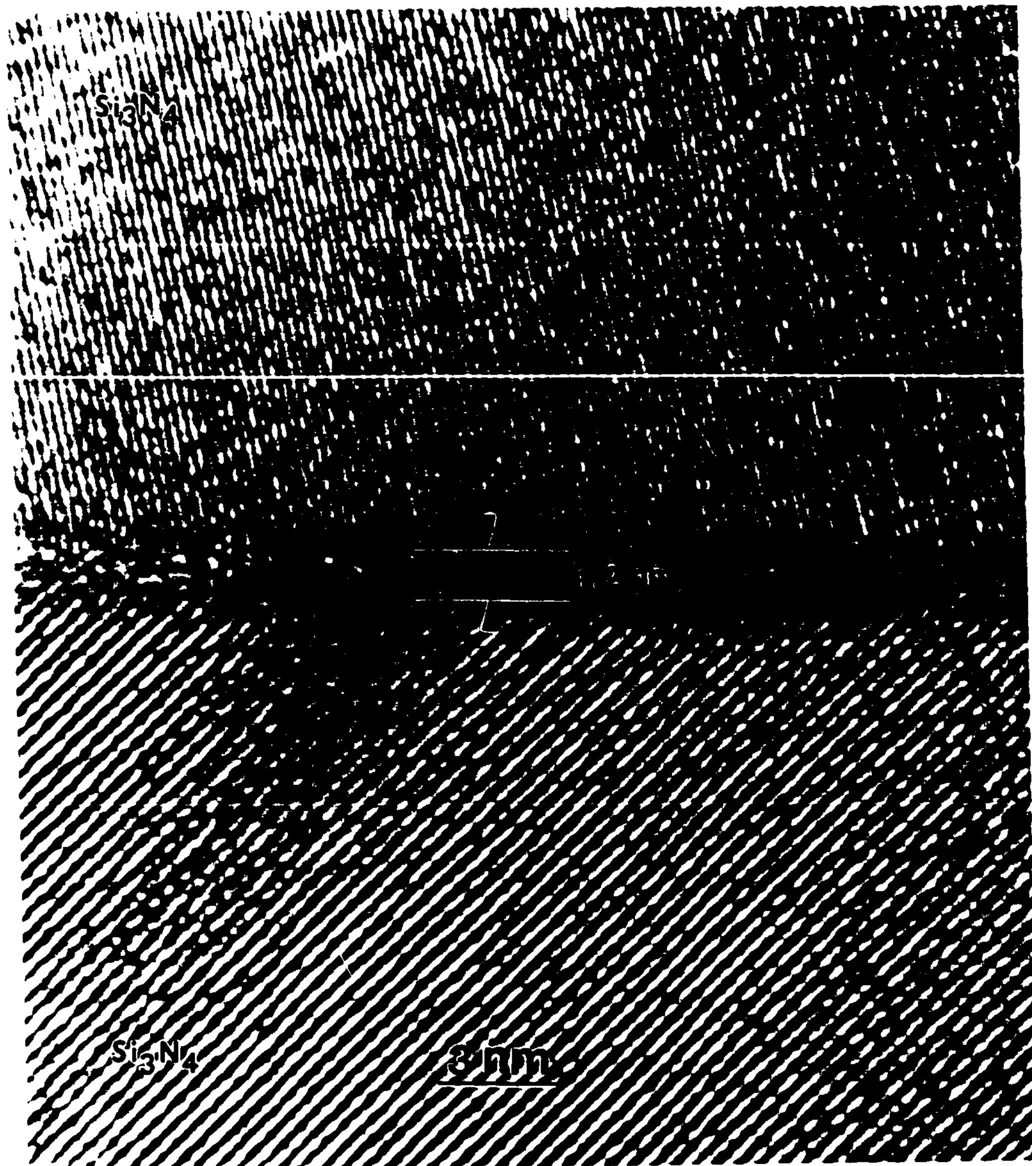

(b)

Figure 6.9 High-resolution lattice images of homophase boundary films in the gauge section of the Y_2O_3 doped Si_3N_4 sample crept under 40MPa for 690h, showing (a) a film thickness of 0.5 nm at one grain boundary, and (b) a film thickness of 1.2 nm at another grain boundary.

images of a number of grain boundaries confirmed this result. Figure 6.9 shows a thinner film (0.5 nm) and a thicker film (1.2 nm) at the Si_3N_4/Si_3N_4 interface in the crept gauge section by using the HREM imaging technique. It should be noted that, due to the presence of secondary crystalline phases, EDS analysis was used to ensure that the amorphous film to be measured lay between two Si_3N_4 grains. A full statistical analysis of heterophase-boundary film widths before and after creep was not attempted in this work since three different secondary crystalline phases result in three different heterophase boundaries. However, high-resolution lattice imaging of a number of the heterophase boundaries indicated that no significant change in the range of heterophase-boundary widths could be detected before and after creep.

6.2.3 Other Microstructural Features Caused by Creep

Viscous flow may accompany the creep deformation during the second creep stage, thus causing different film thickness distributions at different strains. A clear understanding of the creep mechanism of the second creep stage is important to evaluate the film thickness distribution during the creep process. In general, the stress exponent for creep and microstructural evolution are used to investigate the creep mechanisms. Previous investigations (Jin 1995, Luecke et al 1995) indicate that dissolution-reprecipitation and cavitation control the second creep stage of the undoped and the Y_2O_3 doped material, respectively. In this work, the film thickness distribution at different strains was measured in the Ba doped material. Therefore, the discussion of microstructural evolution and redistribution of the grain-boundary phase is focused on the Ba doped material. An

important observation in the crept sample of this material is cavitation induced by the creep process. Figure 6.10 shows cavities at multigrain junctions after creep at 100MPa for 200h. Since the as-received material contained a certain volume fraction of pre-existing cavities (5%) at multigrain junctions, and cavities can also be produced by ion-milling of TEM samples, it is hard to distinguish the cavities (as shown in Figure 6.10a) produced during creep from the pre-existing cavities and those caused by ion-milling. Nevertheless, in the crept specimen of the Ba doped material, multiple lens-shaped cavities separated by ligaments were occasionally observed, as shown in Figure 6.10b. Such cavities were never observed in the uncrept materials or in the crept samples of the undoped material under the same testing conditions. We believe these cavities were produced during creep and are not artifacts of sample preparation.

In addition to observations of cavities at multigrain junctions, strain whorls were also observed at grain boundaries of this material, as shown in Figure 6.11. Considering that there were no such features in the undoped material crept under the same testing conditions and in the uncrept materials, it is believed that the strain whorls are manifestations of a localized residual stress produced during creep.

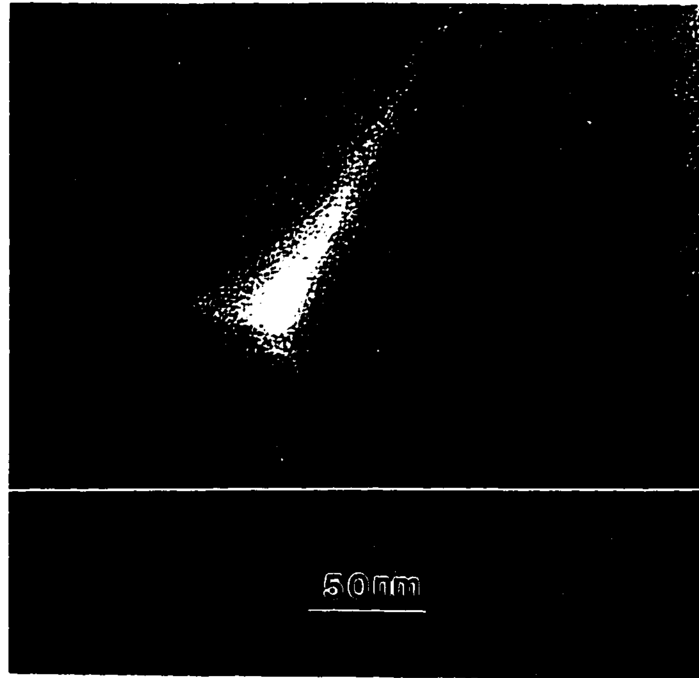

(a)

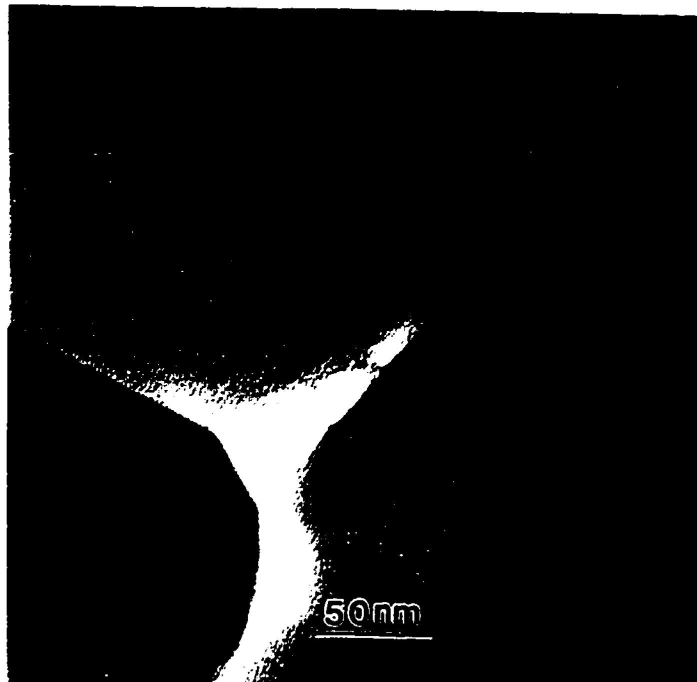

(b)

Figure 6.10 Cavitation at multigrain junctions in the Ba doped material after creep at 1400°C, 100MPa for 200h; (a) single spherical cavity, (b) multiple lens-shaped cavities separated by ligaments.

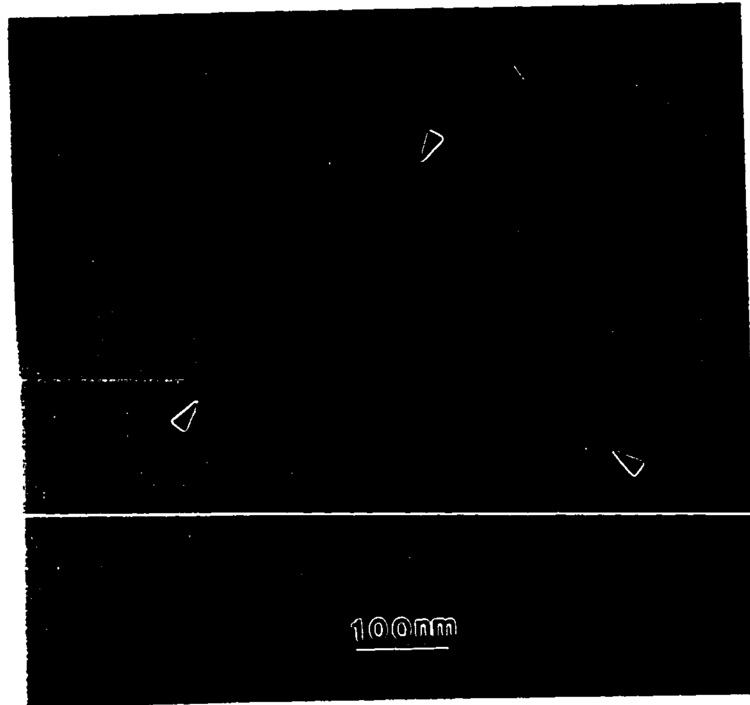

Figure 6.11 Strain whorls observed at two-grain boundaries in the Ba doped material after creep at 1400°C, 100MPa for 200h.

6.3 Discussion

The creep response of the experimental materials is similar, all exhibiting two distinct creep stages. The strain rate remains relatively constant at low strains, whose values (ε =1~4 × 10^{-3}) depend on the stress level, the state of stress and the grade of material. Once the strain reaches a critical value, the strain rate then decreases by up to one order of magnitude. The creep rate approaches an apparent steady state at high strains, although a truly constant strain rate is never achieved. The difference of about one order of magnitude in strain rate between the two stages suggests that more than one creep mechanism operates. A similar kind of creep response has been observed in a number of

silicon nitride ceramics (Chadwick et al 1993, Wilkinson 1994). The first (or low-strain) stage of creep, also termed "exhaustion creep" (Wilkinson 1994), has been postulated as due to the viscous flow mechanism. In the present investigation, the statistical data of the grain boundary film thickness before and after creep (Figures 5.8, 5.9, 5.12 and Figures 6.4, 6.6, 6.8) obtained mainly by the HREM technique indicate that a significant redistribution of the intergranular glass phase accompanies creep. A schematic diagram showing the redistribution of intergranular films due to viscous flow is given in Figure 6.12. Based on the experimental results, the widths of intergranular films are assumed to be constant at all the grain boundaries before creep (Figure 6.12a). After creep, however, the boundaries perpendicular to the compressive stress axis (perpendicular boundaries) become thinner and those lying at an angle to the stress axis (angle boundaries) become thicker (Figure 6.12b). Since the grain boundaries examined were randomly selected, a bimodal distribution of intergranular film widths were observed. This, together with our previous investigation (Jin 1995), provides convincing evidence for the viscous flow mechanism.

Previous models can be used to predict the creep response of the undoped and Ba doped materials. However, they have difficulties for the Y_2O_3 doped material. In order to undersatnd the viscous flow process in multiphase ceramics such as Y_2O_3 doped material, a new model has to be developed. Comparison of experimental observations with the model will be discussed in Chapter 7.

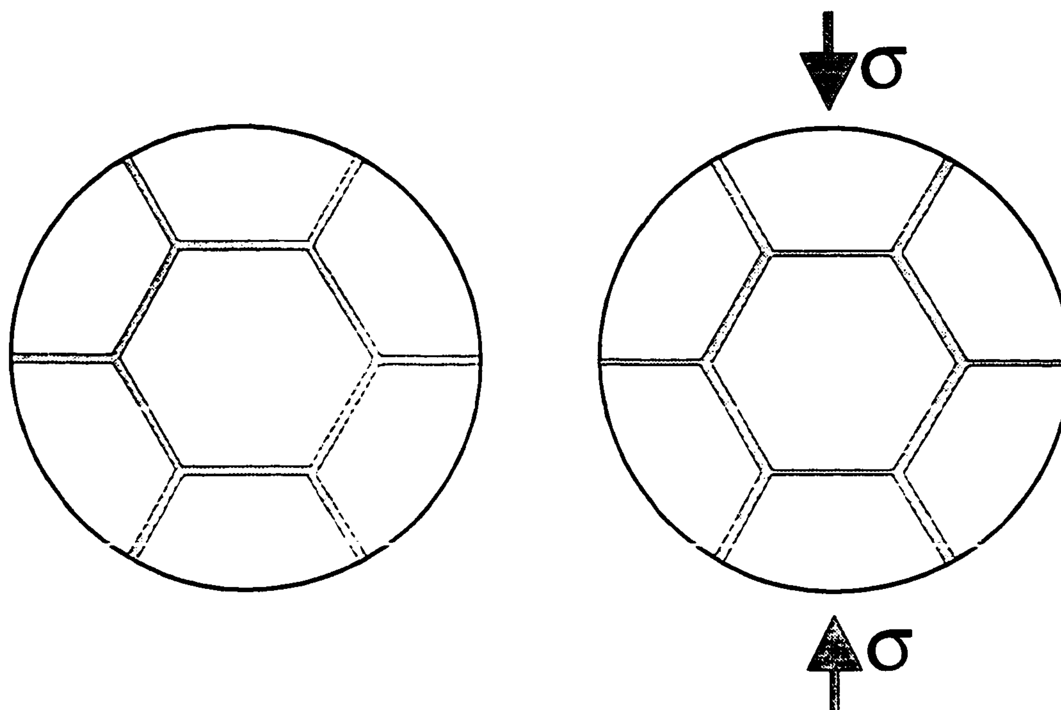

Figure 6.12 Schematic diagram of the grain-boundary film thickness distribution in a glass-containing ceramic; (1) uniform film thickness in the as-sintered state, (b) bimodal distribution of the film widths under a compressive load.

The second (or high-strain) stage of creep is generally ascribed to dissolution/reprecipitation or cavitation processes (Lange et al 1980a, Wiederhorn et al 1993). For the undoped material, which does not cavitate, dissolution-reprecipitation is thought to dominate second stage of creep (Jin 1995). The experimental support for this hypothesis is a stress exponent of about one. As in the previous investigation on a Ba doped material (Jin 1995), the current work on the Ba doped material suggests that grain-boundary sliding accommodated by cavitation dominates the second stage of creep. Firstly, the stress exponent of about 2 rules out the possiblity of simple diffusional creep. Secondly, direct observations of lens-shaped cavities at multigrain junctions (Figure

6.10b), suggest that creep occurs by a cavity-related process. A large number of strain whorls at grain boundaries due to grain-to-grain contact indicate that the growth of cavities is caused by grain boundary sliding. The creep mechanisms of the Y_2O_3 doped material has been investigated by Luecke et al (1995). Extensive cavitation at both two-grain boundaries and triple junctions suggests that cavitation contributes substantially to creep of this material.

The film thickness distributions at different strains strongly suggest that the viscous flow process mainly occurs during the first stage of creep. The average thickness values of the compressive grain boundaries and tensile grain boundaries, which correspond respectively to the positions of the two peaks in a bimodal distribution, were essentially unchanged with strain over the range of conditions used in this study. After a long time of creep (200h), some very thick grain boundaries were observed in the crept sample. This is probably associated with cavitation at multigrain junctions. Assuming the intergranular phase is incompressible, the excess viscous phase displaced by cavity formation must be squeezed into two adjacent grain boundaries under tension, thus causing an increase in film thickness at this grain boundary. A theoretical analysis of cavity growth and its effect on grain boundary film thickness is given in Appendix A. It is predicted that only grain boundaries under tension are expected to have a significant increase in their film thickness. A cavity of 30 nm in diameter could increase the boundary film under tension from 1 nm to 3 nm (see Figure A5). Figure 6.13a is the LFI image of a thick grain boundary observed in the sample crept for 200h. A lower magnification (Figure 6.13b) micrograph

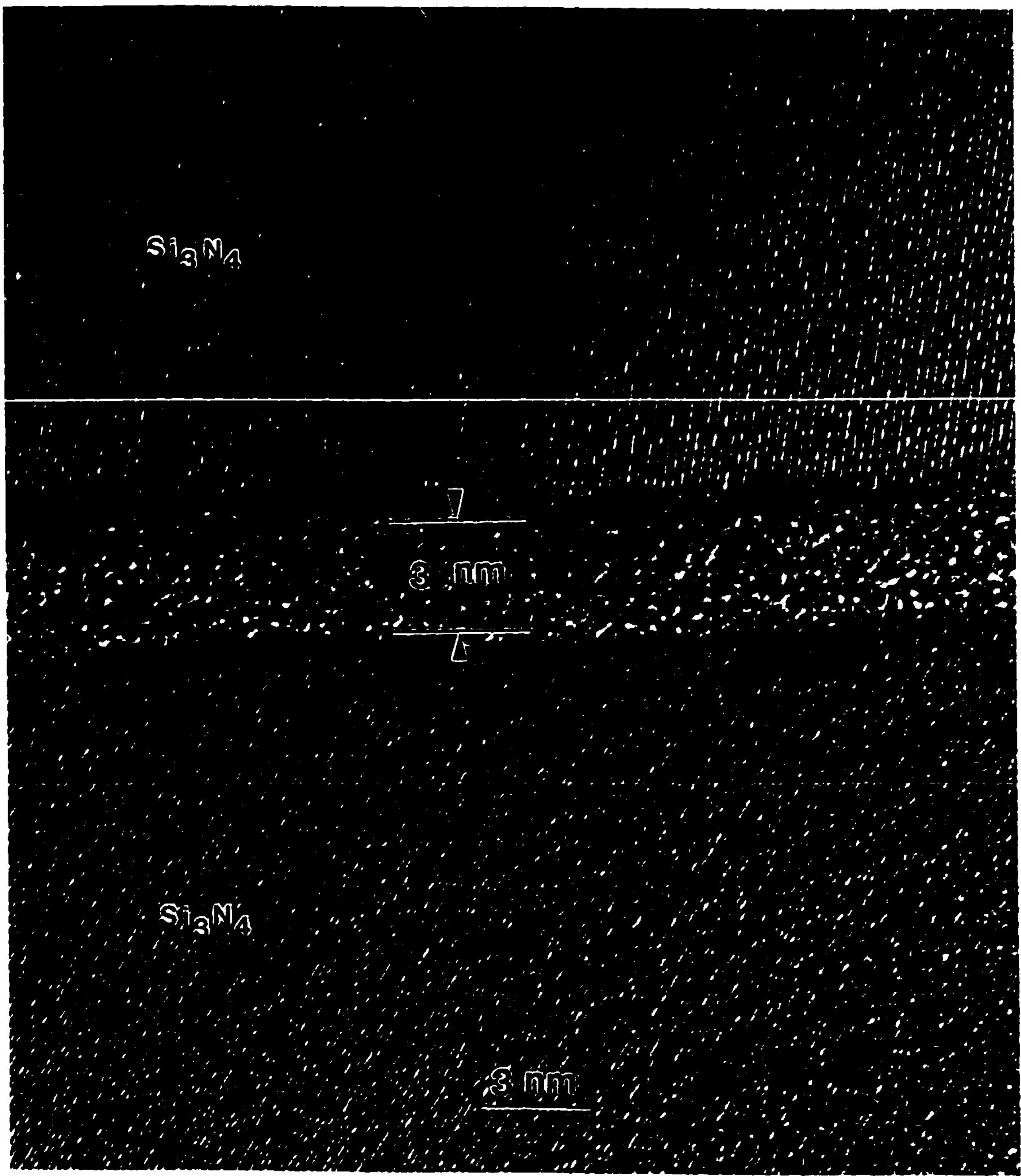

(a)

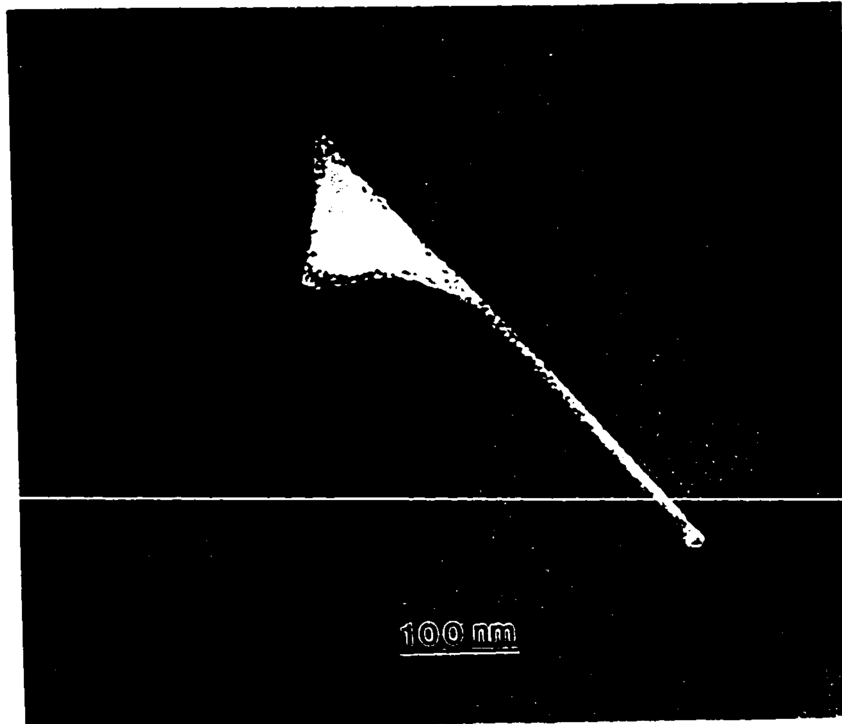

(b)

Figure 6.13 (a) High-resolution lattice image of a thick grain boundary film in the Ba doped material crept at 1400°C, 100MPa for 200h, (b) lower magnification of the grain boundary, showing it is connected to a triple junction cavity.

indicates that this boundary interconnects to a triple junction cavity. This reflects how cavity formation influences the grain boundary film thickness. Since cavitation only occurs at the multigrain junctions which are highly stressed and its influence on the grain boundary film thickness is highly localized, statistically, therefore, most grain boundaries are not influenced by cavitation. The measured film thickness distributions at different strain values can be reasonably explained.

6.4 Summary

In this work, the creep behaviour of the experimental materials was investigated. All the materials exhibited two creep stages which differ in strain rate by up to one order of magnitude, regardless of the grade of material (Si_3N_4 with or without secondary crystalline phases), stress state (tensile or compressive) and stress level (from 40 to 200MPa). The grain-boundary film widths have been measured mainly by using high-resolution transmission electron microscopy. It was found that while the film widths were confined to a narrow range before creep, a bimodal distribution of the film widths were usually found after creep. This indicates that the grain-boundary amorphous phase redistributes after creep. Moreover, no significant difference was found in the film thickness distributions measured at different strains. This suggests that viscous flow mainly occurs during the first stage of creep although cavitation in the second stage of creep may cause local film thickness thickening.

Chapter 7

VISCOUS FLOW CREEP OF SILICON NITRIDE

Part II Modeling and Discussion

7.1 Introduction

The experimental observations of the creep response and the film thickness distribution before and after creep have been discussed in the last chapter. It is concluded that viscous flow indeed occurs during creep deformation of the experimental materials. Theoretical modeling is now required to understand the viscous flow process and predict the creep response caused by this process.

Models for creep by viscous flow have generally focused on the effect of a small amount of amorphous grain boundary phase on the creep behaviour of glass-containing ceramics such as Si_3N_4 (Wilkinson 1998). In these models, the creep strain is determined by changes in the local separation between the crystalline grains through viscous flow of the amorphous films from grain boundaries in compression to those in tension, while the crystalline grains remain rigid. Based on the assumption of either square (Lange 1975, Pharr et al 1983) or hexagonal grains (Drucker 1964, Dryden et al 1989, Chadwick et al 1992), several two-dimensional models have been developed to describe this process. The treatment of hexagonal grains is more realistic, and was first proposed by Drucker (1964), who calculated the average strain rate as a function of stress, viscosity and volume fraction of the amorphous phase. Dryden et al (1989) extended Drucker's model to include the strain dependence of the creep rate. The creep response was predicted to be a nearly

constant strain rate at low strains followed by a rapid decrease in strain rate as the limiting strain is approached. The limiting strain occurs when essentially all of the fluid is squeezed out from grain boundaries under compression. Three-dimensional models (Dryden et al 1997a, 1997b) have also been developed which are generally consistent with the two-dimensional models.

The pre-existing viscous flow models have their limitations. They assumed that the grain size and the initial grain boundary thickness were uniform throughout the material. In polycrystalline material, however, a large range of grain size distribution is usually observed. In addition, the microstructure may contain secondary crystalline phases. Since degradation of mechanical properties occurs at temperatures above 1000°C owing to the softening of the residual amorphous phase (Sanders et al 1985, Hirosaki et al 1988), much attention has been paid to different heat-treatments and additives used to crystallize the amorphous phase at multigrain junctions (Pierce et al 1986, Bonnell et al 1987, Cinibulk et al 1990, Falk et al 1992). However, complete crystallization of these junctions cannot be attained as a residual glass film always remains along matrix/secondary phase two grain boundaries. High-resolution electron microscopy investigations (Kleebe et al 1992, Vetrano et al 1993), together with the current work (see Chapter 5), have shown that the film widths of "heterophase boundaries" (between matrix and SP grains) are in general larger than those of "homophase boundaries" (between matrix grains). The strain rate derived in Dryden et al's model (1989) depends on $(2\delta_0 / \sqrt{3}L)^3$ as well as strain, where $2\delta_0$ is the initial grain-boundary film thickness and 2L is the grain facet length. It is evident that a variation in either the grain size or grain-boundary film thickness will change the

strain rate due to viscous flow. In a microstructure with a local variation in volume fraction of the grain-boundary amorphous phase, generation of internal stresses and a redistribution of the local stresses are required for compatible deformation. The effect of grain size distribution on the viscous flow process has been analyzed recently by Dey et al (1997). They argued that the presence of large grains can cause very high local stress concentrations, about 15~30 times the applied stress, depending on the volume fraction and size of the large grains.

It is apparent that the pre-existing models cannot be used to describe the viscous flow process in multiphase ceramics such as the Y_2O_3 doped material. In this chapter, therefore, the viscous flow model is extended to materials containing secondary crystalline phase grains by assuming a bimodal distribution of grain-boundary film widths. The influence of the volume fraction of the secondary phase and thickness of heterophase boundaries on the creep response is discussed. Since microstructural heterogeneity may also cause very high local stresses and result in cavitation, another point of interest is to analyze the distribution of local stresses during viscous flow. Finally, the experimental observations discussed in Chapter 6 are compared with the results predicted by viscous flow models.

7.2 Viscous Flow Model for Multiphase Ceramics

7.2.1 General Considerations

The thickness of homophase-boundary amorphous films in Si_3N_4 ceramics has been measured for a variety of additive compositions (Kleebe et al 1993a, 1993b, Chapter 5).

They are found to have a characteristic value in each ceramic and vary in the range of 0.5 to 2 nm, depending on the composition but not on the volume fraction of the amorphous phase. Although more experimental work is required, the widths of heterophase boundaries have been found to be 1-3 nm larger than those of homophase boundaries (Kleebe et al 1992, Vetrona et al 1993, Chapter 5). Experimental observations indicate that the secondary phase grains tend to be randomly distributed in the microstructure (see Figure 5.6). Since a limited amount of sintering aids is added during ceramic processing, the resulting secondary phase grains are usually separated by the matrix grains. In this model, it is thus assumed that the material consists of a periodic array of two-dimensional hexagonal grains of the same facet length (2L) with a bimodal distribution of the grain-boundary film widths. While the initial film thickness of homophase boundaries is denoted $2\delta_0$, the film thickness of heterophase boundaries is $2m\delta_0$, i.e., larger by some factor m. In addition, the secondary phase grains are not adjacent to each other. Thus the largest possible volume fraction of the secondary phase that can be treated in this model is 0.33, as shown in Figure 7.1a. The dark grains in the figure represent the secondary crystalline phase.

Suppose the material is loaded uniaxially with a far field applied stress, $\sigma^{\infty}=\sigma_{11}$. The normal stress in the other direction (σ_{22}) and the shear stresses ($\sigma_{12}=\sigma_{21}$) are all zero. Based on mechanical equilibrium, the relation between the local stresses and the applied stress is given by

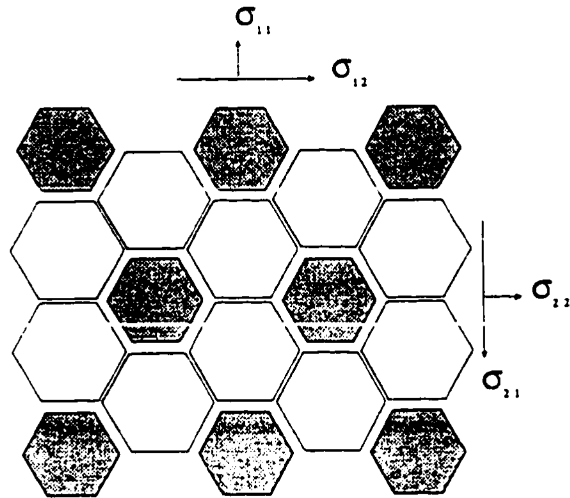

(a)

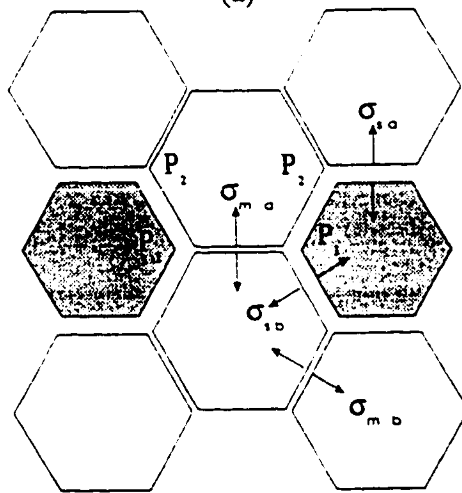

(b)

Figure 7.1 (a) Simplified microstructure of Si_3N_4 containing 1/3 of SP grains, (b) The pressures in the multigrain junctions and the average normal stresses acting on the different boundaries.

$$\sigma_{mb} + 2\sigma_{sb} = 0 \tag{7.1}$$

$$\sigma_{ma} + \sigma_{sb} = \sigma_{sa} + \sigma_{mb} \tag{7.2}$$

$$\sigma_{ma} + \sigma_{sa} + \sigma_{sb} = 3\sigma^{\infty} \tag{7.3}$$

where σ_{ij} (i=m, s; j=a, b) indicates the average stresses acting on the four types of different boundaries (Figure 7.1b). The subscripts m and s denote homophase and heterophase boundaries respectively; the subscript a refers to boundaries which are perpendicular to the stress axis, while b refers to boundaries making an angle of ±30° with respect to the stress axis.

7.2.2 Strain Rate and Local Stress Calculation

We now consider viscous flow of the boundary phase. It is further assumed that (i) the boundary amorphous phase behaves like a Newtonian viscous fluid, (ii) no cavitation occurs during creep, and (iii) the deformation is uniform throughout the microstructure.

The rate of separation of two parallel plates ($\dot{\delta}$) separated by a Newtonian viscous fluid, and with nonzero pressures P_1 and P_2 at the ends of the plates, is calculated in Appendix A. The result is

$$\dot{\delta} = \frac{(\bar{\sigma} - \frac{P_1 + P_2}{2})\delta^3}{\eta L^2} \tag{7.4}$$

where $\bar{\sigma}$ is the average stress acting on the plates, 2L is the length of the plates, η and 2δ are the viscosity and current thickness of the fluid layer, respectively.

Following the analysis by Dryden et al (1989) and applying equation (7.4) to a hexagonal array of grains, the constitutive equations for flow at perpendicular homophase and heterophase boundaries are found to be

$$\dot{\varepsilon}_{ma} = \frac{3}{8\eta}\left(\frac{2\delta_0}{\sqrt{3}L}\right)^3 (1+2\zeta)^3(\sigma_{ma} - P_1) \tag{7.5}$$

$$\dot{\varepsilon}_{sa} = \frac{3}{8\eta}\left(\frac{2\delta_0}{\sqrt{3}L}\right)^3 (m+2\zeta)^3(\sigma_{sa} - P_2) \tag{7.6}$$

where $\dot{\varepsilon}_{ij} = \dot{\delta}_{ij} / \sqrt{3}L$ (i=m, s; j=a, b) is the strain rate *in the direction of the stress axis*. Compatibility of deformation throughout the material requires that $\dot{\varepsilon}_{ma} = \dot{\varepsilon}_{sa} = \dot{\varepsilon}$ and also that $\varepsilon_{ma} = \varepsilon_{sa} = \varepsilon$, where ε is the overall strain of the material in the direction of the stress axis. The relation between the overall strain (ε) and boundary layer thickness change ($\Delta\delta$) is expressed as $\varepsilon = \Delta\delta / \sqrt{3}L$ (Dryden et al 1989). ζ is defined as the normalized strain and is equal to $\varepsilon\sqrt{3}L / 2\delta_0$. P_1 and P_2 are respectively the pressures at the ends of a perpendicular homophase and heterophase boundary, see Figure 7.1b. It is worth noting that the rate of film thickness change at angle boundaries is half that at

perpendicular boundaries since the shear strain rate is zero (for further details see Dryden et al 1989). Thus, the flow rate at the 30° homophase and heterophase boundaries can be expressed as

$$\dot{\varepsilon} = \frac{3}{8\eta}\left(\frac{2\delta_0}{\sqrt{3}L}\right)^3 (1-\zeta)^3(2P_2 - 2\sigma_{mb}) \tag{7.7}$$

$$\dot{\varepsilon} = \frac{3}{8\eta}\left(\frac{2\delta_0}{\sqrt{3}L}\right)^3 (m-\zeta)^3(P_1 + P_2 - 2\sigma_{sb}) \tag{7.8}$$

Using equations (7.1) - (7.8), the strain rate can be calculated as

$$\dot{\varepsilon} = \frac{3}{8\eta}\left(\frac{2\delta_0}{\sqrt{3}L}\right)^3 S(\zeta)\sigma^{*} \tag{7.9}$$

where $S(\zeta) = \dfrac{9}{4(m+2\zeta)^{-3} + 2(1+2\zeta)^{-3} + 2(m-\zeta)^{-3} + (1-\zeta)^{-3}}$

The average normal stress acting on the four different types of boundaries σ_{ij}(i=m, s; j=a, b) is given by

$$\sigma_{ma} = \frac{-\left[\left(\frac{m+2\zeta}{1+2\zeta}\right)^3 - 2\left(\frac{1-\zeta}{m-\zeta}\right)^3 + 1\right]\frac{S(\zeta)\sigma^{*}}{(1-\zeta)^3} + \frac{3}{2}\sigma^{*}\left[5\left(\frac{m+2\zeta}{1+2\zeta}\right)^3 + 4\right]}{3\left[\left(\frac{m+2\zeta}{1+2\zeta}\right)^3 + 2\right]} \tag{7.10}$$

$$\sigma_{mb} = \frac{-\left[\left(\frac{m+2\zeta}{1+2\zeta}\right)^3 - 2\left(\frac{1-\zeta}{m-\zeta}\right)^3 + 1\right]\frac{S(\zeta)\sigma^*}{(1-\zeta)^3} + 3\sigma^*\left[\left(\frac{m+2\zeta}{1+2\zeta}\right)^3 - 1\right]}{3\left[\left(\frac{m+2\zeta}{1+2\zeta}\right)^3 + 2\right]} \tag{7.11}$$

$$\sigma_{mm} = \frac{\left[\left(\frac{m+2\zeta}{1+2\zeta}\right)^3 - 2\left(\frac{1-\zeta}{m-\zeta}\right)^3 + 1\right]\frac{S(\zeta)\sigma^*}{2(1-\zeta)^3} + \frac{3}{2}\sigma^*\left[2\left(\frac{m+2\zeta}{1+2\zeta}\right)^3 + 7\right]}{3\left[\left(\frac{m+2\zeta}{1+2\zeta}\right)^3 + 2\right]} \tag{7.12}$$

$$\sigma_{ab} = \frac{\left[\left(\frac{m+2\zeta}{1+2\zeta}\right)^3 - 2\left(\frac{1-\zeta}{m-\zeta}\right)^3 + 1\right]\frac{S(\zeta)\sigma^*}{2(1-\zeta)^3} - \frac{3}{2}\sigma^*\left[\left(\frac{m+2\zeta}{1+2\zeta}\right)^3 - 1\right]}{3\left[\left(\frac{m+2\zeta}{1+2\zeta}\right)^3 + 2\right]} \tag{7.13}$$

Similarly, the pressures at the ends of a homophase and heterophase boundary are calculated as

$$P_1 = \frac{\left[\left(\frac{m+2\zeta}{1+2\zeta}\right)^3 + 4\left(\frac{1-\zeta}{m-\zeta}\right)^3 - 2 + 6\left(\frac{1-\zeta}{m-\zeta}\right)^3\left(\frac{m+2\zeta}{1+2\zeta}\right)^3\right]\frac{S(\zeta)\sigma^*}{2(1-\zeta)^3} - 6\sigma^*\left[\left(\frac{m+2\zeta}{1+2\zeta}\right)^3 - 1\right]}{3\left[\left(\frac{m+2\zeta}{1+2\zeta}\right)^3 + 2\right]} \tag{7.14}$$

$$P_2 = \frac{\left[\left(\frac{m+2\zeta}{1+2\zeta}\right)^3 + 4\left(\frac{1-\zeta}{m-\zeta}\right)^3 + 4\right]\frac{S(\zeta)\sigma^*}{2(1-\zeta)^3} + 3\sigma^*\left[\left(\frac{m+2\zeta}{1+2\zeta}\right)^3 - 1\right]}{3\left[\left(\frac{m+2\zeta}{1+2\zeta}\right)^3 + 2\right]} \tag{7.15}$$

Equations (7.9)-(7.15) relate the strain rate and local stresses to the far-field applied load σ^{∞} and microstructural parameter m when the material contains the largest possible volume fraction of secondary crystalline phases for the idealized geometry of Figure 7.1a. These equations reduce to the same results derived in the previous model (Dryden et al 1989) for uniform grain-boundary film thickness when m=1.

7.2.3 Ceramics Containing an Arbitrary Volume Fraction of SP Grains

In a polycrystalline material, the volume fraction Φ of the secondary phase grains is determined by the composition of the starting powders and the processing parameters. To evaluate the viscous flow creep of ceramics containing an arbitrary volume fraction of secondary crystalline phases, the method used by Dey et al (1997) is employed, i.e., the material is assumed to consist of two types of regions. Region I is occupied by matrix grains only whereas region II contains 33% of secondary phase grains.

The local strain rate in region II ($\dot{\varepsilon}_2$) is given by equation (7.9). If m=1, the strain rate in region I ($\dot{\varepsilon}_1$) can also be obtained from this expression, leading to

$$\dot{\varepsilon}_1 = \frac{3\sigma_1}{8\eta}\left(\frac{2\delta_0}{\sqrt{3}L}\right)^3 \frac{3}{2(1+2\zeta)^{-3}+(1-\zeta)^{-3}} \tag{7.16}$$

$$\dot{\varepsilon}_2 = \frac{3\sigma_2}{8\eta}\left(\frac{2\delta_0}{\sqrt{3}L}\right)^3 S(\zeta) \tag{7.17}$$

σ_1 and σ_2 are the local stresses in the two regions defined by the condition of mechanical equilibrium, i.e.,

$$(1-3\Phi)\sigma_1 + 3\Phi\sigma_2 = \sigma^{\infty} \tag{7.18}$$

Compatibility between these two regions suggests that

$$\dot{\varepsilon}_1 = \dot{\varepsilon}_2 = \dot{\varepsilon} \tag{7.19}$$

Using equations (7.16) - (7.19), the local stresses in the two regions (σ_1 and σ_2) and the strain rate ($\dot{\varepsilon}$) can be expressed as

$$\sigma_1 = \frac{\sigma^{\infty} S(\zeta)[2(1+2\zeta)^{-3} + (1-\zeta)^{-3}]}{9\Phi + (1-3\Phi)S(\zeta)\left[2(1+2\zeta)^{-3} + (1-\zeta)^{-3}\right]} \tag{7.20}$$

$$\sigma_2 = \frac{\sigma^{\infty}}{3\Phi + (\frac{1}{3} - \Phi)S(\zeta)\left[2(1+2\zeta)^{-3} + (1-\zeta)^{-3}\right]} \tag{7.21}$$

$$\dot{\varepsilon} = \frac{3\sigma^{\infty}}{8\eta}\left(\frac{2\delta_0}{\sqrt{3}L}\right)^3 S'(\zeta) \qquad \text{where} \tag{7.22}$$

$$S'(\zeta) = \frac{S(\zeta)}{3\Phi + (\frac{1}{3} - \Phi)S(\zeta)\left[2(1+2\zeta)^{-3} + (1-\zeta)^{-3}\right]} \tag{7.23}$$

Now in region II, the average stress along the four different boundaries σ_{ij} (i=m, s; j=a,b) and the triple junction pressures P_1 and P_2 are still given by equations (7.10)-(7.15), but with σ^{∞} replaced by σ_2.

7.2.4 Effect of Microstructure

(1) Creep response

Equation (7.22) represents the dependence of creep rate on boundary layer thickness ratio (m) and volume fraction of secondary phase grains (Φ). In Figures 7.2 and 7.3, the creep response in both tension and compression is illustrated by the nondimensional strain rate term $S'(\zeta)$ versus the normalized strain (ζ), either for different values of m with a constant value of Φ, or for different values of Φ with a constant value of m. It should be noted that all the results for the strain rate and local stresses calculated above are also applicable to compressive creep with ζ replaced by $-\zeta$. As shown in Figures 7.2 and 7.3, a similar creep response is obtained with (i.e., m>1) or without (i.e., m=1) the secondary crystalline phase, such that the initial creep rate is relatively constant followed by a rapid decrease in creep rate when the maximum strain is approached. The maximum value of the normalized strain (ζ) due to viscous flow is 1 in tension and 0.5 in compression (Dryden et al 1989). In tension, the maximum strain is reached when all the amorphous phase in homophase boundaries lying at 30° to the tensile axis is squeezed out while some still remains in the equivalent heterophase boundaries since m>1. In compression, the maximum strain corresponds to the situation in which all the amorphous

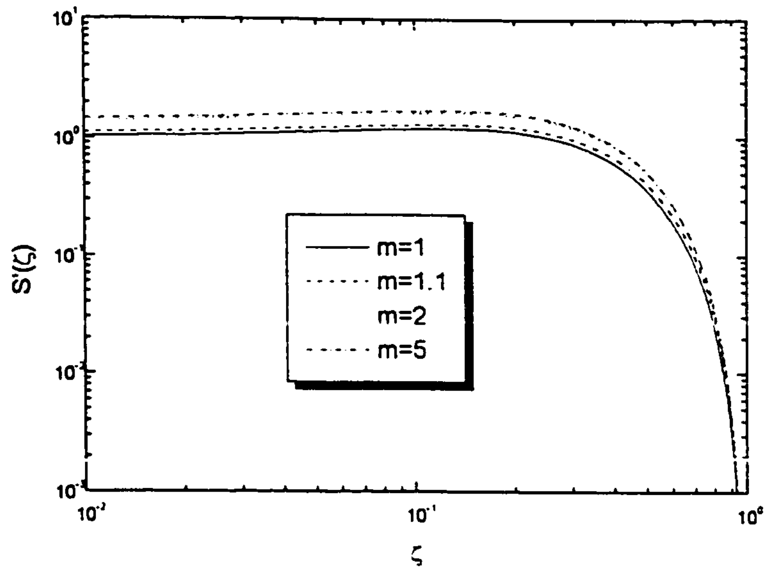

(a)

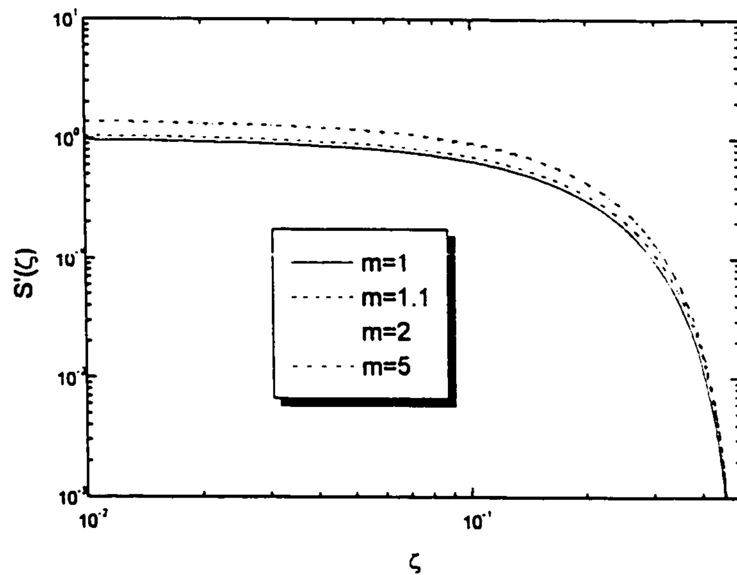

(b)

Figure 7.2 Non-dimensional strain rate term S'(ζ) as a function of the normalized strain ζ for different values of m with a constant value of Φ=0.15: (a) tensile creep; (b) compressive creep.

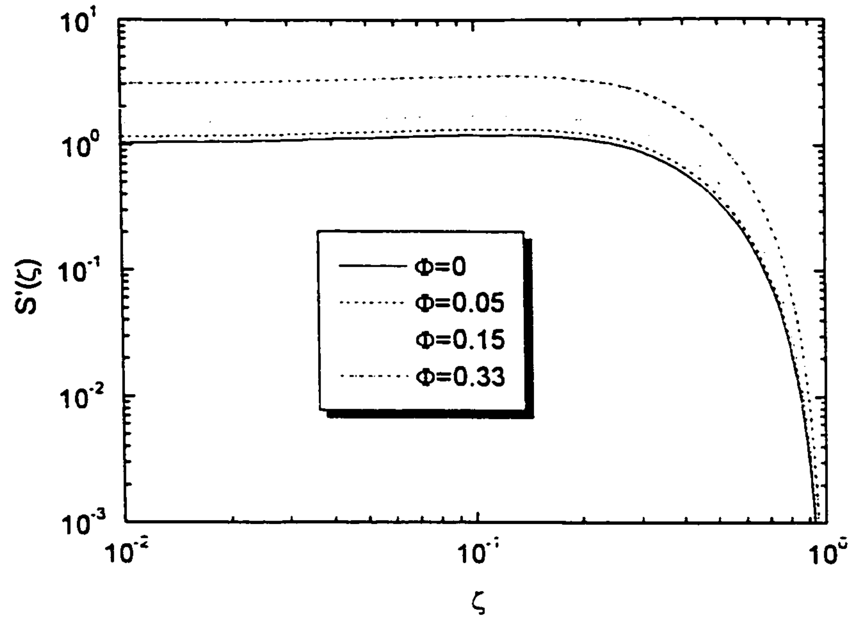

(a)

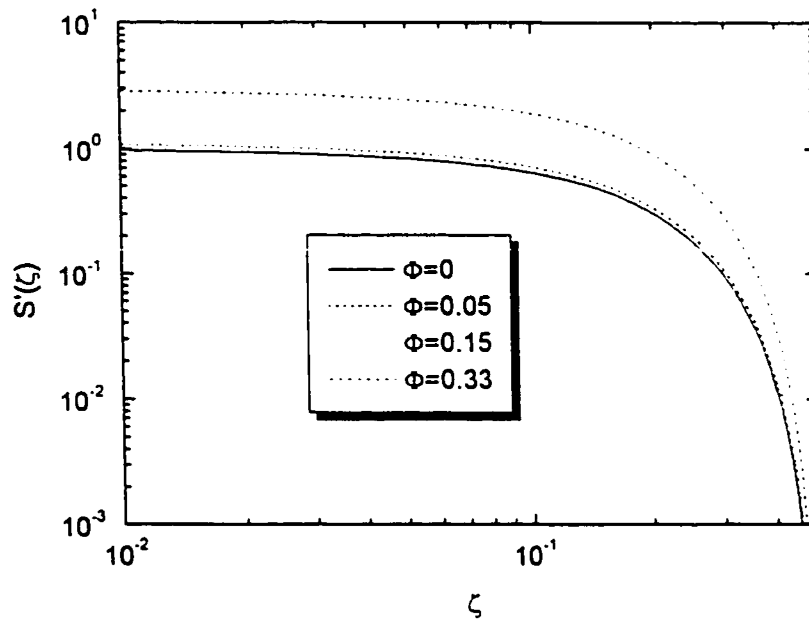

(b)

Figure 7.3 Nondimensional strain rate term $S'(\zeta)$ as a function of the normalized strain ζ for different values of Φ with a constant value of m=5, (a) tensile creep; (b) compressive creep.

phase in the homophase boundaries at 90° to the stress axis is squeezed out from between grains. Similarly, some amorphous phase is still left in the heterophase boundaries. Obviously, the presence of the secondary crystalline phase enhances the viscous flow process in both tensile and compressive creep. As m or Φ increases, the greater is the strain rate. For example, when Φ=0.33 and m is around 5, the largest strain rate is three times as fast as that without secondary crystalline phases.

(2) Stress in local regions

The effect of volume fraction of the secondary phases on local stress in the two regions is shown in Figure 7.4 by using equations (7.20) and (7.21). The stress in both regions increases with the volume fraction of secondary phases and does not change much during the viscous flow process. A small amount of secondary crystalline phases does not cause a stress concentration in region I. The maximum stress in this region is three times the applied stress when the volume fraction of secondary crystalline phases approaches 0.33. This implies that the overall strain rate is dominated by the region which has the larger volume fraction.

(3) Triple junction pressures and normal stress on boundaries

The normal stress along a grain boundary and the pressure in a triple junction have been analyzed by Dryden et al (1989) for materials with a uniform boundary layer thickness. Due to the presence of secondary crystalline phase grains, the internal stress distribution is changed. Equations (7.10)-(7.15) are used to plot the triple junction pressures and the

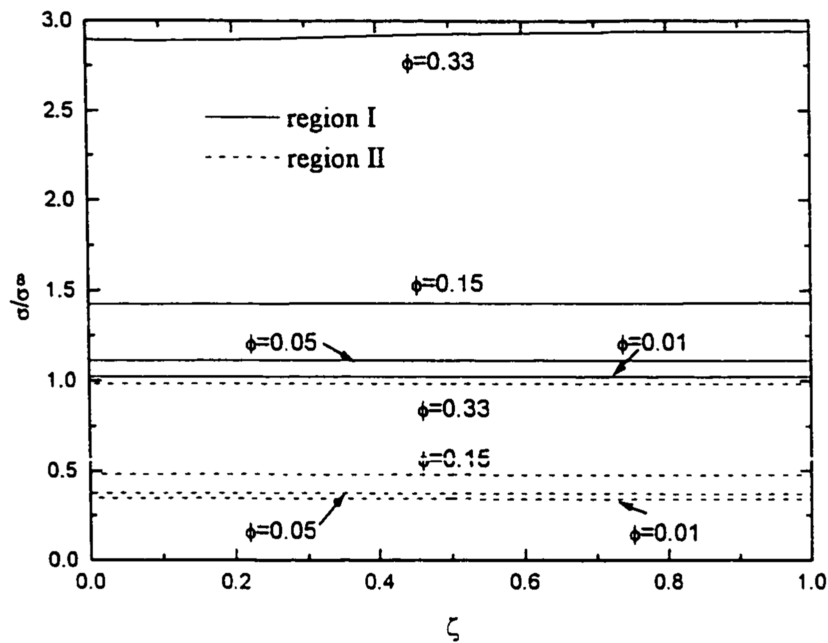

Figure 7.4 Stresses in the local regions vary with the volume fraction of SP grains for a compatible deformation (m=5).

stresses along grain boundaries against the normalized strain for different values of m. The stress and pressure are normalized by the applied stress and the results are shown in Figures 7.5-7.6. For a certain value of m, the stress acting on a perpendicular homophase boundary (Figure 7.5a) is different from that on a heterophase boundary (Figure 7.5b). While the latter increases as viscous flow continues, the former decreases. The pressure at the ends of both boundaries is always lower than the average stress acting on the boundary at the begining of the creep process. However, the difference between them decreases with strain and they become equal at the maximum strain (ζ=1 in tension). The highest stress concentration occurs at a perpendicular heterophase boundary and the largest

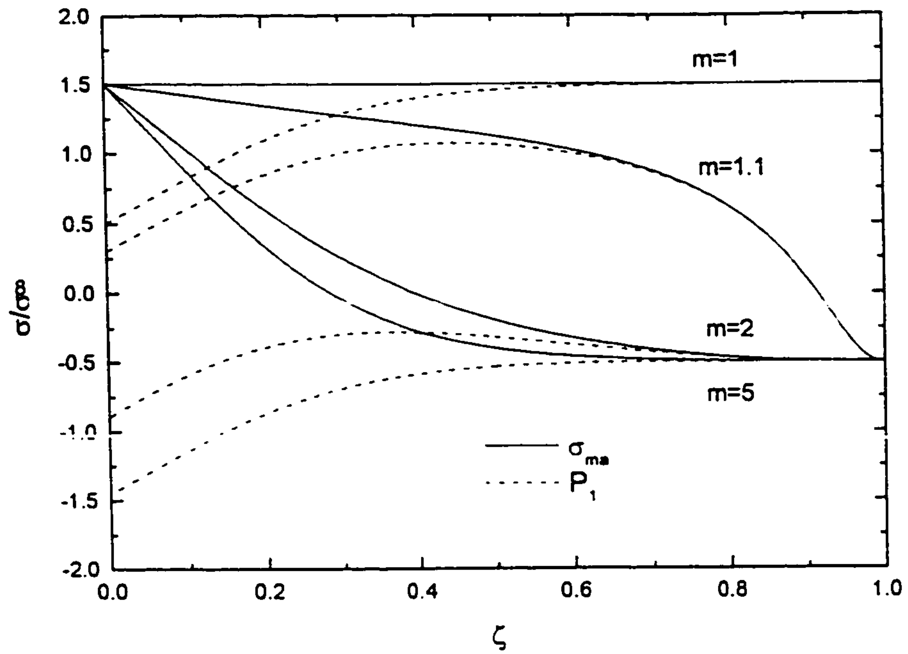

(a)

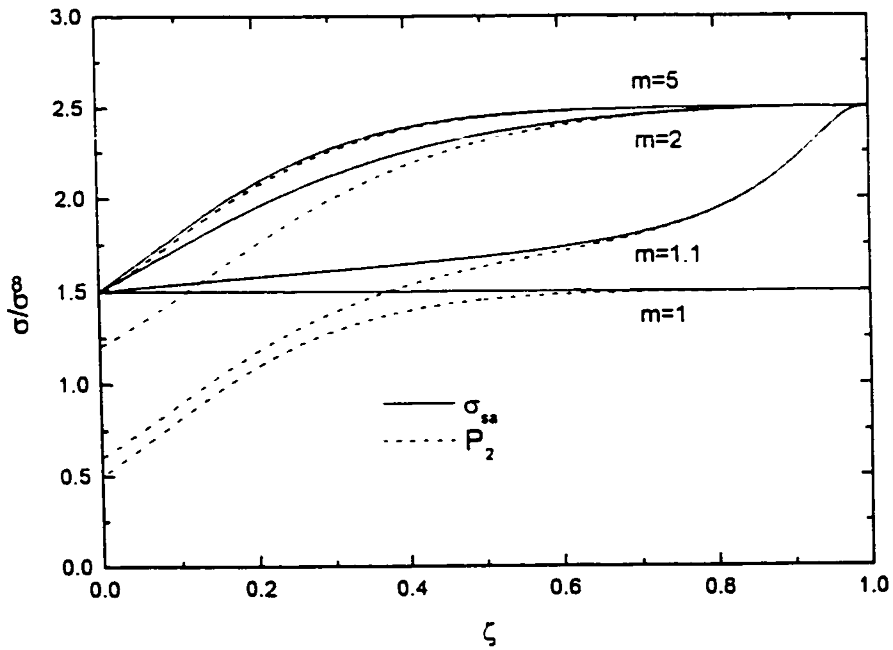

(b)

Figure 7.5 Average normal stresses on perpendicular boundaries and pressures at their ends as a function of the normalized strain for different values of m with $\Phi=1/3$, (a) homophase boundaries; (b) heterophase boundaries.

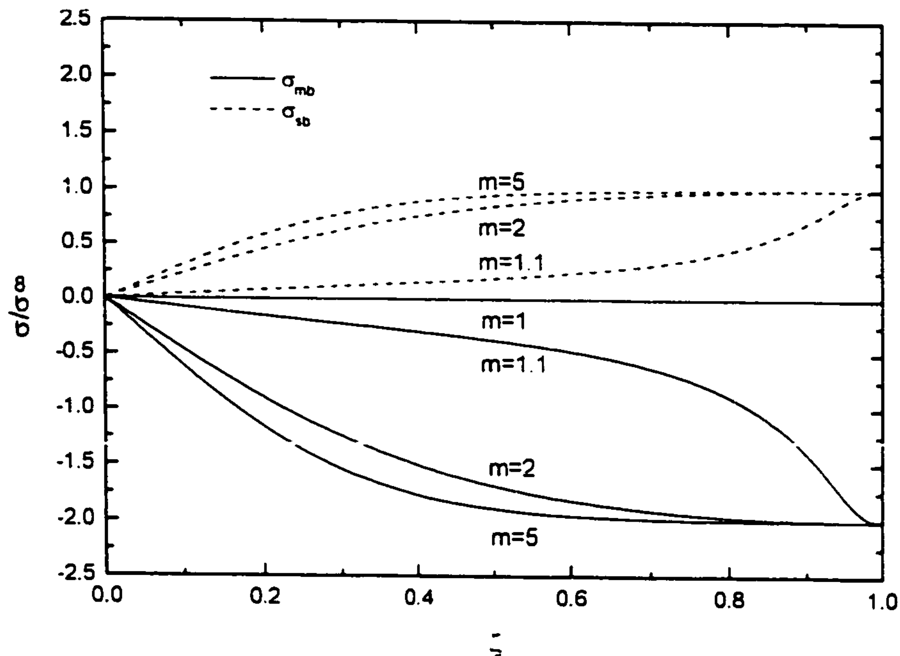

Figure 7.6 Average normal stresses on angle homophase and heterophase boundaries as a function of the normalized strain for different values of m with $\Phi=1/3$.

pressure build-up due to viscous flow is at the triple junction adjoining such a boundary. However, the value is only $2.5\sigma^{\infty}$. If m=1 (i.e., a material without secondary phase grains), the stress acting on the perpendicular boundaries remains constant during the creep deformation and is equal to $1.5\sigma^{\infty}$. A large value of m accelerates the rate at which the stress or pressure increases to reach its maximum value for both homophase and heterophase boundaries. In order to achieve uniform deformation in materials containing a bimodal distribution of the boundary film thickness, a nonzero average stress is produced at the 30° boundaries, as shown in Figure 7.6. This stress is zero when no secondary phase grains are present (Dryden et al 1989). The stress generated on these boundaries at the

end of creep deformation is $-2\sigma^{\infty}$ for a homophase boundary and σ^{∞} for a heterophase boundary.

7.3 Discussion

We now compare the experimental data with the predictions of the model. The constitutive equation for the strain rate (Equation 7.22) requires a knowledge of the microstructural parameters, m and Φ, and the viscosity η. In case of the undoped and the Ba doped materials, the film thickness ratio (m) equals 1 and/or the volume fraction of the secondary crystalline phases (Φ) equals zero. For the Y_2O_3 doped material, the film thickness ratio m is about 5 and the volume fraction of secondary crystalline phase grains is 10%. The value of the viscosity of the boundary amorphous phase is not accurately known for any of the materials. However, the nondimensional strain rate $S'(\zeta)$ vs normalized strain ζ can be compared with the strain rate-strain curves measured experimentally. The theoretical data show an initial constant strain rate followed by a rapid decrease in strain rate as the strain approaches a limiting value (Figures 7.2 and 7.3). This "exhaustion creep" response seems to be independent of the stress state (compressive or tensile) and complexity of microstructure (with or without secondary crystalline phases). Now we understand that even in the Y_2O_3 doped material which contains several secondary crystalline phases, the creep response due to viscous flow is similar to that in the undoped and Ba doped materials which have no secondary crystalline phases. This is consistent with the experimental data (Figures 6.1-6.3). Without this modeling work, it

would be difficult to explain the creep behaviour of multiphase ceramics such as the Y_2O_3 doped material.

The limiting value of strain predicted by the model is $2\delta_0 / \sqrt{3}L$, assuming all the glass phase at the compressive homophase boundaries is squeezed out from between the grains. In reality, the viscous flow process may stop earlier when a new equilibrium thickness distribution is established according to the local normal stress acting on each grain boundary facet (Clarke 1987). Therefore, the maximum strain due to viscous flow can be estimated as the ratio of film thickness change at the perpendicular homophase boundaries to the grain size.

The film thickness change at the perpendicular boundaries can be estimated from the film thickness distribution before and after creep. We know that the film widths generally exhibit a bimodal distribution (two peaks) after creep. Depending on the stress state, the position of the first peak (compressive) or the second peak (tensile) is used as the average film thickness at perpendicular boundaries after creep. If we assume an average silicon nitride grain size to be about 0.25-0.5 μm (an approximate value given by microstructural examination), then the maximum strain due to viscous flow is expected to be in the range of 0.1-0.2%. Experimentally the drop in strain rate occurs at a strain of approximately 0.2-0.4%. These data are shown in Table 7.1. It should be noted that the assumptions made in the calculations are based on an "idealized" geometry. For example, the size of secondary crystalline phase grains are usually less than 0.5 μm. Furthermore, the film widths were measured at room temperature. It is not clear that the resulting observations are

representative of the grain-boundary structure of the material at the creep temperature. Clarke (1989) found that the high-temperature microstructure was significantly different from that of the material slowly cooled to room temperature. For example, the amorphous intergranular film in samples rapidly cooled to room temperature was much thicker (2~8 nm) than the thickness of ~ 1 nm found in the regularly cooled material. Given these uncertainties, we conclude that the limiting strain predicted by the viscous flow mechanism is in good agreement with the experimental results. This conclusion is similar to that reached before (Jin 1995).

The creep response predicted by the model is the nondimensional term $S'(\zeta)$ as a function of the normalized strain ζ due to the unknown viscosity of the amorphous phase. Direct comparison in strain rate-strain curves between the experimental data and theoretical prediction is also made for the undoped material. The amorphous phase in this material behaves like a non-Newtonian fluid with a stress exponent n=1.7 (Jin 1995). Viscous flow creep due to a non-Newtonian grain-boundary phase has been modeled by Chadwick et al (1992). For a two-dimensional array of hexagonal grains with a facet length of 2L separated by intergranular amorphous layer with an initial thickness of $2H_o$, the constitutive equation for the strain rate ($\dot{\varepsilon}$) is given by

$$\dot{\varepsilon} = C\Psi|\sigma|^n R(\varepsilon_N) \tag{7.24}$$

Ψ is a material constant ($\Psi=1/\eta$ when n=1, where η is the viscosity of the glass layer), $|\sigma|$ is the absolute value of the applied stress,

$$C = \frac{3^{(n+1)/2}}{2^{n+1}(n+2)}\left[\frac{2n+1}{2n}\right]^n f^{n+2}\text{, and} \tag{7.25}$$

$$R(\varepsilon_N) = 3^n \frac{(1+2\varepsilon_N)^{n+2}(1-\varepsilon_N)^{n+2}}{[(1+2\varepsilon_N)^{(n+2)/n} + 2^{1/n}(1-\varepsilon_N)^{(n+2)/n}]^n} \tag{7.26}$$

Here

$$f = \frac{2H_o}{\sqrt{3}L} \tag{7.27}$$

is the normalized glass layer thickness, and

$$\varepsilon_N = \frac{\varepsilon}{f} \tag{7.28}$$

is the normalized strain.

The material constant Ψ can be calculated from equations (7.24) to (7.28) by using the experimentally determined initial strain rate. Thus, the creep response predicted by the model can be compared directly with the experimental results, as shown in Figure 7.7. Considering the possible effect of temperature discussed earlier, two values of the initial film thickness (1 nm and 1.5 nm) were used in modeling, corresponding to Ψ being 1.808 $\times 10^{-12}$ and 3.974 $\times 10^{-13}$ $(Pa.s)^{-1}$ respectively. In either case, the creep response predicted by the model is in good agreement with the experiment, although a thickness value of 1.5 nm provides a better correspondence between model and experiment. The relationship between Ψ and η can be expressed as

$$\eta = \frac{\sigma^{(1-n)}}{n\Psi} \tag{7.29}$$

Using the aforementioned values of Ψ, the calculated viscosity of the intergranular film was found to be in the range of $0.5\sim5 \times 10^6$ Pa.s, corresponding to a stress range of 50 to 200 MPa used for the creep tests (Jin 1995). Mosher et al (1976) have measured the viscosity of the grain boundary phase in two different hot-pressed silicon nitride ceramics by using an internal friction technique. They found the values of viscosity per unit film thickness (η/δ) were $10^{16}\sim10^{17}$ Pa.s/m for temperatures in the range of 1100°C~1200°C. Extrapolation to 1400°C results in a viscosity of $10^5\sim10^6$ Pa.s for a 1 nm thick boundary. This suggests that the values of the material constant Ψ used here in modeling are reasonable.

Two plateaus of the strain rate were generally observed experimentally (Figures 6.1-6.3). The difference between the experimental data and theoretical predictions (as shown in Figure 7.7) is that creep continues at a much lower rate after the limiting strain at the end of the first plateau. This suggests that another mechanism is activated. The creep mechanisms which control the second stage of creep have been discussed in Chapter 6.

In the Y_2O_3 doped material, strains larger than 0.003 were observed with a concomitant reduction in strain rate (Figure 7.3). TEM observations and precise density measurements (Luecke et al 1995) indicate that cavities formed in the multigrain junctions contribute substantially to the tensile creep after the viscous flow regime. Small-angle X-ray scattering (SAXS) analysis of the crept material (Luecke et al 1995) suggests that cavity nucleation, rather than cavity growth, dominates the cavitation process. For a spherical

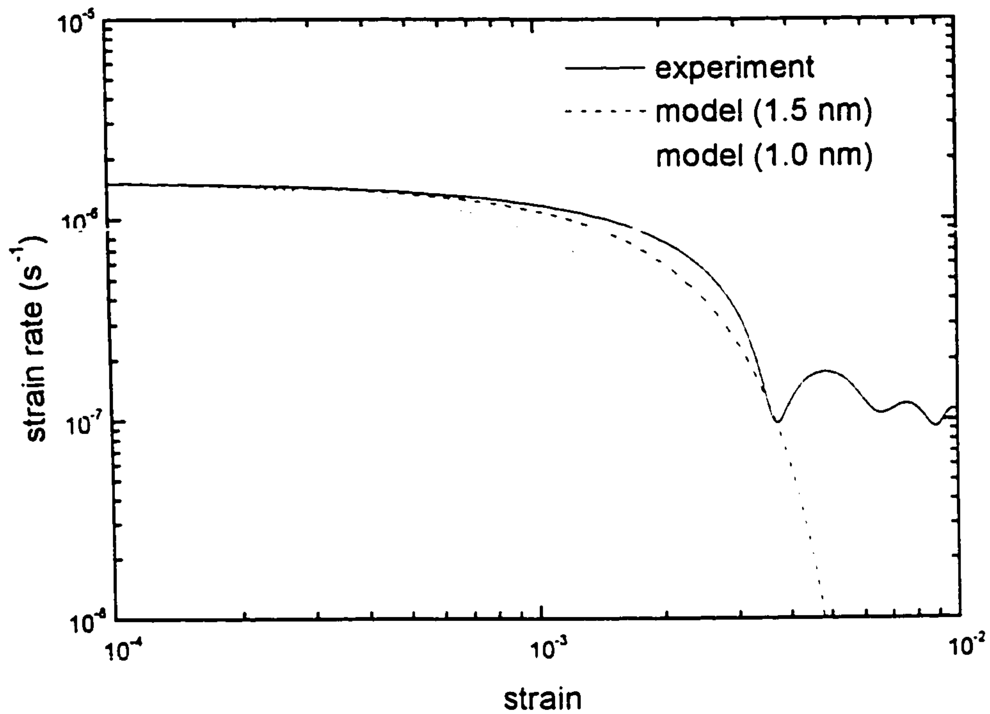

Figure 7.7 Creep resistance as a function of strain found experimentally (solid curve); and predicted theoretically (dashed curve) for compression testing at 1400°C and 200MPa. Two values of the initial film thickness (1 nm and 1.5 nm) and a stress exponent n=1.7 are used in modeling.

cavity, the assumed minimum observable cavity nucleation rate (10^{-10} s^{-1} per available site) requires a local hydrostatic tension of about 350 MPa at 1430°C (Dey et al 1997). The present model predicts that the maximum local stress concentration generated during the viscous flow process is only two and half times the applied stress (Figures 7.5-7.6). However, extensive cavitation in the crept material was observed at a stress level as low as 40 MPa. This suggests that there must be an additional mechanism for creating the critical stress for cavity nucleation, i.e. one not simply associated with the presence of secondary crystalline phase grains. One possible mechanism is grain boundary sliding, which can produce a very high hydrostatic tension in the multigrain junctions (Tsai et al 1982). Experimental evidence for stress concentrations arising from grain boundary sliding comes from the "strain whorls" observed at grain boundaries in the crept material (Wiederhorn et al 1993, Tsai et al 1982). Cavitation by grain boundary sliding in this material has been described in detail elsewhere (Luecke et al 1995, Wiederhorn et al 1993). Another possible mechanism for cavity nucleation is the presence of clusters of large grains, as proposed recently by Dey et al (1997).

Nevertheless, the presence of secondary phase grains may enhance cavitation. The normal stress on a perpendicular heterophase boundary and the multigrain junction pressure at its ends increase to $2.5\sigma^{\infty}$ when $\zeta=1$, larger than the value of $1.5\sigma^{\infty}$ for the homogeneous material. The sliding-induced stress adds to the initial hydrostatic tension, resulting in a higher local stress. The amorphous phase cavitates when the local stress in the multigrain junctions exceeds the critical stress for cavity nucleation. Lens-shaped cavities have also been observed at two-grain boundaries in the crept material (Luecke et al 1995,

Wiederhorn et al 1993). The greater thickness of heterophase boundaries (about 4 nm) and higher stress concentration ($2.5\sigma^{\infty}$) will certainly facilitate cavity nucleation at grain boundaries if a spherical cavity nucleus with the boundary thickness as its critical diameter is assumed.

The present model has a number of limitations. The microstructure is simplified as a mixture of two types of submicrostructure, region I and region II, implying that all the secondary phase grains are clustered together as shown in Figure 7.1a. The real microstructure is more random. However, the microstructure depicted in Figure 7.1a represents the extreme case for secondary phase-containing ceramics since it maximizes the heterogeneity in the microstructure. The maximum possible effect of the secondary crystalline phases on viscous flow of the boundary amorphous phase can be obtained from this model. Furthermore, the results derived from the model are based on a bimodal distribution of the boundary phase thickness while the materials may contain more than one type of heterophase boundaries such as the Y_2O_3 doped material.

7.4 Summary

The present chapter addresses theoretical modeling of viscous flow creep in Si_3N_4 ceramics containing secondary crystalline phases. A simple model considering a bimodal distribution of amorphous phase regions has been developed. The strain rate is enhanced due to the presence of secondary phase grains. The creep response predicted by this model is similar to the case of no secondary phase grains, i.e., the initial strain rate is constant followed by a sharp decrease at a limiting strain. This occurs when all the available glass

has been squeezed out from the 30° homophase boundaries in tensile creep or from perpendicular homophase boundaries in compressive creep. The experimental data and the results predicted by the model are in good agreement.

The local stresses generated during viscous flow have also been evaluated. To meet the compatibilty condition between the local regions with or without secondary phase grains, the stresses along grain boundaries and pressures in the multigrain junctions are redistributed. The local stress concentration due to viscous flow is at most $2.5\ \sigma^{\infty}$, which suggests that other mechanisms, e.g. grain boundary sliding, must be responsible for cavity nucleation in Si_3N_4 materials.

Chapter 8

SUMMARY AND CONCLUSIONS

The microstructure of silicon nitride ceramics with and without sintering additives was analyzed by using analytical electron microscopy including high-resolution electron microscopy. All the materials examined consist of equiaxed and acicular β-Si_3N_4 grains. A thin amorphous film is always present at grain- or phase-boundaries. The residual sintering liquid at multigrain junctions exists either in the crystalline form or amorphous form, depending on the sintering aids and post-sintering heat treatments. Both the undoped and Ba doped materials contain the amorphous phase at multigrain junctions as well as grain boundaries. The high temperature microstructure of the Y_2O_3 doped material contains secondary crystalline phases at multigrain junctions. Complete crystallization is not available since the aforementioned thin amorphous films still exist along Si_3N_4/secondary-phase boundaries. Fine probe EDS analysis indicates that the grain boundary amorphous phase mainly contains the cations of the sintering aids and SiO_2 which comes from the starting powder.

Both the Fresnel fringe imaging (FFI) technique and lattice fringe imaging (LFI) technique were used to image the grain-boundary amorphous films. Current investigations indicate that while LFI can provide the most accurate measurements of the boundary film thickness ($\pm$ 0.1 nm), the FFI technique is capable of relatively precise determination of the film thickness ($\pm$ 0.15 nm), and is easier to operate experimentally than the LFI

technique. It is thus suggested that the FFI method is a useful technique for quantitatively determining intergranular film thickness.

The grain boundary amorphous films exhibit a characteristic value of thickness, independent of grain misorientation. However, the film thickness depends on the chemical composition of the film and the two adjacent grains on either side of the film. The undoped material exhibited a film thickness of 1 nm. The addition of BaO increased the film thickness to 1.2 nm whereas the Y_2O_3 doped material showed an amorphous boundary film 0.7 nm in width. The heterophase boundary (i.e., Si_3N_4/secondary-phase) film thickness is in general larger than the film width along grain boundaries. This can be explained by Clarke's equilibrium film thickness theory.

Compressive creep tests on the undoped and Ba doped materials and tensile creep tests on the Y_2O_3 doped material had very similar creep characteristics. The initial strain rate remains relatively constant at low strains followed by a decrease in strain rate at higher strains. In general, the strain at which the creep rate decreased was slightly smaller for samples crept under smaller loads.

Direct evidence of viscous flow creep was obtained by measuring the film thickness distribution before and after creep. While the film widths were confined to a narrow range before creep, they generally displayed a bimodal distribution after creep. This indicates that grain boundaries under compression become thinner and those under tension become thicker. This viscous flow process mainly occurs in the initial stage of creep, although

cavitation at higher strains may also cause a local redistribution of the grain boundary amorphous phase.

A model is developed for creep by viscous flow in ceramics containing secondary crystalline phases. The strain rate is enhanced due to the presence of secondary phase grains. The creep response predicted by this model is similar to the case of no secondary phase grains, i.e., the initial strain rate is constant followed by a sharp decrease at higher strains. The local stresses caused by the secondary phases alone during viscous flow are not high enough to account for cavitation. It is thus suggested that other mechanims such as grain boundary sliding must be responsible for cavitation.

The creep behaviour observed experimentally can be explained using the model for creep due to viscous flow in multiphase ceramics. The initial constant strain rate in tension or compression is due to the redistribution of the grain boundary amorphous phase. The creep rate decreases as some of the amorphous phase is squeezed out from grain boundaries under compression. The maximum strain due to viscous flow corresponds to the situation in which a new equilibrium film thickness distribution is established according to the local normal stress throughout the material. As the thickness of the residual amorphous film between grains depends on the applied stress, the maximum strain at which the strain rate drops also depends on the applied stress. After the viscous flow process essentially stops, another mechanism will take over and dominate the creep deformation. These include dissolution-reprecipitation and grain-boundary sliding accommodated by cavitation. The active mechanism depends to a large extent on the properties of the intergranular amorphous phase.

It is recommended that for high temperature applications, the sintering additives should be tailored in material fabrication to ensure a small thickness and high viscosity of the intergranular amorphous phase. On the other hand, the strain due to viscous flow should be taken into consideration in design of structural components.

APPENDICES

Appendix A. A model for Cavity Growth by Viscous Flow and Its Effect on Grain-Boundary Film Thickness

The microstructure of glass-containing ceramics (e.g., Si_3N_4) consists of rigid grains and continuous intergranular amorphous phase (Figure A1). The amorphous phase is present both at two-grain boundaries as thin films and at triple junctions as glass pockets. The widths of the films have a characteristic value ($2\delta_0$) which is about 0.5-2 nm, depending on the chemistry of the film (Kleebe et al 1994b).

Small cavities have been found almost exclusively at triple grain junctions in glass-containing ceramics. Only a small proportion were evident along two-grain interfaces (Marion et al 1983). Cavity growth along two-grain boundaries by viscous flow has been modeled by other investigators (Evans and Rana 1980, Thouless and Evans 1986). Observations (Lange et al 1980a, Arons et al 1980) suggest that the triple junctions in typical liquid phase sintered materials are generally of sufficient size (7-100nm in diameter) to accomodate a critical nucleus with spherical morphology and accounts for most of the creep strain contributed by cavitation (Luecke et al 1995). We now wish to model the growth process of the cavities which are nucleated in the triple junctions. To facilitate the calculations, the triple junctions are simplified to cylinders of radius R.

It is assumed that the growth of cavities only occurs at triple junctions and all triple junctions cavitate simultaneously by the viscous flow mechanism, i.e., the amorphous

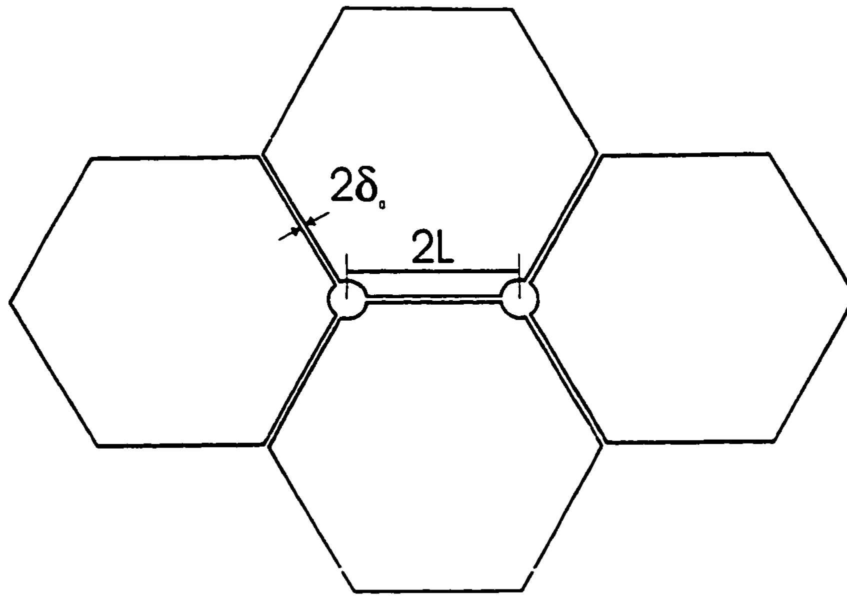

Figure A1 Microstructure of glass-containing ceramic which is simplified as hexagons of rigid grains (facet length 2L) surrounded by amorphous grain-boundary films (thickness $2\delta_0$) and cylinders of glass pockets (radius R<<L) at three-grain channels.

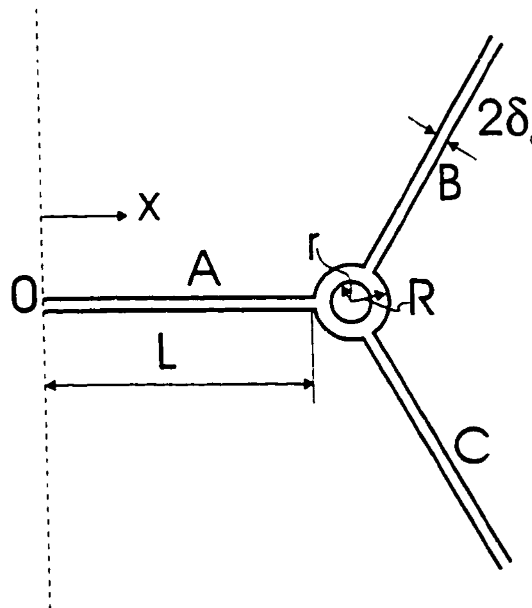

Figure A2 Schematic diagram for stress analysis during viscous flow process.

phase at triple junctions flows out into the two-grain boundaries. Analogous to liquid phase sintering, the pressure in the grain pockets is the driving force for mass flow. The assumptions of incompressible primary grains and linear viscous fluid are also used.

As shown in Figure A2, the initial condition for the pocket pressure at t=0 is $\sigma_0=\gamma/r$. On the other hand, the boundary conditions for the fluid pressure in the amorphous film at x=0 and x=L are given

$$\sigma(x=L) \approx \gamma/r, \text{ and } \frac{d\sigma(x=0)}{dx} = 0 \tag{A1}$$

where γ is the surface energy of the vsicous phase, and σ is the stress at location x. The condition at x=0 follows from geometrical symmetry considerations; the condition at x=L ensures continuity of the fluid pressure between the two-grain channel and the triple pocket.

The average velocity of motion u of a viscous phase at a location x along a boundary of uniform separation of 2δ is, at steady state (Fields and Ashby 1976)

$$u = -\frac{\delta^2}{3\eta}\frac{d\sigma}{dx} \tag{A2}$$

The fluid viscosity is denoted by η. Conservation of matter requires that

$$\frac{du}{dx} = -\frac{\dot{\delta}}{\delta} \tag{A3}$$

Intergration of this equation yields

$$u(x) = -\frac{\dot{\delta}}{\delta}x \tag{A4}$$

Combining equations A2-A3, the governing differential equations is obtained as

$$\frac{d^2\sigma(x)}{dx^2} + \frac{3\eta}{\delta^3}\frac{d\delta}{dt} = 0 \tag{A5}$$

Using the boundary conditions, the stress distribution along the boundary is

$$\sigma(x) = \frac{\gamma}{r} + \frac{3\eta\dot{\delta}}{2\delta^3}(L^2 - x^2) \tag{A6}$$

It is easy to calculate the local stresses at different boundaries (as denoted in Figure A2, boundary A, B and C)

$$\sigma_A = \frac{3}{2}\sigma^\infty \quad \text{and} \quad \sigma_B = \sigma_C = 0 \tag{A7}$$

when a uniaxial tensile stress σ^∞ is applied in the direction perpendicular to boundary A. For boundary A, mechanical equilibrium requires

$$\sigma_A L = \int_0^L \left[\frac{\gamma}{r} + \frac{3\eta\dot{\delta}_A}{2\delta_A^{\,3}}(L^2 - x^2)\right]dx \tag{A8}$$

Combining with equation A7, we have

$$\dot{\delta}_A = \frac{\left(\frac{3}{2}\sigma^{\infty} - \frac{\gamma}{r}\right)\delta_A{}^3}{\eta L^2} \tag{A9}$$

In the same way, we obtain

$$\dot{\delta}_B = \dot{\delta}_C = \frac{-\frac{\gamma}{r}\delta_B{}^3}{\eta L^2} \tag{A10}$$

Conservation of mass requires that

$$\pi(r^2 - r_0{}^2) = (2\delta_A - 2\delta_0)L + 2(2\delta_B - 2\delta_0)L \tag{A11}$$

where r_0 is the size of cavity nucleus. Here it is assumed that the cavity nucleation does not influence the initial film thickness.

Rearranging equation (A11), we have

$$\frac{\pi(r^2 - r_0{}^2)}{2L} + 3\delta_0 - \delta_A - 2\delta_B = 0 \tag{A12}$$

From equations A6-A7, we get

$$\frac{1}{\delta_B{}^2} - \frac{1}{\delta_A{}^2} = \frac{3\sigma t}{\eta L^2} \tag{A13}$$

Combining equations A7, A9 and A10, we find that

$$\frac{d\delta_B}{dt} = \frac{-\gamma}{\eta L^2}\left(\frac{\left(\frac{1}{\delta_B^{\ 2}} - \frac{3\sigma t}{\eta L^2}\right)^{-\frac{1}{2}} + 2\delta_B - 3\delta_0}{\frac{\pi}{2L}} + r_0^{\ 2}\right)^{-\frac{1}{2}} \delta_B^{\ 3} \qquad \text{(A14)}$$

This differential equation expresses the thickness change of grain boundary B as a function of time. Although an analytical solution is difficult to obtain, the equation can be solved numerically by using reasonable values of the physical parameters (Table A1). Using equations A13, A14 and A9, the thickness change at boundary A and the radius of the cavity can also be obtained as a function of time.

Table A1. Values of Assumed Parameters

Parameter	Value	Reference
δ_0	0.5×10^{-9} m	Kleebe et al (1994b)
L	0.5×10^{-6} m	
γ	0.2 $J.m^{-2}$	Marion et al (1983)
$(\eta/2\delta_0)$ at 1100-1200°C	10^{16} - 10^{17} Pa.s/m	Mosher et al (1976)
r_0	5×10^{-9} m	

The effect of viscosity of the intergranular amorphous phase on cavity growth is shown in Figure A3. The values of 10^5 -10^7 Pa.s used for the viscosity correspond to the temperature range of 1400°C-1200°C, based on the results of Mosher et al (1976). The initial growth rate is lower until the cavity reaches a critical size at which "instability" occurs. The cavity rapidly grows to the maximum size which is constrained by the size of triple junctions. The lower viscosity leads to a higher growth rate.

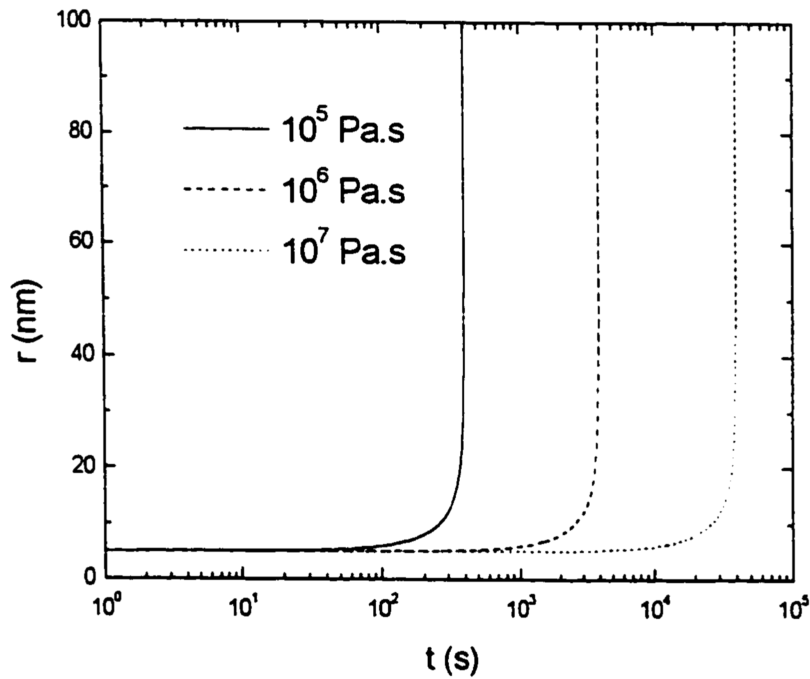

Figure A3 Effect of viscosity (or temperature) on the cavity growth rate indicating that the higher viscosity the lower growth rate (σ^{∞}=100MPa).

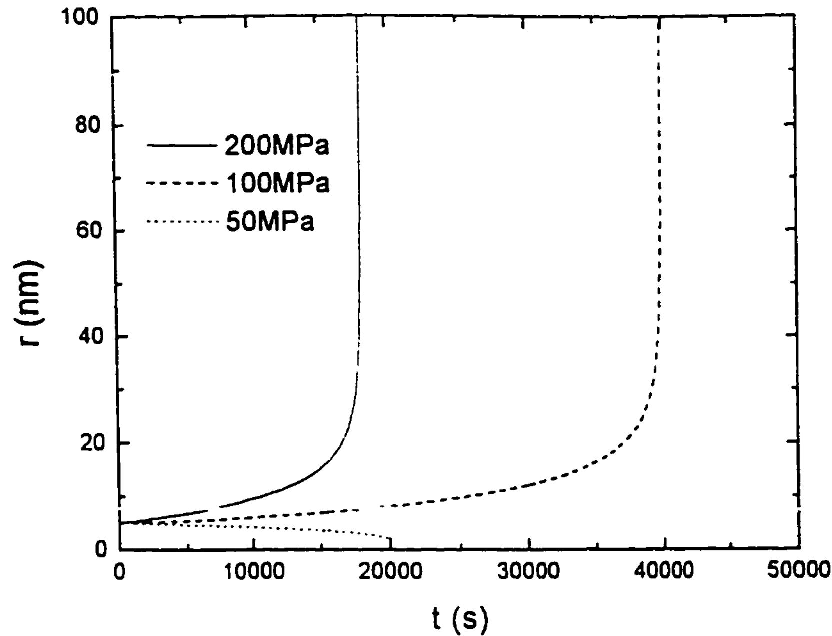

Figure A4 Effect of stresses on the cavity growth rate with an assumed viscosity $\eta=10^7$ Pa.s.

Once a cavity is nucleated, a critical value of tensile stress is required for its growth. As shown in Figure A4, for a viscosity of 10^7 Pa.s, stresses larger than 100MPa can make the cavity continuously grow until it reaches the maximum size. However, a lower stress, say, 50 MPa, can cause the cavity shrink. Obviously, a compressive stress prohibits the cavity growth process. This probably can be used to explain the creep asymmetry observed in some Si_3N_4 ceramics. Wiederhorn et al (1994) investigated the creep behaviour of the Y_2O_3 doped material and found that cavitation contributes substantially to tensile creep whereas dissolution-reprecipitation process dominates compressive creep of this material. It should be noted that cavitation process involves transient tensile stress which is not considered in the present model for cavity growth. This transient tensile stress is caused by

grain boundary sliding. Therefore, even under a compressive stress, creep cavitation may still occur.

Cavity nucleation is a heterogeneous process, depending on local stress concentration. Since viscous flow of the amorphous phase accompanies cavitation, the film thickness in the local region will be influenced by this process. In general, only grain boundaries under tension are expected to have a significant change in their film thickness, as shown in Figure A5. A cavity with a radius of 20 nm in a triple junction could increase the thickness of boundary A to 4 nm. Although a tensile stress is used in calculations, a cavity of enough size induced during compressive creep is expected to have similar effects on the local film thickness. The experimental evidence for this is shown in Figure 6.13.

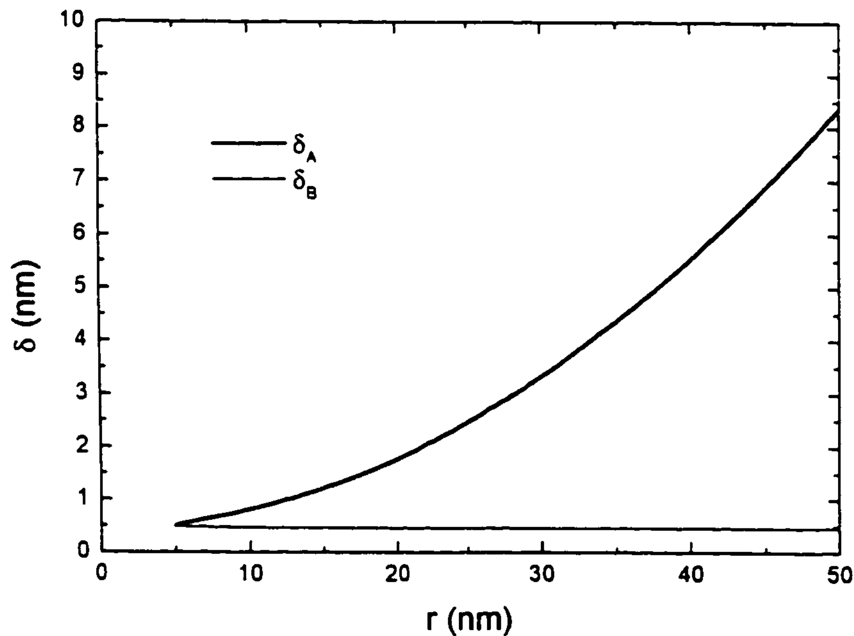

Figure A5 Effect of cavity growth on the film thickness change, showing the boundary in tension takes almost all the glass which flows out from the pockets while boundaries in compression essentially do not change their thickness (σ=100MPa, $\eta=10^5$ Pa.s).

Appendix B. Separation Rate of Parallel Plates Separated by a Newtonian Fluid Layer with Unequal Pressures at Ends

The governing differential equation for viscous flow of a Newtonian fluid layer between two parallel plates is given by (see equation (A5) in Appendix A)

$$\frac{d^2\sigma(x)}{dx^2}+\frac{3\eta}{\delta^3}\frac{d\delta}{dt}=0 \tag{B1}$$

where $\sigma(x)$ is the normal stress acting on the plate and varies as a function of position x, $d\delta / dt$ is the separation rate of parallel plates, 2δ and η are the current thickness and viscosity of the fluid layer, respectively. If we assume that the pressures at the ends of the plates are P_1 and P_2 (see Figure B1), then the boundary conditions are given by

$$\sigma_{x=L} = P_2, \sigma_{x=-L} = P_1 \tag{B2}$$

Solving this differential equation, we get the stress distribution along the boundary:

$$\sigma(x)=\frac{3\eta\dot{\delta}}{2\delta^3}(L^2-x^2)+\frac{P_2-P_1}{2L}x+\frac{P_1+P_2}{2} \tag{B3}$$

Mechanical equilibrium requires $\int_{-L}^{L}\sigma(x)dx = 2L\overline{\sigma}$, where $\overline{\sigma}$ is the average stress acting on the boundary, so the rate of separation ($\dot{\delta}$) of two parallel plates is given by

$$\dot{\delta} = \frac{(\bar{\sigma} - \frac{P_1 + P_2}{2})\delta^3}{\eta L^2} \tag{B4}$$

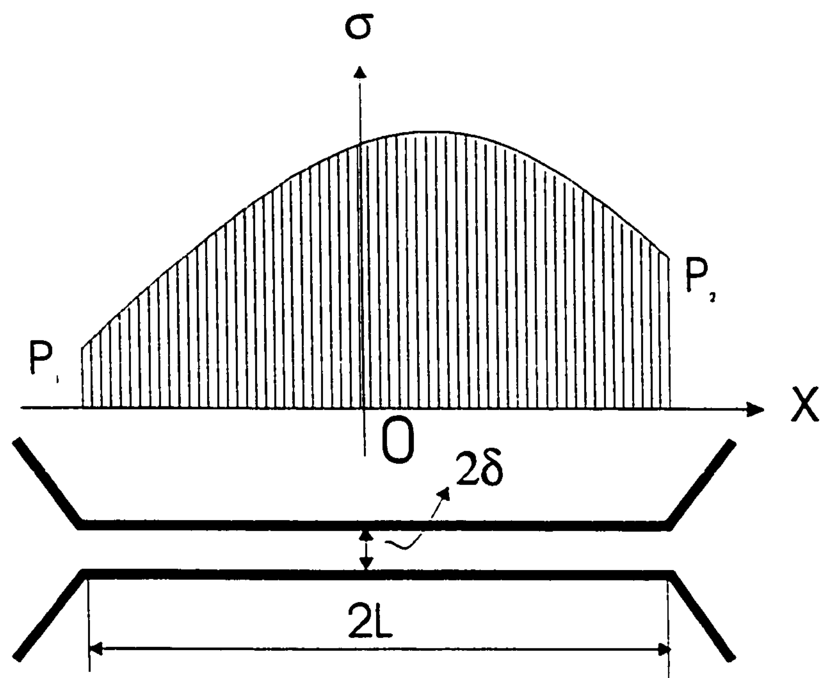

Figure B1 Schematic diagram of the stress distribution for viscous flow of a fluid layer in a two-grain boundary channel.

BIBLIOGRAPHY

Arons R.M., Tien J.K., "Creep and Strain Recovery in Hot-Pressed Silicon Nitride", J. Mater. Sci., **15**, 2046-58 (1980).

Becher P.F., Hwang H.T., Lin H.T., and Tiegs T.N., "Microstructural Contribution to the Fracture Resistance of Silicon Nitride Ceramics", in Proceedings of Workshop: Tailoring of High Temperature Properties of Si_3N_4 Ceramics. Edited by M. J. Hoffmann and G. Petzow, Kluwer Academic Publishers, Dordrecht, 87-100 (1994).

Bikerman J.J., The Science of Adhensive Joints. Academic Press, New York, 1968

Bonnell D.A., Tien T. Y. and Rühle M. R., "Controlled Crystallization of the Amorphous Phase in Silicon Nitride Ceramics", J. Am. Ceram. Soc., **70**, 460-465 (1987).

Cahn J. W. and Hilliard J. E., "Free Energy of a Nonuniform System I: Interface Free Energy", J. Chem. Phys., **28**, 258-67 (1958).

Cameron A., Basic Lubrication Theory. Ellis Hoewood, Chichester, U.K., 1976.

Carroll D.F., Wiederhorn S.M., and Roberts D.E., "Technique for Tensile Creep Testing of Ceramics", J. Am. Ceram. Soc., **72**, 1610-14 (1989).

Chadwick M.M., Wilkinson D.S., and Dryden J.R., "Creep Due to a Non-Newtonain Grain Boundary Phase", J. Am. Ceram. Soc., **75**, 2327-34 (1992).

Chadwick M.M., Jupp R.S., Wilkinson D.S., "Creep Behaviour of a Sintered Silicon Nitride", J. Am. Ceram. Soc., **76**, 385-396 (1993)

Chadwick M.M., Ph.D Thesis, McMaster University, 1990

Chan K.S., Lankford J., and Page R.A., " Viscous Cavity Growth in Ceramics under Compressive Loads," Acta Metall., **32**, 1907-14 (1984).

Chuang T.-J. and Rice J. R., "The Shape of Intergranular Creep Cracks Growing by Surface Diffusion", Acta Metall., **21**, 1625-28 (1973).

Chuang T.-J., "A Diffusive Crack-Growth Model for Creep Fracture", J. Am. Ceram. Soc., **65**, 93-103 (1982).

Chuang T.-J., Kagawa K.I., Rice J.R., and Sills L.B., "Overview No.2 : Non-Equilibrium Models for Diffusive Cavitation of Grain Interfaces", Acta Metall., **27**, 265-84 (1979).

Cinibulk M.K. and Kleebe H.-J., "Effects of Oxidation on Intergranular Phases in Silicon Nitride Ceramics", J. Mater. Sci., **28**, 5775-82 (1993).

Cinibulk M.K., Kleebe H.-J. and Rühle M.R., "Quantitative Comparison of TEM Techniques for Detecting Amorphous Intergranular Film Thickness", J. Am. Ceram. Soc., **76**, 426-32 (1993).

Cinibulk M.K., Thomas G. and Johnson S.M., "Grain-Boundary-Phase Crystallization and Strength of Silicon Nitride Sintered with a YSiAlON Glass", J. Am. Ceram. Soc., **73**, 1606-12 (1990).

Cinibulk M.K., Thomas G. and Johnson S.M., "Oxidation Behaviour of Rare-Earth Disilicate-Silicon Nitride Ceramics", J. Am. Ceram. Soc., **75**, 2050-55 (1992).

Clarke D.R., "On the Detection of Thin Intergranular Films by Electron Microscopy", Ultramicroscopy, **4**, 33-44 (1979).

Clarke D.R., "Grain Boundaries in Polyphase Ceramics", J. Phys., **C4**, 51-60 (1985).

Clarke D.R., "On the Equilibrium Thickness of Intergranular Glass Phases in Ceramic Materials", J. Am. Ceram. Soc., **70**, 15-22 (1987).

Clarke D.R., "High-Temperature Microstructure of a Hot-Pressed Silicon Nitride", J. Am. Ceram. Soc., **72**, 1604-09 (1989).

Clarke D.R., "The Intergranular Film in Silicon Nitride Ceramics: A Diffuse Interface Approach", in Proceedings of Workshop: Tailoring of High Temperature Properties of Si_3N_4 Ceramics. Edited by M. J. Hoffmann and G. Petzow, Kluwer Academic Publishers, Dordrecht, 291-301(1994).

Clarke D.R., Lange F.F., and Schnittgrund G.D., "Strength of a Sintered Silicon Nitride by a Post-Fabrication Heat-Treatment", J. Am. Ceram. Soc., **65**, C-51-52 (1982).

Clarke D.R., Shaw T.M., Philipse A.P. and Horn R.G., "Possible Electrical Double-Layer Contribution to the Equilibrium Thickness of Intergranular Glass Films in Polycrystalline Ceramics", J. Am. Ceram. Soc., **76**, 1201-204 (1993).

Clarke D.R. and Thomas G., "Grain-Boundary Phases in MgO-Fluxed Silicon Nitride", J. Am. Ceram. Soc., **60**, 491-95 (1977).

Clarke D.R. and Thomas G., "Microstructure of Y_2O_3 Fluxed Hot-Pressed Silicon Nitride", J. Am. Ceram. Soc., **61**, 114-118 (1978).

Cliff G. and Lorimer G.W., "Quantitative Analysis of Thin Specimens", J. Microsc. (Oxford). **103**, 203-207 (1975).

Coble R.L., "A Model for Boundary Diffusion Controlled Creep in Polycrystalline Materials", J. Appl. Phys., **43**, 1679-82 (1963).

Cubicciotti D. and Lau K.H., " Kinetics of Oxidation of Hot-Pressed Silicon Nitride Containing Magnasia ", J. Am. Ceram. Soc., **61**, 512-517 (1978).

Dalgleish B.J., Johnson S.M. and Evans A.G., "High-Temperature Failure of Polycrystalline Alumina: I, Crack Nucleation, J. Am. Ceram. Soc., **67**, 741-50 (1984).

Dey N., Hsia K. J., Socie D.F., "The Effects of Grain Size Distribution on Cavity Nucleation and Creep Deformation in Ceramics Containing Viscous Grain Boundary Phase", Acta Mater., **45**, 417-29 (1997).

Din S.U., Nicholson P.S., "Creep of Hot-Pressed Silicon Nitride", J. Mater. Sci., **10**, 1375-80 (1975).

Dinger T.R., Rai R.S. and Thomas G., "Crystallization Behaviour of a Glass in the Y_2O_3-SiO_2-AlN System", J.Am. Ceram. Soc., **71**, 236-44 (1988).

Drucker D.C., "Engineering and Continuum Aspects of High-Strength Materials", in High Strength Materials, Edited by V. F. Zackay, Wiley Press, New York, 795-833 (1964).

Dryden J.R. and Wilkinson D.S., "Three-Dimensional Analysis of the Creep Due to A Viscous Grain Boundary Phase," Acta mater., **45**, 1259-1273 (1997a).

Dryden J.R. and Wilkinson D.S., "A Model for the Mechanical Behaviour of Highly Concentrated Composites", Composites Science and Technology, submitted, 1997b.

Dryden J.R., Kucerovsky D., Wilkinson D.S. and Watt D.F., "Creep Deformation Due to a Viscous Grain-Boundary Phase", Acta Metall., **37**, 2007-15 (1989).

Durney D.W., "Solution-Transfer, an Important Geological Deformations Mechanism", Nature, **235**, 315-317 (1972).

Evans A.G. and Rana A., "High Temperature Failure Mechanisms in Ceramics," Acta Metall., **28**, 129-41 (1980).

Evans A.G. and Sharp J.V., "Microstructural Studies on Silicon Nitride", J. Mater. Sci., **6**, 1292-1302 (1971).

Faber K.T. and Evans A.G., "Crack Deflection Processes - I. Theory", Acta. Metall., **34**, 565-576 (1983).

Faber K.T. and Evans A.G., "Crack-Growth Resistance of Microcracking Brittle Materials", J. Am. Ceram. Soc., **67**, 255-260 (1984).

Falk L.K.L, "Microstructural Development During Liquid Phase Sintering of Silicon Carbide Ceramics", J. Eu. Ceram. Soc., **17**, 983-994 (1997).

Falk L.K.L. and Dunlop G.L., "Crystallization of the Glassy Phase in a Si_3N_4 Material by Post-Sintering Heat Treatments". J. Mater. Sci., **22**, 4369-76 (1987).

Falk L.K.L., Rundgren K., "Microstructure and Short-Term Oxidation of Hot-Pressed $Si_3N_4/ZrO_2(+Y_2O_3)$ Ceramics", J. Am. Ceram. Soc., **75**, 28-35 (1992).

Ferber M.K., Jenkins M.J., "Evaluation of the Strength and Creep-Fatigue Behaviour of Hot-Isostatically Pressed Silicon Nitride", J. Am. Ceram. Soc., **75**, 2453-62 (1992).

Fields R.J., and Ashby M.F., "Finger-Like Crack Growth in Solids and Liquids", Phil. Mag. **33**, 33-48 (1976).

Fukushima K., Kawakatsu H., and Fukami A., "Fresnel Fringes in Electron Microscope Images". J. Phys. D. 7, 257-266 (1974).

Gauckler L. J., Hohnke H. and Tien T.Y., "The System Si_3N_4-SiO_2-Y_2O_3", J. Am. Ceram. Soc., **63**, 35-37 (1980).

Gazza G.E., "Hot-Pressed Si_3N_4", J. Am. Ceram., Soc., **56**, 662 (1973).

Goldstein J.I., Williams D.B., and Cliff G., Principles of Analytical Electron Microscopy. Edited by Joy D.C., Bomig A.D., and Goldstein J.I., Plenum Press, New York, 1986.

Herring C., "Diffusional Viscosity of a Polycrystalline Solid", J. Appl. Phys., **21**, 437-45 (1950).

Hirosaki N., Okada A., Matoba K., "Sintering of Si_3N_4 with the Addition of Rare-Earth Oxides", J. Am. Ceram. Soc., **71**, C-144-147 (1988).

Hockey B.J., Wiederhorn S.M., Liu W., Boldoni J.G., and Buljan S.-T., "Tensile Creep of Whisker-Reinforced Silicon Nitride", J. Mater. Sci., **26**, 3931-39 (1991).

Hull D. and Rimmer D.E., "The Growth of Grain-Boundary Voids Under Stress", Phil. Mag., **4**, 673-687 (1959).

Jepps N.W., Page T.F. and Stobbs W.M., "Grain Boundaries in Semiconductors". Edited by H. J. Leamy, G. E. Pike and C. H. Seager, Amsterdam: Elsevier. 45-50 (1982).

Jin Q., Master Thesis, McMaster University, 1995.

Jin Q., Wilkinson D.S., Weatherly G.C., "Determination of Grain-Boundary Film Thickness by the Fresnel Fringe Imaging Technique", J. Eu. Ceram. Soc., in press, 1998.

Jin Q., Ning X.-G., Wilkinson D.S., Weatherly G.C., "Redistribution of A Grain-Boundary Glass Phase During Creep of Silicon Nitride Ceramics", J. Am. Ceram. Soc., **80**, 685-691 (1997).

Kessler H., Kleebe H.-J., Cannon R. W. and Pome W., "Effects of Internal Stress on Crystallization of Intergranular Phases in Ceramics", Acta Metall. Mater., **40**, 2233-45 (1992).

Kingery W.D., Bowen H.K., Uhlmann D.R., Introduction to Ceramics, John Wiley and Sons, USA, 1976.

Kleebe H.-J., unpublished work (1994).

Kleebe H.-J., Hoffmann M.J. and Rühle M., "Influence of Secondary Phase Chemistry on Grain Boundary Film Thickness in Silicon Nitride", Z. Metallkd., **83**, 610-617 (1992).

Kleebe H.-J., Bruley J. and Rühle M.R., "HREM and AEM Studies of Yb_2O_3-Fluxed Silicon Nitride Ceramics with and without CaO Addition", J. Eur. Ceram. Soc., **14**, 1-11 (1994a).

Kleebe H.-J. and Cinibulk M.K., "Thransmission Electron Microscopy Characterization of a Ceria-Fluxed Silicon Nitride", J. Mater. Sci. Lett., **12**, 70-72 (1993c).

Kleebe H.-J., Cinibulk M.K., Cannon R.M., and Rühle M.R., "Statistical Analysis of the Intergranular Film Thickness in Silicon Nitride Ceramics", J. Am. Ceram. Soc., **76**, 1969-77 (1993a).

Kleebe H.-J., Cinibulk M. K., Tanaka I., Bruley J., Cannon M.R., Clarke D.R., Hoffmann M. J. and Rühle M., "High-Resolution Electron Microscopy Observations of Grain-Boundary Films in Silicon Nitride Ceramics", in Silicon Nitride Ceramics: Scientific and Technological Advances, Materials Research Society Symposium Proceedings, 287. Edited by I.-W. Chen, P.F. Becher, M. Mitomo, G. Petzow and T.-S. Yan. Materials Research Society, Pittsburgh, PA, 65-78 (1993b).

Kleebe H.-J., Cinibulk M.K., Tanaka I., Bruley J., Vetrano J.S., and Rühle M.R., "High-Resolution Electron Microscopy Studies on Silicon Nitride Ceramics", in Proceedings of Workshop: Tailoring of High Temperature Properties of Si_3N_4 Ceramics. Edited by M. J. Hoffmann and G. Petzow, Kluwer Academic Publishers, Dordrecht, 259-274 (1994b).

Kleebe H.-J., Vetrano J.S., Bruley J., Rühle M., "TEM Studies of Grain Boundary Films in Si_3N_4 Ceramics", in Proceedings of 49th Annual EMSA Meeting, San Jose, CA, 930-31 (1991).

Kossowsky R., "Cyclic Fatigue of Hot-Pressed Si_3N_4", J. Am. Ceram. Soc., **56**, 531-535 (1973).

Kossowsky R., Miller D.G. and Diaz E.S., "Tensile and Creep Strength of Hot-Pressed Si_3N_4", J. Am. Ceram. Soc., **74**, 915-922 (1991).

Krivanek O.L., Shaw T.M. and Thomas G., "Imaging of Thin Intergranular Phases by High-Resolution Electron Microscopy", J. Appl. Phys., **50**, 4223-27 (1979).

Lange F.F., "Relation Between Strength, Fracture Energy, and Microstructure of Hot-Pressed Si_3N_4", J. Am. Ceram. Soc., **56**, 518-522 (1973).

Lange F.F., "Non-elastic Deformation of Polycrystals with a Liquid Boundary Phase"; in Deformation of Ceramic Materials. Edited by R.C. Bradt and R.E. Tressler. Plenum Press, New York, 361-81 (1975).

Lange L.L., "Silicon Nitride Polyphase Systems: Fabrication, Microstructure and Properties", Int. Met. Rev., **1**, 1-20 (1980).

Lange F.F., Davis B.I., and Clarke D.R., "Compressive Creep of Si_3N_4/MgO Alloys", Part 1, Effects of Composition, J.Am. Ceram. Soc., **15**, 601-610 (1980a)

Lange F.F., Davis B.I., Clarke D.R., "Compressive Creep of Si_3N_4/MgO Alloys, Part 3 Effects of Oxidation Induced Compositional Change", J. Mater. Sci., **15**, 616-618 (1980b).

Laval J.Y. and Thorel A., "Atomic Structure of Interfaces in Silicon Nitride", Mater. Sci., Forum, **47**, 143-61 (1989).

Lee W.E., Drummond C.H., Hilmas G.E., Kiser J.D., Sanders W.A., "Microstructural Evolution on Crystallizing the Glass Phase in a 6 weight % Y_2O_3-Si_3N_4 Ceramics", Ceram. Eng. Sci. Proc., **19**, 1355-65 (1988).

Lewis M.H., Bhatti A.R., Lumby R.J., and North B., "Microstructure of Sintered Si-Al-O-N Ceramics", J. Mater. Sci., **15**, 103-13 (1980).

Lewis M.H., Leng-Ward G, Jasper C., "Sintering Additives Chemistry in Controlling Microstructure and Properties of Nitride Ceramics"; in Ceramic Transactions - Proceedings of the 1 st International Conference on Ceramic Powder Processing Science, Orlando FL., Nov/87, Am. Ceram. Soc. Inc., 1019-33 (1988).

Lewis M.H., Lumby R.J., "Nitrogen Ceramics: Liquid Phase Sintering", Powder Met., **26**, 73-81 (1983).

Lewis M.H., Powell B.D., Drew P., Lumby R.J., North B., and Taylor A.J., "The Formation of Single-Phase Si-Al-O-N Ceramics", J. Mater. Sci., **12**, 61-74 (1977).

Liddell K. and Thompson D.P., "X-ray Diffraction Data for Yttrium Silicates", J. Br. Ceram. Trans., **85**, 17-22 (1986).

Loehman R.E., "Structure, Formation, and Stability of Oxynitride Glasses"; in Tailoring of High Temperature Properties of Si_3N_4 Ceramics. Edited by Hoffmann, M.J. and Petzow, G. Kluwer Academic Publishers, Dordrecht, Netherlands, 167-173 (1994).

Lou L.K., Mitchell T.E., and Heuer A.H., "Discussion of 'Grain Boundary Phases in a Hot-Pressed MgO-Fluxed Silicon Nitride' ", J. Am. Ceram. Soc., **61**, 462-64 (1978).

Luecke W.E., private communication, 1997

Luecke W.E. and Wiederhorn S.M., unpublished work, 1993

Luecke W.E. and Wiederhorn S.M., "Tension/Compression Creep Asymmetry in Si_3N_4", in Silicon Nitride 93 Stuttgart, International Conference on Silicon Nitride-Based Ceramics, Stuttgart, Germany. Trans. Tech. Publications, Switzerland, 587-92 (1994).

Luecke W.E., Wiederhorn S.M., Hockey B.J., Krause R.F. and Long G.G., "Cavitation Contributes Substantially to Tensile Creep in Silicon Nitride", J. Am. Ceram. Soc., **78**, 2085-96 (1995).

Marion J.E., Evans A.G., Drory M.D., Clarke D.R., "High Temperature Failure Initiation in Liquid Phase Sintered Ceramics," Acta Metall., **31**, 1445-57 (1983).

Marion J.E., Hsueh C.H. and Evans A.G., "Liquid Phase Sintering of Ceramics", J. Am. Ceram. Soc., **70**, 708-713(1987).

McDonough W.J., Wu C.Cm. and Morgan P.E.D., "Internal Phase Changes in Dense Si_3N_4 Associated with High-Temperature Oxidation", J. Am. Ceram. Soc., **64**, C-45-C-47 (1981).

Mosher D.R., Raj R., Kossowsky R., "Measurement of Viscosity of the Grain Boundary Phase in Hot-Pressed Silicon Nitride", J. Mater. Sci., **11**, 49-53 (1976).

Nabarro F.R.N., Report on a Conference on the Strength of Metals, Phys. Soc. London, 1948.

Menon M.N., Fang H.T., Wu D.C., Jerkins M.G., Ferber M.K., More K. L., Hubbard C.R. and Nolan T.A., "Creep and Stress Rupture Behaviour of an Advanced Silicon Nitride: Part I, Experimental Observation", J. Am. Ceram. Soc., 77, 1217-27 (1994).

Morrell R. and Ashbee K.H.G., "High Temperature Creep of Lithium Zinc Silicate Glass-Ceramics - Part I, General Behaviour and Creep Mechanisms", J. Mater. Sci., **8**, 1253-70 (1973).

Ness J. N., Stobbs W.M. and Page T.F., "A TEM Fresnel Diffraction-Based Method for Characterizing Grain-Boundary and Interfacial Film", Phil. Mag. A, **54**, 679-702 (1986).

Page R.A. and Chan K.S., "Stochastic Aspects of Creep Cavitation in Ceramics", Metall. Trans. **18A**, 1843-1854 (1987).

Page R.A., Lankford J. and Chan K.S., Hardman-Rhyne K., Spooner S., "Creep Cavitation in Liquid-Phase-Sintered Alumina," J. Am. Ceram. Soc., **70**, 137-45 (1987).

Page R.A., Lankford J. and Spooner S., "Small-Angle Neutron Scattering Study of Creep Cavity Nucleation and Growth in Sintered Alumina", J. Mater. Sci., **19**, 3360-74 (1984a).

Page R.A., Lankford J. and Spooner S., "Nucleation and Early-State Growth of Creep Cavities in Hot-Pressed Silicon Carbide," Acta Metall., **32**, 1275-86 (1984b).

Pan X.-Q., "Atomic Structure of Silicon Nitride/Silicate Glass Interfaces", J. Am. Ceram. Soc., **79**, 2975-79 (1996).

Perice L.A., Mieskowski D.M. and Sanders W.A., "Effects of Grain-Boundary Crystallizatioin on the High-Temperature Strength of Silicon Nitride", J. Mater. Sci., **21**, 1345-48 (1986).

Pharr G.M. and Ashby M.F., "On Creep Enhanced by a Liquid Phase," Acta Metall., **31**, 129-38 (1983)

Rae A.W.J.M., Thompson D.P., Pipkin N.J., and Jacj K.H., Special Ceramics 6. Edited by Popper P. British Ceramic Research Association, Stoke-on-Trent, 347-60 (1975).

Raj R. and Ashby M.F., "Intergranular Fracture at Elevated Temperatures ", Acta Metall., **23**, 653-666 (1975).

Raj R., "Creep in Polycrystalline Aggregates by Matter Transport Through a Liquid Phase", J. Geophys. Res., **87B**, 4731-39 (1982).

Raj R. and Chyung C.K., "Solution-Precipitation Creep in Glass Ceramics", Acta Metall., **129**, 159-166 (1981).

Raj R. and Lange L.L., "Crystallization of Small Quantities of Glass (or Liquid) Segregated in Grain Boundaries", Acta Metall., **29**, 1993-2000 (1981).

Reimer L., Transmission Electron Microscopy, Springer-Verlag, Berlin, FRG, 63-69 (1989).

Sanders W.A., Mieskowski D.M., "Strength and Microstructure of Sintered Si_3N_4 with Rare-Earth-Oxide Additives", J. Am. Ceram. Soc., **64**, 304-09 (1985).

Schmid H., Rühle M., "Structure of Special Grain Boundaries in SiAlON Ceramics", J. Mater. Sci., **19**, 615-628 (1984).

Singhal S.C., "Thermodynamics and Kinetics of Oxidation of Hot-Pressed Silicon Nitride", J. Mater. Sci., **11**, 500-509 (1976).

Smith J.T., and Quackenbush C.L., "Phase Effects in Si_3N_4 Containing Y_2O_3 or CeO_2: 1. Strength", Bull. Amer. Ceram. Soc., **59**, 529-532 (1980).

Tanaka I., Bruley J., Gu H., Hoffmann M.J., Kleebe H.-J., Cannon R.M., Clarke D.R., Rühle M., "Compositions and Thicknesses of Grain Boundary Films in Ca-Doped Silicon Nitride Ceramics", in Tailoring of High Temperature Properties of Si_3N_4 Ceramics. Edited by Hoffmann, M.J. and Petzow, G. Kluwer Academic Publishers, Dordrecht, Netherlands, 275-289 (1994c).

Tanaka I., Igashira K., Kleebe H.-J. and Rühle M., "High-Temperature Strength of Fluorine-Doped Silicon Nitride", J. Am. Ceram. Soc., 77, 275-77 (1994a).

Tanak I, Kleebe H.-J., Cinibulk M.K., Bruley J., Clarke D.R. and Rühle M., "Calcium Concentration Dependence of the Intergranular Film Thickness in Silicon Nitride", J. Am. Ceram. Soc., 77, 911-914 (1994b).

Thorel A., Laval J. Y., Broussaud D., Sagey G. and Schffmacher G., "Grain Boundary Structure of SiAlON for Thermomechanical Applications", Grain Boundary Structure and Related Phenomena, Proceedings of JIMIS-4, Trans. Japn. Inst. Met., Suppl., 819-26 (1986).

Thouless M.D., "A Review of Creep Rupture in Materials Containing an Amorphous Phase", Res Mechanica, **22**, 213-242 (1987).

Thouless M.D. and Evans A.G., "Nucleation of Cavities During Creep of Liquid-Phase-Sintered Materials," J.Am. Ceram. Soc., **67**, 721-27 (1984a).

Thouless M.D. and Evans A.G., "On the Nucleation of Cavities During the Creep of Liquid Phase Sintered Materials", J. Am. Ceram. Soc., **67**, 741-750 (1984b).

Thouless M.D. and Evans A.G., "On Creep Rupture in Materials Containing an Amorphous Phase", Acta Metall., **34**, 23-31 (1986).

Tighe N.J., Wiederhorn S.M., Chuang T.-J., McDaniel C.L., "Creep Cavitation and Crack Growth in Silicon Nitride", in Deformation of Ceramic Materials II. Edited by Tressler R.E., Bradt R.C., Plenum Press, N.Y., 587-604 (1984).

Tsai R.L. and Raj R., "Creep Fracture in Ceramics Containing Small Amounts of a Liquid Phase", Acta Metall., **30**, 1043-58 (1982).

Tsuge A., Nishida K., and Komatsu M., "Effect of Crystallizing the Grain-Boundary Glass Phase on the High-Temperature Strength of Hot-Pressed Si_3N_4 Containing Y_2O_3", J. Am. Ceram. Soc., **58**, 323-326 (1975).

Vetrano J.S., Kleebe H.-J., Hampp E., Hoffmann M.J., Rühle M., Cannon R.M., "Yb_2O_3-Fluxed Sintered Silicon Nitride", J. Mater. Sci., **28**, 3529-38 (1993).

Wang C.-M., Pan X.-Q., Hoffmann M. J., Cannon R.M., Rühle M., "Grain Boundary Films in Rare-Earth-Glass-Based Silicon Nitride", J. Am. Ceram. Soc., **79**, 788-92 (1996).

Wiederhorn S.M., Chuck L., Fuller E.R., and Tighe N.J., "Creep Rupture of Siliconized Silicon Carbide"; in Tailoring Multiphase and Composite Ceramics, Materials Science and Research. Edited by Tressler R.E., Messing G.L., Pantano C.G. and Newnham R.E., Plenum Press, New York, 755-73 (1986).

Wiederhorn S.M., Hockey B.J., Cranmer D.C. and Yeckley R., "Transient Creep Behaviour of Hot Isostatically Pressed Silicon Nitride", J. Mater. Sci., **28**, 445-53 (1993).

Wiederhorn S.M., Hockey B.J., Krause R.F., Jakus K., "Creep and Fracture of a Vitreous-Bonded Aluminum Oxide", J. Mater. Sci., **21**, 810-824 (1986).

Wiederhorn S.M., Luecke W.E., Hockey B.J., Long G.G., "Creep Damage Mechanisms in Si_3N_4"; in Tailoring of High Temperature Properties of Si_3N_4 Ceramics. Edited by Hoffmann, M.J. and Petzow, G. Kluwer Academic Publishers, Dordrecht, Netherlands, 305-326 (1994).

Wiederhorn S.M., Roberts S.M., Chuang T.-J., and Chuck L., "Damage-Enhanced Creep in Siliconized Silicon Carbide: Phenomenology", J. Am. Ceram. Soc., **71**, 602-608 (1988).

Wild S., Grievson P., Jack K.H., and Latimer M.J., Special Ceramics 5. Edited by Popper P. British Ceramic Research Association, Stoke-on Trent, 377-84 (1972).

Wilkinson D.S., "Creep Mechanisms in Multiphase Ceramic Materials", J. Am. Ceram. Soc., **81**, 275-99 (1998).

Wilkinson D.S., "Creep Mechanisms in Silicon Nitride Ceramics", in Tailoring of High Temperature Properties of Si_3N_4 Ceramics. Edited by Hoffmann M.J. and Petzow G. Kluwer Academic Publishers, Dordrecht, Netherlands, 327-338 (1994).

Williams D.B., Practical Analytical Electron Microscopy in Materials Science, 2nd Edition. Philips Electron Optics Publishing Group, Mahwah, New Jersey, 1987.

Yeckley R.L. and Siebein K.N., "High Temeprature Cavitation of HIP Silicon Nitride", in Ceramic Materials and Components for Engines. Edited by Tennery V.J., American Ceramic Society, Westerville, OH, 751-765 (1989).

Ziegler G., Heinrich J. and Wötting G., "Review: Relationship Between Processing, Microstructure and Properties of Dense and Reaction Bonded Silicon Nitride", J. Mater. Sci., **22**, 3014-86 (1987).